ABSTRACT

Title of Dissertation: MULTI-INSTRUMENT APPROACH FOR MEASURING SPECTRAL AEROSOL ABSORPTION PROPERTIES IN UV AND VIS WAVELENGTHS

Jungbin Mok, Doctor of Philosophy, 2017

Directed By: Professor Zhanqing Li
Department of Atmospheric and Oceanic Science/Earth System Science Interdisciplinary Center

Dr. Nickolay A. Krotkov
NASA Goddard Space Flight Center

The spectral dependence of light absorption by atmospheric particulate matter (PM) has major implications for air quality, surface ultraviolet (UV) radiation, and tropospheric oxidation capacity, but remains highly uncertain. Quantifying the spectral dependence of aerosol absorption at UV and visible wavelengths is important for the accurate air pollution characterization using current (e.g., Aura/OMI) and future (e.g., TROPOMI, TEMPO, GEMS) satellite measurements, photolysis rates calculations in chemical and aerosol transport models and surface radiation modeling. Measurements of column atmospheric absorption and its spectral dependence remain the most difficult part of atmospheric radiation measurements. Currently available ground measurements of spectral aerosol absorption properties (e.g., column effective imaginary refractive index (k), single scattering albedo, (SSA), and aerosol absorption optical depth (AAOD)) are limited to the cloud free conditions and few discrete wavelength

bands in the visible spectral region by AERONET almucantar inversions. To address the lack of spectral aerosol and gaseous absorption measurements in the UV, a suite of complementary ground-based instruments, modified UV Multifilter Rotating Shadowband Radiometer (UV-MFRSR) was established in 2002 and is currently in use at NASA Goddard Space Flight Center (NASA/GSFC) in Greenbelt, Maryland. In addition, several field campaigns have been carried out to measure aerosol absorption properties in UV and VIS from different sources in different locations.

In September-October 2007 biomass-burning season in the Amazon basin (Santa Cruz, Bolivia), light absorbing (chromophoric) organic or "brown" carbon (BrC) is studied with surface and space-based remote sensing. It is found that BrC has negligible absorption at visible wavelengths, but significant absorption and strong spectral dependence at UV wavelengths. Using the ground-based inversion of column effective imaginary refractive index (k) at UV wavelengths down to 305 nm, a strong spectral dependence of specific BrC absorption is quantified in the UV implying more strongly reduced ultraviolet B (UV-B) radiation reaching the surface. Reduced UV-B means less erythema, plant damage, but also a slower ozone photolysis rate. A photochemical box model is used to show that relative to black carbon (BC) alone, the combined optical properties of BrC and BC slow the net rate of production of ozone by up to 18% and lead to reduced concentrations of radicals OH, HO_2, and RO_2 by up to 17%, 15%, and 14%, respectively. The optical properties of BrC aerosol change in subtle ways the generally adverse effects of smoke from biomass burning.

The objective of this thesis is to develop a new method to infer column effective spectral absorption properties (*k*, SSA, and AAOD) of PM using the ground-based measurements from AERONET in the visible wavelengths and UV-MFRSR in the UV and ozone and NO_2 from ground-based (Pandora and Brewer) or satellite spectrometers, such as Ozone Monitoring Instrument (OMI) on NASA EOS Aura satellite. This represents the first effort to separate effects of gaseous (ozone and NO_2) and aerosol absorption and partition black and brown (light-absorbing organic) carbon absorption in the short UV-B wavelengths. These measurements are essential to answer key science questions of the atmospheric composition and improve data products from the current and future satellite atmospheric composition missions.

MULTI-INSTRUMENT APPROACH FOR MEASURING SPECTRAL AEROSOL ABSORPTION PROPERTIES IN UV AND VIS WAVELENGTHS

By

Jungbin Mok

Dissertation submitted to the Faculty of the Graduate School of the
University of Maryland, College Park, in partial fulfillment
of the requirements for the degree of
Doctor of Philosophy
2017

Advisory Committee:
Professor Zhanqing Li, Chair/Advisor
Dr. Nickolay A. Krotkov, Advisor
Professor Russell R. Dickerson
Professor Rachel Pinker
Dr. Omar Torres
Professor James Farquhar, Dean's representative

Dedication

My thesis is dedicated to my wife, Hyelim, and my daughter, Kate.

Acknowledgements

First and foremost, I would like to give my sincere gratitude to my advisors, Professor Zhanqing Li and Dr. Nickolay A. Krotkov, for their excellent guidance, sincere support, and encouragement throughout the study. They encouraged me to complete this long journey. Many thanks to the members of my committee, Professors Russell R. Dickerson, Rachel Pinker, and James Farquhar, and Dr. Omar Torres for their insightful comments and suggestions.

This thesis has been funded by the ESSIC–NASA Master grant, National Science Foundation, and Aura/OMI project. I really appreciate for their support.

I would especially like to thank close collaboration with Gordon Labow, Sergey Osipov, and Drs. Antti Arola, Georgiy Stenchikov, Hiren Jethva, Nader Abuhassan, Seoung-Soo Lee, Thomas F. Eck, and Xinrong Ren. I would also like to thank Ms. Maureen Cribb for her wonderful advice and help on writing my papers. I am also very grateful to all faculty and staff of AOSC and ESSIC for their kindly help. Andrew Jongeward, Pat Kablick, Youtong Zheng, Dr. Jianjun Liu, and other members in Dr. Li's team are to be thanked for their encouragement, discussion, and suggestions.

A special thanks to members of AERONET team, UV-B Monitoring and Research Program, Drs. Omar Torres and Marcos Andrade for conducting field measurements in Santa Cruz, Bolivia, Professor Jhoon Kim and his team in Yonsei University for conducting field measurements in Seoul, South Korea, and Professor Hitoshi Irie and SKYNET team in Chiba University, Japan.

Deepest thanks must also be recorded to my parents, Donsoo Mok and Youngja Yoon, my sister, Eunha Mok, parents in law, and University Church family. Their support and prayer keep me pursuing my dream. Finally and without hesitation I would like to give my earnest thanks and love to my wife, Hyelim Yoo and daughter, Kate Mok for their support and love. They are all my energy.

Table of Contents

List of Tables

List of Figures

Chapter 1: Introduction

1.1. Background

Aerosols change the budget of incoming and outgoing radiation and perturb the radiative balance. To quantify the radiative effects of aerosols, the aerosol optical depth (AOD) and single scattering albedo (SSA) are measured using ground-based, orbital and sub-orbital platforms. The aerosol absorption changes atmospheric stability and cloud formation (aerosol semi-direct effects [Hansen et al, 1997; Johnson et al., 2004]) and modifies the hydrological cycle [Koren et al., 2004]. While the potential climate effects of absorbing aerosols have received considerable attention lately [IPCC, 2007; Myhre et al., 2013], their effects on surface ultraviolet (UV) and photochemistry can be equally important for tropospheric chemistry and may affect human health and agricultural productivity [Dickerson et al., 1997; Krotkov et al., 1998; He and Carmichael, 1999; Castro et al., 2001]. Quantifying the spectral dependence of aerosol absorption at UV and visible wavelengths is important for monitoring air pollution using current (e.g., Aura/OMI) and future (e.g., TROPOMI, TEMPO, GEMS) satellite measurements. Measurements of column atmospheric aerosol absorption and its spectral dependence in UV remain one of the most difficult tasks in atmospheric radiation measurements.

The enhanced column UV absorption (small SSA values) is commonly

attributed to the organic aerosol (OA) that absorbs predominantly in the UV, explaining much stronger wavelength dependence than a purely black carbon (BC) model would suggest [Kirchstetter et al., 2004]. Martins et al. [2009] show that the SSA of urban aerosol is considerably smaller in UV (implying larger absorption) than in visible wavelengths probably linked to the absorption by OA. This added OA UV absorption doubles absorption efficiency of BC and reduces surface UV fluxes by up to 50%. Current studies [Feng et al., 2013; Saleh et al., 2014] reported that the light absorbing component of organic carbon (OC) known as "brown carbon" (BrC) is capable of enhancing total absorption efficiency of OC, potentially altering direct radiative forcing (DRF) at the top of the atmosphere from negative to positive. Strong absorption of BrC at UV wavelengths has a significant impact on the photochemistry [Krotkov et al., 2005b; Bergstrom et al. 2007; 2010]. In addition, unaccounted aerosol absorption in the UV might have explained a positive bias in satellite estimated surface UV radiation [Krotkov et al., 1998; 2005b; Li et al., 2000; Ciren and Li, 2003; Arola et al., 2009].

To measure aerosol absorption, the diffuse/direct method has been introduced by M. King and B. Herman in late 1970s. The direct solar flux is defined as the portion of the solar flux, which reaches the Earth's surface without scattering and absorption in the atmosphere. By contrast, the diffuse solar flux means the radiation multiple scattered by air molecules and aerosols from the direct solar beam. Downwelling portion of diffuse radiation can be measured from the surface and upwelling diffuse radiation scattered back to space can be

measured with satellites. The atmospheric scattering processes are described by radiative transfer (RT) theory, which requires knowledge of molecular and aerosol-scattering phase functions, aerosol single scattering albedo (SSA, scattering to extinction ratio), surface albedo, the solar zenith angle (SZA), and the aerosol and molecular optical depths [Herman et al., 1975]. The phase functions and SSA can be calculated given the particle size- and shape-distributions combined with the known spectral dependence of the complex refractive index, $m(\lambda) = n(\lambda) + ik(\lambda)$ [Mishchenko et al., 2002; Thomas and Stamnes, 1999]. For naturally occurring inhomogeneous particles or aerosol mixtures an effective refractive index can be derived through inversions of the measured radiation, provided all other inputs, such as particle mixing state, size- and shape-distributions, and surface reflection, are known or simultaneously retrieved [Dubovik et al., 2000; Herman et al., 1975; King and Herman, 1979]. The spectral dependence of the effective imaginary refractive index, $k(\lambda)$ contains information about aerosol composition and provides insights into aerosol speciation [Mok et al., 2016; Schuster et al., 2016]. It is therefore important to further develop multi-instrument atmospheric measurement techniques, which allow derivation of the extended spectrum of the refractive index: from near ultraviolet (UV-B and UV-A) through visible to near infrared (NIR) wavelengths.

As first demonstrated by Herman et al. [1975], the imaginary part of the refractive index (k) is remarkably sensitive to the downwelling diffuse to direct irradiance ratio (DD) for a fixed aerosol optical depth (AOD), surface albedo, and SZA (Figure 1.1). The variation in the real part of the refractive index has a small

effect (a few percent) on DD irradiance ratio. The DD ratio depends on SZA and increases with surface albedo (Figure 1.1). Therefore, surface albedo should be accounted for to get better accuracy of the DD method. This method uses the relative magnitude of the diffuse and direct flux, which cancels sensitivity to the extraterrestrial solar irradiance. However, measurements of AOD do require calibration of the direct solar irradiance with respect to the extraterrestrial measurement. This is typically done using Langley calibration technique [Harrison and Michalsky, 1994; Slusser et al., 2000].

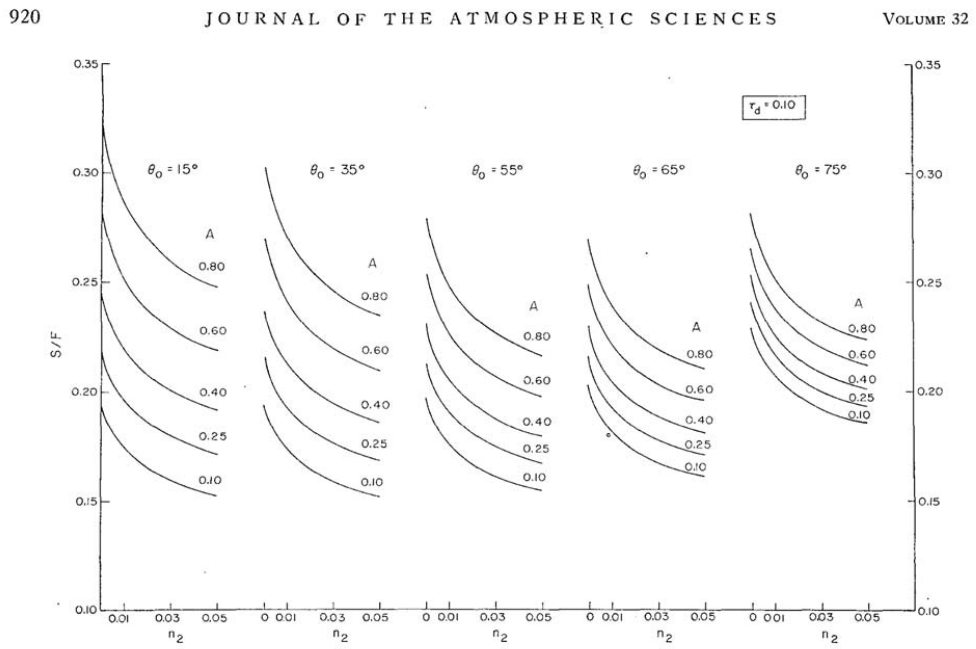

FIG. 2. The ratio of diffuse to direct solar flux, S/F, vs absorption refractive index n_2, for five solar zenith angles, as a function of surface reflectivity A. The dust optical depth is 0.10.

Figure 1.1. The diffuse to direct method to measure aerosol absorption from Herman et al. [1979].

King [1979] first demonstrated the diffuse/direct method to measure the

aerosol absorption. He used a research hemispheric radiometer with solar shadowing ball to measure the downward hemispheric diffuse and global fluxes. The first commercial MultiFilter Rotating Shadowband Radiometer (MFRSR – Yankee Environmental systems, INC, http://www.yesinc.com/) (Figure 1.2) was developed by Harrison et al. [1994]. The MFRSR provides the direct-normal, diffuse-horizontal, and total-horizontal irradiance in seven narrow-filter spectral bandpasses.

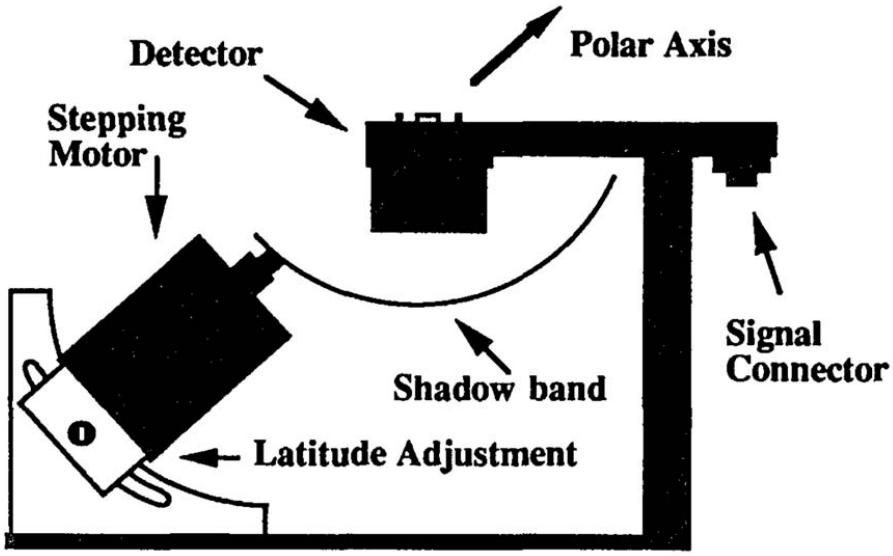

Figure 1.2. The basic geometry of the MFRSR from Harrison et al. [1994].

1.2. Importance of aerosol absorption in UV wavelength

Aerosol in the planetary boundary layer (PBL) can significantly modify air quality either directly or by changing the rate of tropospheric ozone (urban

smog) formation [Jacobson, 1998]. Aerosol scattering increases the actinic flux and the rates of photochemical reactions in the upper parts of the PBL [Dickerson et al., 1997], whereas aerosol absorption reduces the amount of UV radiation available for chemical UV absorption. The magnitude and even the sign of the aerosol effect on the tropospheric photochemistry remain highly uncertain. For example, absorbing aerosols decrease the photolysis rates of UV-absorbing gases and thus reduce ground-level ozone amount [Jacobson, 2002]. On the other hand, non-absorbing aerosols increase the photolysis rates of UV-absorbing gases and thus increase tropospheric ozone amount [Dickerson et al., 1997; Jacobson, 1998].

The UV aerosol absorption suppresses both biologically active UV radiation [Madronich, 1993; Krotkov et al., 1998] and photolysis rates of important pollutants (ozone and NO2) in the PBL providing a negative feedback for photochemical smog formation. Kerr et al. [2002] used radiative transfer (RT) calculation and found that a decrease in the UV by moderate increases in absorbing aerosol were comparable to that caused by stratospheric ozone recovery. Stratospheric ozone has an effect only on the UV-B (280 – 320 nm), whereas aerosols affect both UV-B and UV-A (320 – 400 nm) spectral ranges. As a result, local change in aerosols may enhance, reduce or even reverse changes in the UV resulted from expected stratospheric ozone recovery [Krotkov et al., 2005a; Kerr et al., 2002].

Aerosol absorption in the UV region affects satellite retrievals of surface UV irradiance [Krotkov et al., 1998]. The unaccounted absorption by UV-absorbing aerosols can explain the positive bias in satellite derived surface UV-B

radiation compared to ground-based measurements as shown Figure 1.3. The bias can be corrected if aerosol absorption optical depth (AAOD = AOD*(1-SSA)) is known [Krotkov et al., 2005b; Arola et al., 2005]. The AAOD requires knowledge of both AOD and SSA. These can be retrieved from satellite, provided spectral shape of *k* is known a priori [Torres et al., 2007; Jethva et al., 2014].

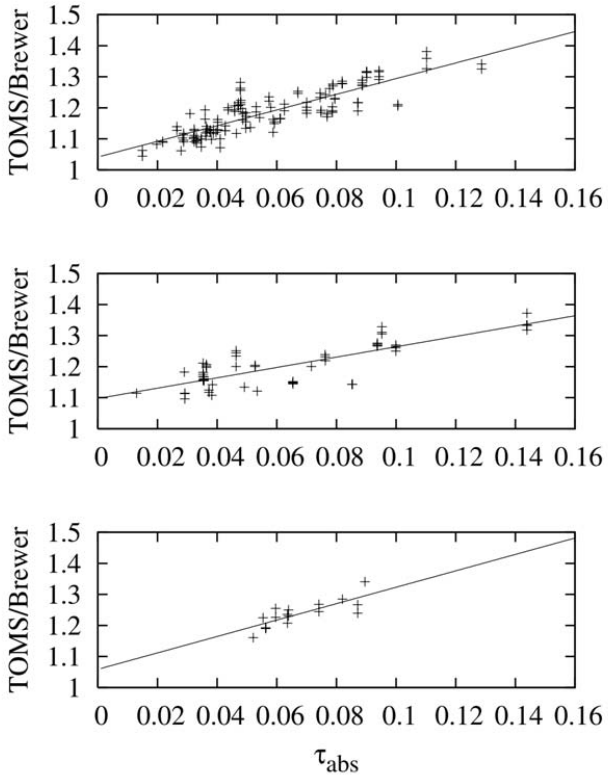

Figure 1.3. The ratio of TOMS/Brewer irradiance (324 nm) as a function of AAOD at Thessaloniki, Greece from Arola et al. [2005].

Black carbon (BC) has received lot of attention because of its role of the largest global warming agent after CO_2 [Bond et al., 2013]. Pure BC is insoluble [Bond et al., 2013; Wang et al., 2014], but in the atmosphere, it can be coated by

other materials (e.g., sulfate or organic) through processes, such as condensation and coagulation [Liu et al., 2013; Wang et al., 2014]. Because most of coating materials are soluble, BC is converted from hydrophobic to hydrophilic during aging and transport processes, which leads to reducing its residence time through wet-deposition process. Typical aging lifetime of BC is about one day [Wang et al., 2014]. The aging lifetime can differ significantly depending upon dominant coating substances, such as slow mixing with sulfuric acid in urban areas and rapid mixing with co-emitted soluble organic compounds in biofuel/biomass burning. The aging effect of BC is also significant for the direct radiative forcing (DRF) since it enhances the absorption of solar radiation [Schnaiter et al., 2005; Bond and Bergstrom, 2006]. Model estimated global mean DRF of BC range from 0.19 to 0.9 Wm^{-2} [Myhre et al., 2013; Bond et al., 2013; Wang et al., 2014]. This range can be explained in part by misrepresentation of the additional absorption from organic carbon (OC).

Recently, the needs for measurements of column atmospheric aerosol absorption in UV wavelengths are highlighted in the global aerosol chemistry model simulation. Current aerosol and chemistry transport models treat all OC from biomass burning as purely scattering, thus, underestimating heating effect of the total carbon (BC+OC) – primary absorbing component of carbonaceous aerosols [Cooke et al., 1999; Chung and Seinfeld, 2002; Bond et al., 2013; Myhre et al., 2013]. However, recent laboratory studies [Saleh et al., 2013; 2014; Chen and Bond, 2010; Kirchstetter et al., 2004; Yang et al., 2009; Chakarbarty et al., 2010; Zhong and Jang, 2014; Lack et al., 2012; Favez et al., 2009] suggest that

the light absorbing component of OC known as “brown carbon” (BrC) is capable of enhancing total absorption efficiency of OC, altering the direct radiative forcing (DRF) from negative to positive [Bond, 2001; Kirchstetter et al., 2004; Feng et al., 2013; Saleh et al., 2014]. For instance, Hammer et al. [2016] show that carbonaceous aerosol absorption over most of biomass burning is underestimated if OC is regarded as purely scattering in a global 3-D chemical transport model (GEOS-Chem) simulation. However, a better agreement with satellite observations after implementing the BrC absorption parameterization into GEOS-Chem (Figure 1.4).

(a)

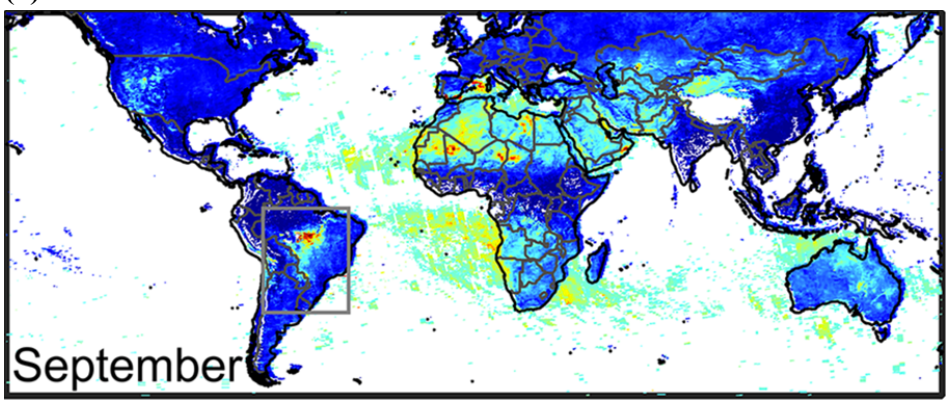

(b)

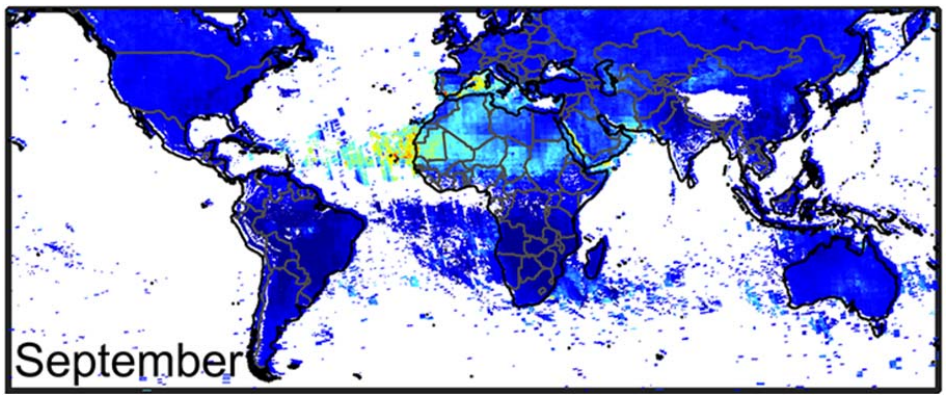

(c)

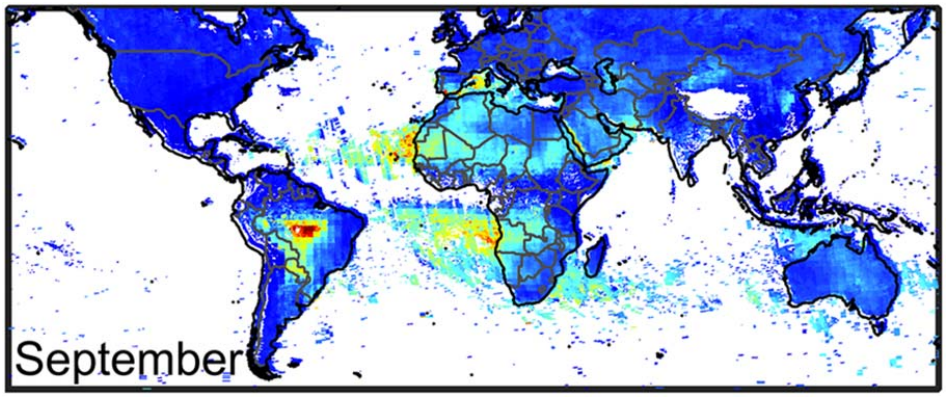

Figure 1.4. Monthly mean UV aerosol index (UVAI) of (a) observation from Ozone Monitoring Instrument (OMI) onboard NASA Aura satellite [Torres et al., 2007], (b) simulation from GEOS-Chem without BrC absorption, and (c) simulation from GEOS-Chem with BrC absorption, and (c) simulation from GEOS-Chem with BrC absorption for September 2007 from Hammer et al. [2016].

1.3. Objectives and Outline

The ultimate goal of this study is to develop a new method to infer the full spectrum of aerosol absorption properties (e.g., effective imaginary refractive index (k), SSA, and AAOD) combining ground-based AERONET retrievals in the visible wavelengths and UV-MFRSR retrievals in the UV with the most accurate gaseous (ozone and NO_2) column densities from Brewer, Pandora or satellite retrievals from Ozone Monitoring Instrument (OMI) on board NASA EOS Aura satellite. This represents the first effort to separate effects of gaseous (ozone and NO2) and aerosol absorption and partition black and brown carbon absorption in

the short UV-B wavelengths. Next, the BrC effect on reducing biologically harmful UV-B (305 – 320 nm) radiation reaching the surface is quantified. Finally, the retrieved spectral absorption properties are compared with other instruments (AERONET CIMEL sunphotometer and SKYNET skyradiometer).

Chapter 2: Instrumentation and Methodology

2.1. Instrumentation and data

2.1.1. MFRSR

To address the lack of spectral aerosol and gaseous absorption measurements in UV, a suite of complementary ground-based instruments was established in 2005 and is currently in use at the AERONET calibration site at Goddard Space Flight Center (GSFC) in Greenbelt, Maryland. The UV and VIS-MFRSR instruments (Yankee Enviromental systems, INC) are part of the USDA UV-B Monitoring and Research Program (UVMRP). They provide 1-minute measurements of diffuse, direct normal and total irradiance voltages. One cycle of MFRSR measurement comprises (1) total horizontal irradiance (no Sun blocking, V_{tot} in Figure 2.1), (2) blocking the Sun (V_{blk} in Figure 2.1), and (3) blocking sky irradiance on each side of the Sun (at 9°) (V_{se} and V_{sw} in Figure 2.1) with different positions of the shadowband. Equations (2.1) to (2.5) describe how total, diffuse, and direct normal irradiance are calculated from the measured voltages. Direct beam irradiance is calculated from equation (2.5) using all 4 shadowing measurements (~ten seconds). The shadowing cycle is repeated every minute through a day.

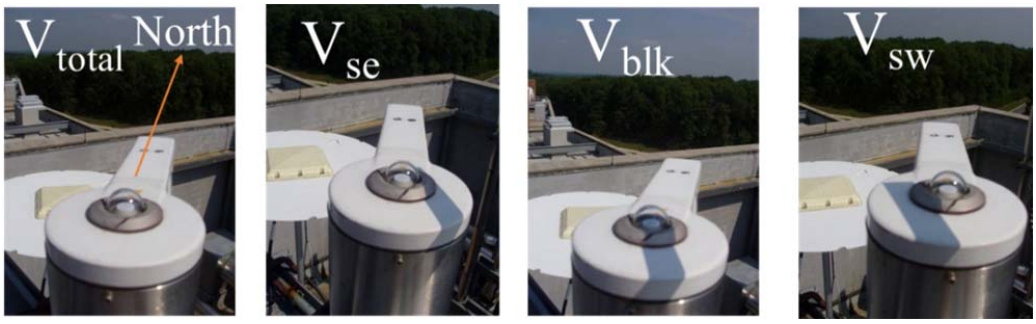

Figure 2.1. Four-step measurement cycle of the MFRSR instrument.

$$V_{tot} = I_{sun} + I_{sky} + I_{aureole} \tag{2.1}$$

$$V_{blk} = I_{sky} \tag{2.2}$$

$$(V_{se} + V_{sw})/2 = I_{sun} + I_{sky} \tag{2.3}$$

$$\begin{aligned} V_{dif} &= V_{blk} + (V_{tot} - (V_{se} + V_{sw})/2) \\ &= I_{sky} + \left(I_{sun} + I_{sky} + I_{aureole} - \left(I_{sun} + I_{sky}\right)\right) = I_{sky} + I_{aureole} \end{aligned} \tag{2.4}$$

$$V_{dir} = V_{tot} - V_{dif} = \left(I_{sun} + I_{sky} + I_{aureole}\right) - \left(I_{sky} + I_{aureole}\right) = I_{sun} \tag{2.5}$$

$$V_{dirn} = V_{dirh} \,/\, \cos(SZA) \tag{2.6}$$

where I_{sun}, I_{sky}, and $I_{aureole}$ means the measurements of irradiance of the Sun, sky, aureole, respectively. SZA is the solar zenith angle. V_{dirn} is the direct normal voltage and V_{dirh} is the direct horizontal voltage.

The commercial UV-MFRSR contains seven interference filter photodiode detectors (300, 305, 311, 317, 325, 332, and 368 nm) with a 2-nm full width at

half maximum (FWHM) bandwidth [Chen et al., 2013]. Also, the commercial VIS-MFRSR consists of six narrowband channels (415, 500, 615, 673, 870, and 940 nm) and an unfiltered (open) silicon photodiode with a 10-nm FWHM bandwith [Harrison et al., 1999]. To facilitate the AERONET-to-MFRSR calibration transfer and to compare derived aerosol absorption products, the 300-nm MFRSR filter of the UV-MFRSR-527 was replaced with the 440-nm filter, which was also used by the AERONET. Since 2010, new modified UV-MFRSR-582 with replaced AERONET filters (300 nm → 440 nm, 317 nm → 340 nm, 368 nm → 380 nm) has been in operation at GSFC. Since 2012, new modified VIS-MFRSR-579 with replaced AERONET 440-nm filter has been installed.

All spectral channels in the MFRSR are measured within one second by seven separate solid-state detectors with interference filters sharing a common Teflon diffuser. The raw data (voltages) are calibrated on-site against the co-located reference AERONET CIMEL sunphotometers (data available at http://aeronet.gsfc.nasa.gov) as discussed in Section 2.2 and 2.3.

2.1.2. AERONET

The AERONET (Aerosol Robotic Network) CIMEL sunphotometer consists of two collimators for measuring the direct Sun and sky radiance and robotic Sun- and sky-tracker. The Sun-tracking radiometer makes direct Sun measurements with a 1.2° full field of view every 15 minutes at 8 channels from

UV to near-infrared (NIR) (340, 380, 440, 500, 675, 870, 940, and 1020 nm). The accuracy of AOD for the reference AERONET instruments at GSFC is typically ~0.003 to 0.01 in the visible with larger errors (~0.02) in the UV. The measurements of sky radiance comprise scanning the sky along the principle plane and different azimuth angles at a fixed zenith angle to obtain radiances as a function of scattering angle (e.g., almucantar scan). Through the inversion technique using almucantar scan at 440, 670, 870, and 1020 nm [Dubovik et al., 2000; Dubovik and King, 2000], particle size distribution, single scattering albedo, index of refraction, and scattering phase function of aerosol are retrieved.

2.1.3. Pandora/Brewer/OMI O_3 and NO_2

The Pandora spectrometer system was developed to measure gaseous absorptions of NO_2, SO_2, and O_3 using Differential Optical Absorption Spectroscopy (DOAS) technique. The Pandora spectrometer measures Sun and sky radiance from 280 to 525 nm [Herman et al., 2009; Tzortziou et al., 2012]. It is mounted on the Sun-tracker, which is automatically controlled by a computer. Before the installation of the Pandora spectrometer, a co-located Brewer spectrophometer was used for measuring column densities of the trace gases. If neither Pandora spectrometer nor the Brewer spectrophotometer were available, satellite O_3 and NO_2 data were used from Ozone Monitoring Instrument (OMI) on board NASA's Aura satellite.

2.2. MFRSR modification and calibration at NOAA CUCF laboratory

All MFRSR instruments in UVMRP network are have been periodically characterized for their spectral (Figure 2.2), angular (Figure 2.3) and radiometric responses at the NOAA Central UV Calibration Facility (CUCF) in Boulder, Colorado. In our on-site daily calibration procedure [Krotkov et al., 2005b], I use only the CUCF's spectral and angular responses for each channel combined with the co-located AERONET AOD and Brewer/Pandora/OMI gaseous measurements to determine the extraterrestrial calibration constant (V_0) for each one-minute measurement and each spectral channel. The version 2 level 2.0 AERONET AODs at 340, 380, 440, and 500 nm are interpolated in time and wavelength and compared with the MFRSR measurements of the corrected direct-normal voltages (more details in Section 2.3) to derive more accurate daily V_0 calibration compared to the standard UVMRP Langley calibrations (http://uvb.nrel.colostate.edu) [Krotkov et al., 2005b].

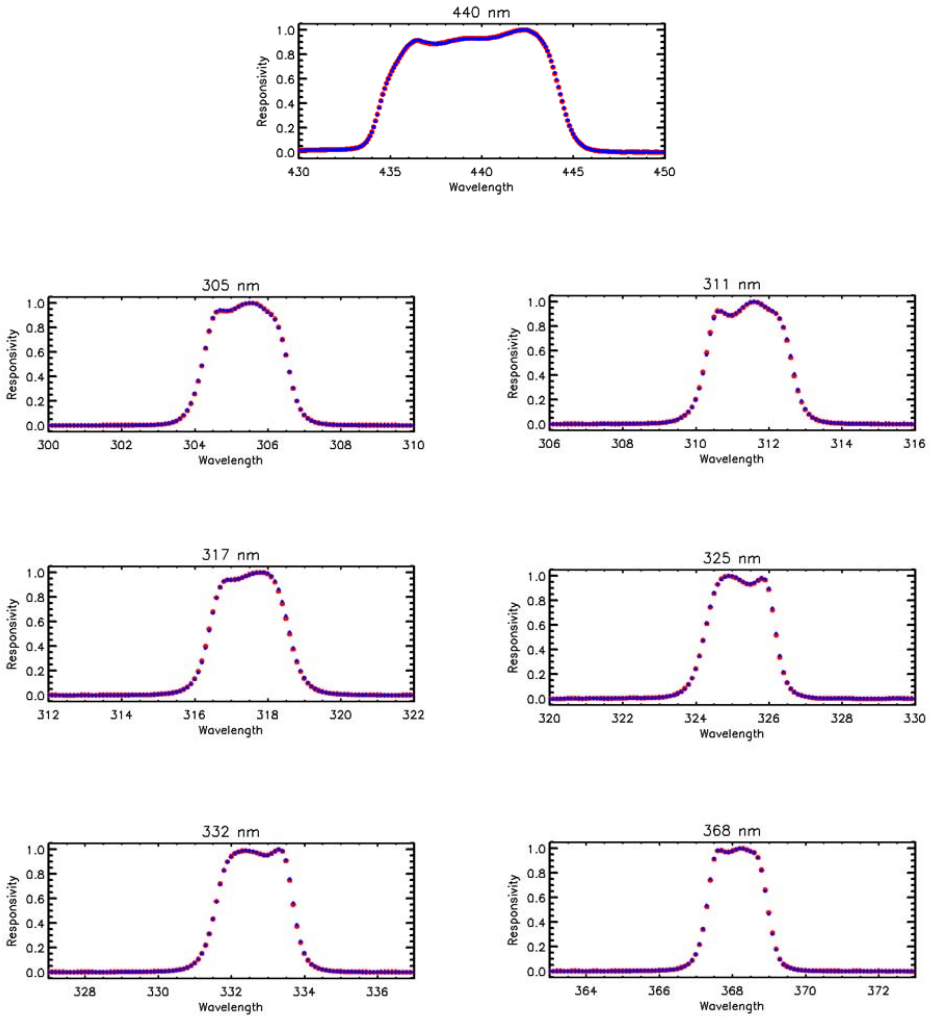

Figure 2.2. CUCF measured spectral response functions (SRF) of UV-MFRSR-527 for nominal 440, 305, 311, 317, 325, 332, and 368 nm channels [Courtesy to Charles Wilson from the NOAA CUCF laboratory in Boulder, Colorado]. A standard 300-nm filter has been replaced with the AERONET 440-nm filter. Red dots show the SRF measured in 2012. Blue dots show the SRF measured in 2013. The SRFs show MFRSR stability between the two lab calibrations.

The CUCF angular calibrations are utilized to perform angular (cosine) correction of the raw direct irradiance measurements and calculate the diffuse correction factor assuming isotropic illumination. Since a quartz dome was

installed on the top of the MFRSR diffuser to stabilize long-term throughput, lab calibrations with the dome were performed to account for the differences in the cosine and spectral responses with and without dome. It did not show any significant differences either with or without the dome. Figure 2.3 shows that the angular response of the UV-MFRSR-527 changed between 2007 and 2012 calibrations. The change was mostly confined to illumination angles larger than ~65° and resulted in small (~2.4%) decrease in diffuse cosine correction factor (DCF) at 440 nm (from 1.02 in 2007 to 0.996 in 2012). Nevertheless, the small change in DCF has important implication for SSA inversion, i.e., reduction of 0.01 in DCF results in approximate increase in SSA retrieval by 0.01. Applying the 2012 CUCF angular calibrations calibration to the measurements in 2010 through 2012 resulted in significant improvements in V_0 calibrations and also removed the previous low bias in the MFRSR SSA inversions.

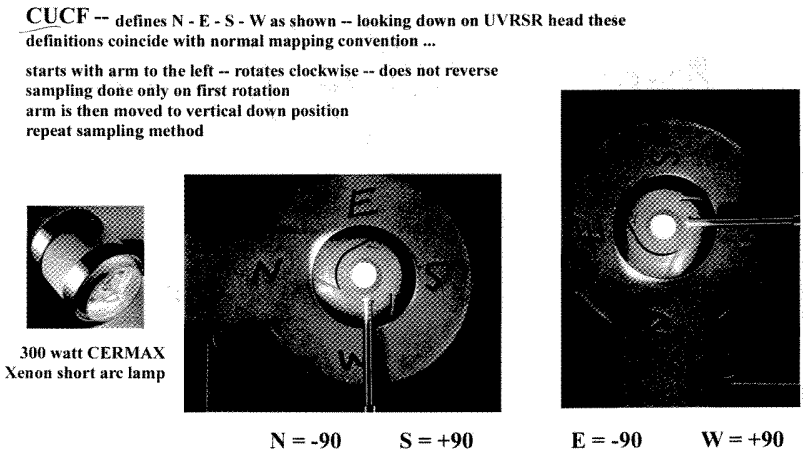

(a)

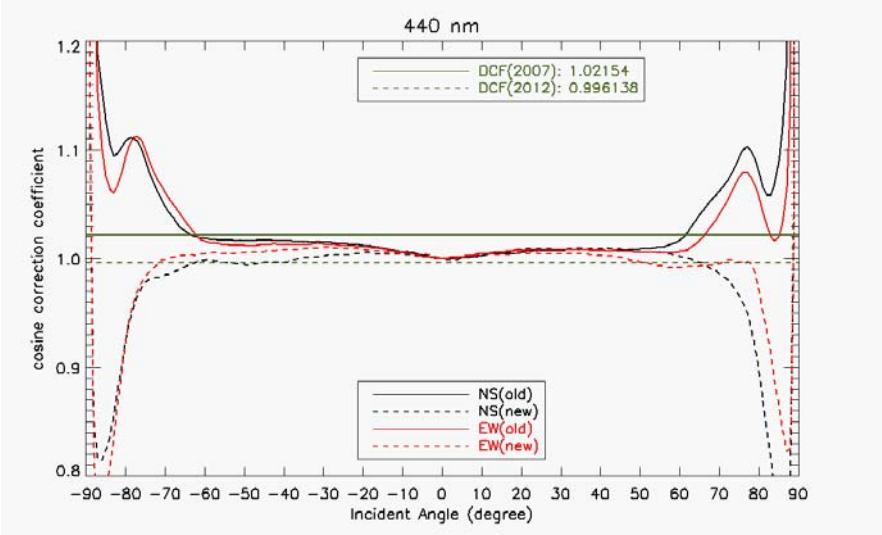

(b)

Figure 2.3. (a) The setup of angular response measurements (lamp and MFRSR geometry) at the CUCF Laboratory [Courtesy to Charles Wilson from the NOAA CUCF laboratory in Boulder, Colorado] and (b) calibration measurements of the UV-MFRSR-527 instrument angular response normalized to the ideal (cosine) response. Black lines show angular response in the North-South azimuthal plane and red lines in the East-West azimuthal plane. Large changes were found for oblique illumination angles larger than 60°. Horizontal lines correspond to diffuse cosine correction factors (assuming isotropic illumination) – 1.02 in 2007 and 0.996 in 2012.

2.3. MFRSR on-site calibration

Improving the MFRSR observational protocol and daily on-site "soft calibration" are both critical for accurate measurements of aerosol column absorption. The MFRSR on-site calibration is determined via daily comparisons with the reference AERONET sun-photometers.

I use the time-resolved (one minute) estimates of the MFRSR calibration constant (i.e., extraterrestrial voltage, V_0) calculated using equation (2.7) to normalize measured direct and diffuse voltages and as a diagnostic tool to select best quality measurements consistent with AERONET AOD measurements. The outlier measurements with $\ln(V_0)$ exceeding 2 standard deviations from dally average $\langle V_0 \rangle$ are iteratively removed and $\langle V_0 \rangle$ is re-calculated as described in Krotkov et al. [2005a]. Any low-frequency diurnal V_0 variability indicates possible systematic errors (e.g., not perfect alignment or shadowing or electronics problems). To reduce systematic errors and outliers, time periods are selected when V_0(time) ~ constant [Krotkov et al., 2005a] and retain only those MFRSR measurements meeting quality assurance criteria (Table 2.1).

$$\ln V_0(t) = \ln V_{dirn} + \sec(SZA)\,[\tau_a + \tau_R + \tau_{NO_2} + \tau_{O_3}] \qquad (2.7)$$

where V_{dirn} is the MFRSR-measured direct normal voltage, τ_a is the interpolated AOD to the MFRSR wavelengths and time using the AERONET

AOD at 340, 380, 440 and 500 nm (Figure 2.4), τ_R is the Rayleigh optical depth inferred from surface pressure, and τ_{NO_2} and τ_{O_3} are NO_2 and ozone optical depths, taken from a Pandora spectrometer or a Brewer spectrophotometer or OMI measurements.

Table 2.1. Quality assurance of the MFRSR measurements.

1. SZA < 75°
2. time periods ln(V_0) ~ constant

   standard deviation (StDev) of ln(V_0) < 0.01 (1%)
3. Iteratively remove outliers outside ±2StDev {ln(V_0) – ln(<V_0>)}

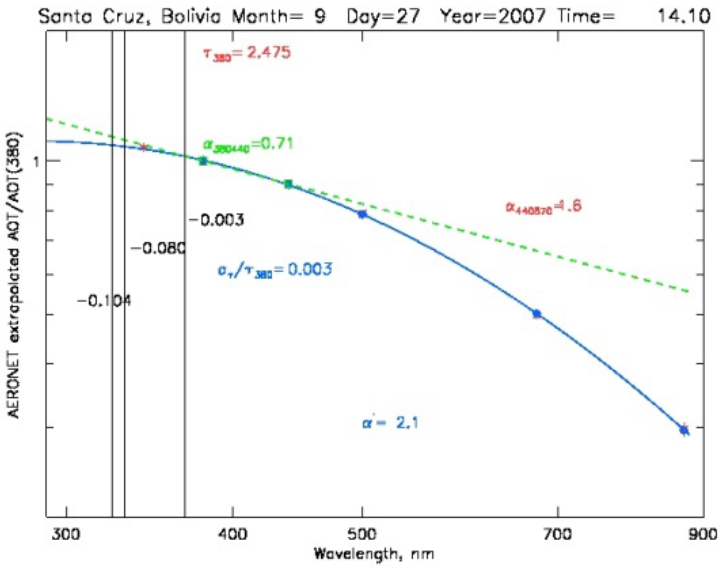

Figure 2.4. Interpolated AERONET AOD to the MFRSR effective wavelengths and time. The blue line show the quadratic polynomial interpolation of ln(AOD) versus ln(wavelength).

Using the best quality of the MFRSR measurements within the selected time period, mean V_0 value for a given day ($<V_0>$) is calculated and then MFRSR AOD values ($\tau_{a(MFRSR)}$) are calculated from the equation (2.8).

$$\tau_{a(MFRSR)} = \cos(SZA) \ln(\langle V_0 \rangle / V_{dirn}) - \tau_R - \tau_{NO_2} - \tau_{O_3} \quad (2.8)$$

Finally, the measurements are only used when RMS ($\tau_{a(MFRSR)} - \tau_{a(AERONET)}$) < 0.01 for Δ time < 3 minutes.

2.3.1. Night-time bias correction

Night-time bias is a stray current or voltage produced by the electronics in the absence of light [Krotkov et al., 2005a]. The magnetic field in the presence of alternating current (AC) generates these biases. To correct the bias, the average of night-time measurements within one hour of the minimum solar elevation angle during night proceeding to the measurements is calculated. If the previous night bias is not available, the average bias for the previous month is used instead. The bias does not affect the V_0 since the direct voltage is already bias-corrected, which means the direct horizontal voltage is calculated as the difference between total and diffuse measurements that have the same bias. However, the bias affects the SSA inversion, because the ratio of diffuse to direct (DD) can change.

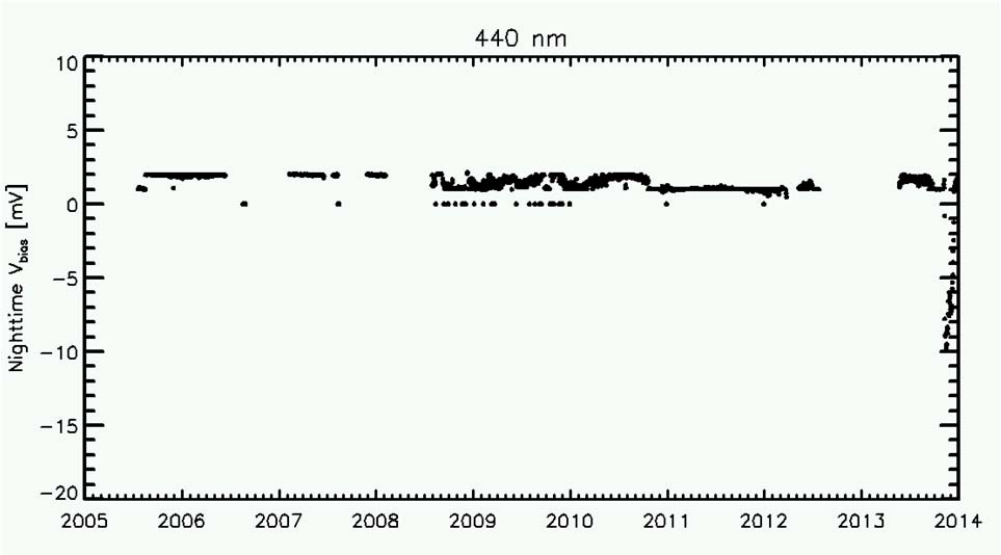

Figure 2.5. Time series of night-time voltage biases [mV] in the 440-nm channel from 2005 to 2013. Most periods show night-time voltage biases within 2 mV. However, night-time biases sharply increased during the period from November to December 2013.

2.3.2. Cosine correction

The angular response function for an ideal instrument follows cosine function of the illumination angle. However, actual angular response for a real instrument deviates considerably from the ideal cosine response. The angular response of the MFRSR instrument (Figure 2.6) was periodically measured at the CUCF laboratory using collimated illumination source (Figure 2.3). For direct normal irradiance, measured angular response factor is interpolated according to solar zenith and azimuth angle. For diffuse irradiance, the diffuse correction factor is determined assuming isotropic sky illumination [Krotkov et al., 2005b;

Leszczynski et al., 1998].

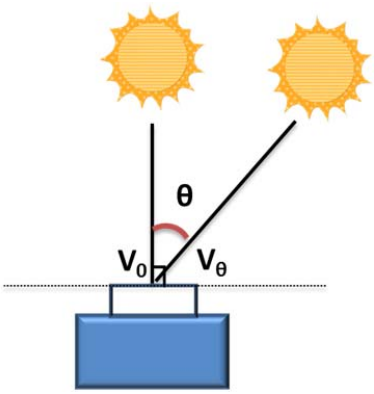

Figure 2.6. The angular response of an instrument (=V_θ / V_0) (θ: SZA, V_0: voltage measured at θ = 0, and V_θ: voltage measured at SZA= θ).

2.3.3. Tilt correction

An instrumental tilt is one of the main error sources of MFRSR [Alexandrov et al., 2007]. The possible tilt of MFRSR produces an incorrect SZA calculation, which leads to inappropriate calculation of direct normal voltage through the equation (2.6). Thus, the tilt affects cosine correction of the direct normal voltage. To reduce tilt effects, I apply tilt correction determining such tilt angles (zenith θ_t and azimuth φ_t tilt angles in equation (2.10) and (2.11)) that flatten V_0 diurnal dependence. Tilt correction is performed in conjunction with cosine correction (Figure 2.7). Through the tilt correction, cosine and tilt corrected voltages are re-calculated using actual SZA (θ' in equation (2.13)).

$$\ln V_0 = \ln \frac{V_{dirh}}{\cos \theta} + m\tau_{TOT} \tag{2.9}$$

$$\theta = \theta' + \theta_t \tag{2.10}$$

$$\varphi = \varphi' + \varphi_t \tag{2.11}$$

$$\ln V_0 = \ln \frac{V_{dirh}}{\cos (\theta - \theta_t)} + m\tau_{TOT} \tag{2.12}$$

$$\cos \theta' = \cos \theta \cos \theta_t + \sin \theta \sin \theta_t \cos(\varphi - \varphi_t) \tag{2.13}$$

where τ_{TOT} is the total optical depth of the atmosphere (see more details in equation (2.14)). θ, φ are the nominal solar zenith and azimuthal angles, respectively assuming tilt angle is zero. θ', φ' are the actual solar angles accounting for the instrumental tilt angles: θ_t, φ_t (zenith and azimuth) [c.f., Alexandrov et al., 2007].

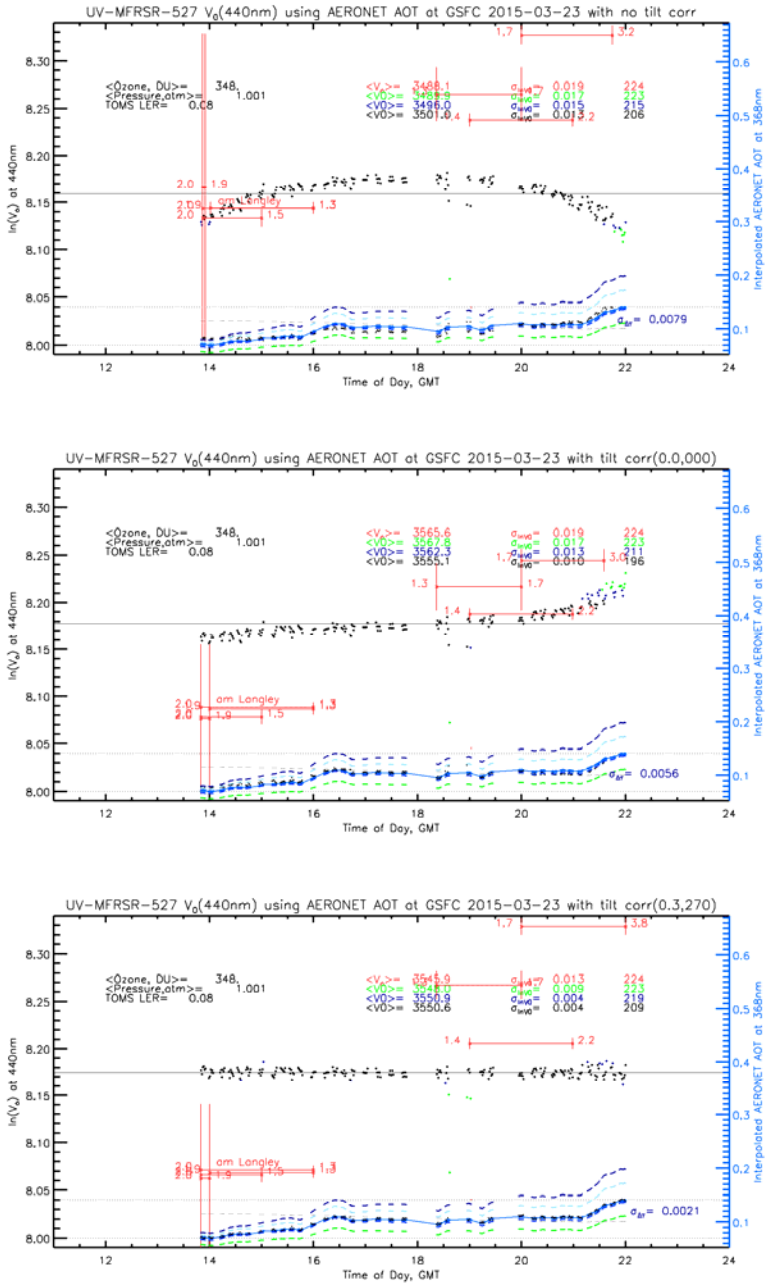

Figure 2.7. Using daily V_0 plot for diagnostics. (Top) Raw voltages (no angular correction) show pronounced diurnal V_0 dependence on solar zenith angle. (Middle) Angular calibration applied to raw voltages makes V_0 dependence flat, but not constant with SZA. (Bottom) Applying both angular and tilt correction of 0.3° makes V_0 constant with time (SZA). Constant V_0 means that MFRSR AOD agrees with AERONET AOD and RMSD ~ 0.002 (bottom lines).

The tilt correction will help calculate correct V_0 (equation 2.12). In addition, tilt correction allows processing additional morning and evening measurements with high SZA ~ 75° as shown in the Figure 2.7. Thus, tilt correction allows more matchups with AERONET morning and evening almucantar inversions that require high SZA > 50° [Dubovik and King, 2000].

2.3.4. Gaseous absorption correction

We combine Pandora spectrometer, Brewer spectrophotometer, and Aura/OMI to measure ozone and NO_2 column densities. In rare cases, when none of these instruments are available, we use the climatological ozone and NO_2 from the AERONET database. To convert the column amounts of gases into optical depth, we use laboratory measured high spectral resolution absorption coefficients and convolve them with the MFRSR spectral response functions (SRF) (Figure 2.2). Currently, we neglect minor absorption by water vapor and SO_2:

$$\begin{aligned}\tau_{TOT}(\lambda) &= \tau_R(\lambda) + \tau_a(\lambda) + \tau_{O_3}(\lambda) + \tau_{NO_2}(\lambda) \\ &= \beta(\lambda)\frac{P}{P_o} + \tau_a(\lambda) + \alpha_{O_3}(\lambda,T)\Omega + \alpha_{NO_2}(\lambda,T)N\end{aligned} \tag{2.14}$$

where P: atmospheric pressure [hPa], P_0: 1013.25 [hPa], τ_R is Rayleigh optical depth, τ_a is aerosol optical depth, τ_{O3}: ozone optical depth, τ_{NO2}: NO_2 optical depth,

$\alpha_{O_3}(\lambda,T)$: ozone absorption coefficient [atm·cm^{-1}], Ω: ozone column density [molec./cm^2] or [atm·cm], 1 atm·cm = 10^3 Dobson Units (DU = 2.69×10^{16} molecules·cm^{-2}), $\alpha_{NO_2}(\lambda,T)$: NO_2 absorption coefficient, N: NO_2 column density [atm·cm].

2.3.5. Surface pressure correction

AERONET uses the NCEP/NCAR reanalysis pressure interpolated to the altitude of the AERONET sites. To confirm the pressure AERONET used, I compared it with the measured pressure by the Sutron barometric pressure sensor installed on the roof of Building 33 at NASA Goddard Space Flight Center. Additional information about the pressure sensor is available at http://www.sutron.com/product/accubarbarometric-pressure-sensor-5600-0120/.
Blue dots in the upper panel of Figure 2.8 show the NCEP/NCAR reanalysis pressure and red dots show the measured pressure with accuracy ~0.5 mb. The difference between the interpolated NCEP/NCAR reanalysis pressure and the measured pressure is within 2 – 4 mb shown in the lower panel in Figure 2.8. The uncertainty of pressure affects the calculation of the Rayleigh optical thickness and V_0 (equation (2.7) and (2.14)). The introduced maximal V_0 errors using NCEP pressure are shown in Table 2.2. The corresponding error in AOD is proportional to cos(SZA) and is half of the V_0 error at SZA=60° (equation (2.8)).

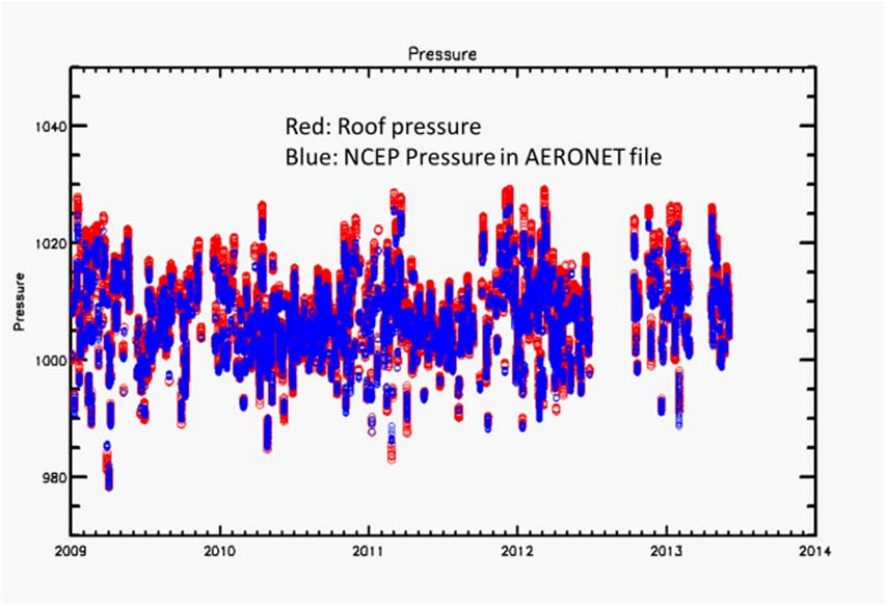

(a)

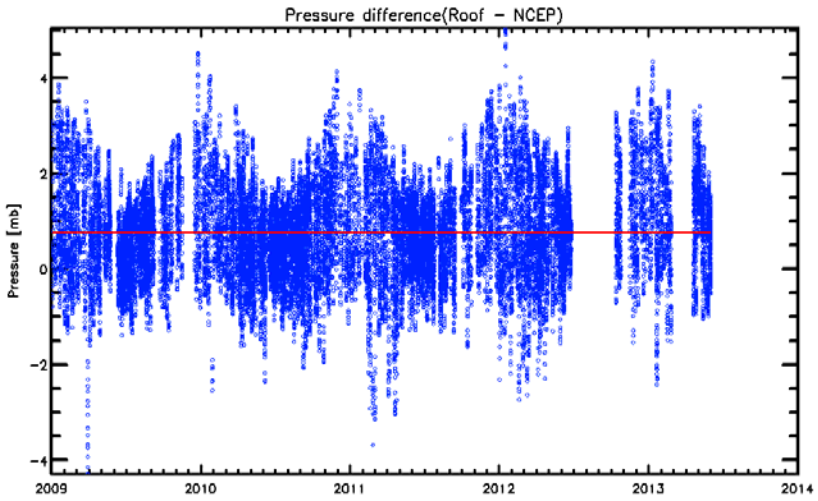

(b)

Figure 2.8. Time series of (a) the NCEP pressure interpolated to the time measurements performed at the AERONET site (blue) and the Sutron pressure measured on the roof of Bldg. 33, GSFC, NASA (red) and (b) their differences (blue dots) and the mean of differences (red line).

Table 2.2. V_0 errors due to uncertainty in Rayleigh optical depth derived from the pressure difference.

Source of error	440 nm	368 nm	332 nm	325 nm
Pressure: ±2mb	0.001	0.002	0.005	0.005

2.4. MFRSR inversion technique

The inversion technique uses the simultaneous AOD measurements from co-located AERONET CIMEL sunphotometer and UV-MFRSR instruments to ensure (1) accurate and consistent measurements of the spectral aerosol extinction optical depth (AOD), (2) consistent assumptions about surface reflectance, aerosol size distribution, and real part of the effective complex refractive index [Krotkov et al., 2005a; 2005b].

The primary data set consists of one–minute measurements of diffuse and total irradiance transmittances by MFRSR (Section 2.1.1) and 15 minute AOD measurements by AERONET (Section 2.1.2) [Holben et al., 2001]. The AERONET level 2.0 AOD at 340, 380, 440, and 500 nm were interpolated in time and wavelength [Eck et al., 1999] and compared with the UV-MFRSR measurements of cosine corrected direct-normal voltages to derive the daily V_0 calibrations, consistent AOD, and dimensionless diffuse and direct atmospheric transmittances [Krotkov et al., 2005a]. To ensure consistency between UV-

MFRSR and AERONET retrievals, I only consider the UV-MFRSR inversions leading to AOD agreeing with the interpolated AERONET AOD within 0.01.

I infer the column effective imaginary part of the refractive index (k) independently at 440 nm and each UV wavelength by fitting UV-MFRSR measured diffuse/direct (DD) irradiance ratios [King and Herman, 1979] with the Mie-RT modeled irradiances (Arizona code [Herman et al., 1975]). Ancillary input parameters, such as surface albedo, the column particle size distribution (PSD), and the real part of the refractive index (n), are taken from near simultaneous level 1.5 AERONET inversions (within 8 minutes). Absorption by trace gases (O_3 and NO_2) was accounted for using a Pandora spectrometer or a Brewer spectrophotometer or Aura/OMI satellite data. The forward Mie-RT model iterates to find the retrieved k value, which minimizes the difference between calculated and measured DD ratio. Details of approach are described in Krotkov et al. [2005b]. Requiring AERONET spherical particle fraction to exceed 95% justifies the sphericity assumption.

Table 2.3. AERONET-MFRSR inversion parameters.

Parameter	Source	Condition	References
	Measurements		
$DD = V_{Diffuse}/V_{Direct}$ $T_{Direct} = V_{Direct}/\langle V_0 \rangle$ or	MFRSR cosine corrected voltage measurements	SZA < 75°	Harrison et al., 1994; Slusser et al., 2000;

$T_{Diffuse} = V_{Diffuse}/\langle V_0 \rangle$ or $T_{Total} = V_{Total}/\langle V_0 \rangle$			Krotkov et al., 2005b
Inversion			
Imaginary part of the column effective refractive index, $k(\lambda)$	MFRSR one parameter inversion separately in each spectral band	Cloud free SZA < 75° $AOD_{440} > 0.2$	Krotkov et al., 2005b
Fixed forward model parameters			
AOD(λ)	AERONET direct sun AOD(340), AOD(380), AOD(440), AOD(500) , level 1.5 interpolated to MFRSR wavelength and time	Un-obscured sun	Holben et al., 1998
Aerosol size distribution	AERONET level 1.5 sun-sky almucantar inversion at 440,670,870,1020 nm	$AOD_{440} > 0.2$ SZA < 75° Sky error < 5%	Dubovik and King, 2000
Real part of the column effective refractive index, $n(\lambda)$	AERONET level 1.5 sun-sky almucantar inversion $n(\lambda) = n_{440}$	Cloud free SZA < 75° $AOD_{440} > 0.2$	Dubovik and King, 2000
Surface pressure	AERONET (NCEP/NCAR reanalysis)		
Surface albedo, A(λ)	AERONET/MODIS surface albedo,440nm: $A(\lambda)=A_{440}$		Moody et al., 2008
Column Ozone and NO_2	Pandora/OMI/Brewer		Herman et al., 2009; Tzortziou et al., 2012

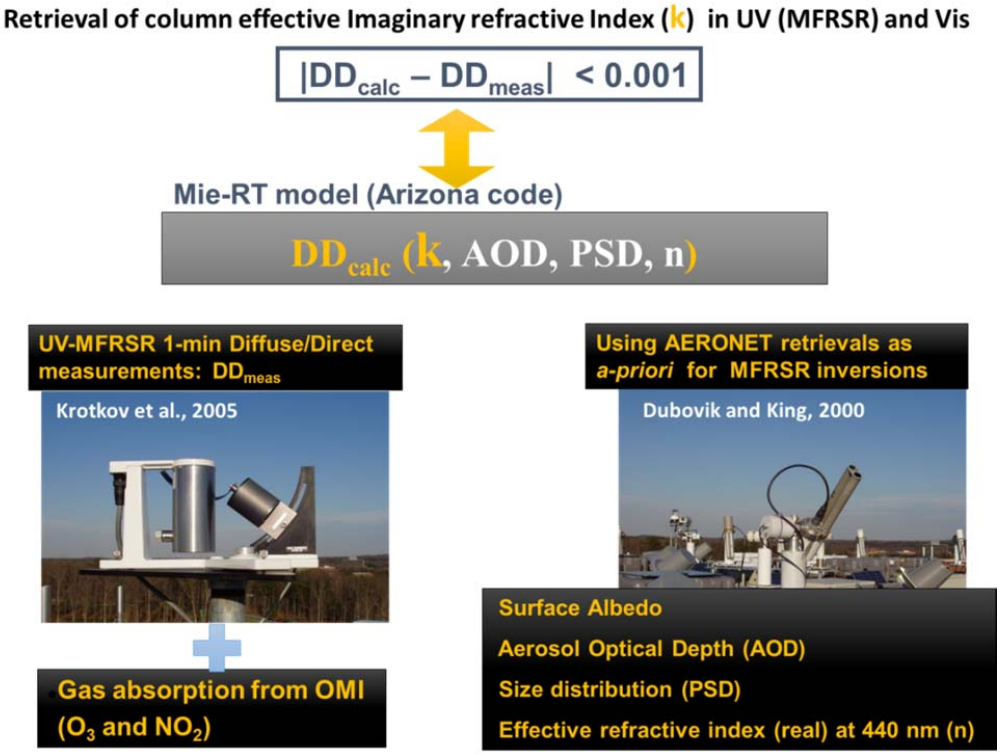

Figure 2.9. Retrievals of column effective imaginary refractive index. Measured diffuse/direct (DD) irradiance ratios are fitted with the Mie-RT model (Arizona code [Herman et al., 1975]) to invert column effective imaginary part of refractive index (*k*). Ancillary input parameters, such as absorptions of trace gases (O_3 and NO_2), surface albedo, particle size distribution (PSD), real part of refractive index (*n*) at 440 nm, are taken from near simultaneous, co-located AERONET level 1.5 inversions. The aerosol extinction optical depth (AOD) is known from either MFRSR or AERONET direct sun measurements. The Mie-RT forward model iterates to find the *k* value, which minimizes the difference between calculated and measured DD. The fitted *k* value together with the AERONET PSD and real part of refractive index at 440 nm is converted to SSA using Mie calculation assuming spherical particles. Requiring AERONET spherical particle fraction to exceed 95% justifies the sphericity assumption.

Next, comprehensive error propagation study is conducted to calculate finite difference Jacobians (J) using combined Mie-RT code to estimate retrieval

errors Δk and $\Delta\omega$:

$$J_{kpar}=\frac{\frac{\Delta k}{k}}{\frac{\Delta par}{par}} \tag{2.15}$$

$$J_{\omega k}=\frac{\frac{\Delta \omega}{\omega}}{\frac{\Delta k}{k}} \tag{2.16}$$

$$\Delta k=J_{kpar}\frac{\Delta par}{par}k \tag{2.17}$$

$$J_{\omega par} = J_{\omega k}J_{kpar} \tag{2.18}$$

$$\Delta \omega=J_{\omega par}\frac{\Delta par}{par}\omega \tag{2.19}$$

where ω is SSA. $J_{\omega par}$ shows the change of ω as function of the change of parameter (expressed as par) (i.e., measured diffuse to direct (DD) irradiance ratio). *k* is the imaginary part of the refractive index.

Using the equation (2.19), errors of SSA ($\Delta\omega$) can be calculated.

Chapter 3: Long-term synergistic measurements of spectral aerosol absorption at AERONET calibration site, GSFC, Greenbelt

3.1. Introduction

Though potential climatic effects of absorbing aerosols have received considerable attention lately [Stocker et al., 2013], their effect on surface ultraviolet (UV) radiation and photochemical smog formation can be equally important for environment and may affect human health and agricultural productivity. Extending our knowledge of aerosol and trace-gas absorption into UV wavelengths is also important for remote sensing of aerosol composition [Martins et al., 2009; Yang et al., 2009; Mok et al., 2016] and accurate modeling of tropospheric photochemistry.

In electromagnetic theory, optical properties of solid or aqueous medium are characterized by the spectral dependence of the complex refractive index, $m(\lambda) = n(\lambda) + ik(\lambda)$. The non-negative real part (n) determines the phase velocity of a plane electromagnetic wave in a medium: $v = c/n$ (c is speed of light in vacuum) and the imaginary part (k) determines intensity absorption coefficient, $\alpha = 4\pi k/\lambda$ ($\lambda = 2\pi c/\omega$ is the vacuum wavelength). For homogeneous particles the refractive index, together with the particle size- and shape- distributions, determines macroscopic absorption and scattering coefficients used in atmospheric radiative transfer theory [Mishchenko et al., 2002; Thomas and Stamnes, 1999]. For

naturally occurring inhomogeneous particles or aerosol mixtures an effective refractive index can be derived through inversions of the measured radiation, provided all other inputs, such as particle mixing state, size- and shape-distributions, and surface reflection, are known or simultaneously retrieved [Herman et al., 1975; King and Herman, 1979; Dubovik et al., 2000]. The spectral dependence of the effective imaginary refractive index, $k(\lambda)$ contains information about aerosol composition and provides insights into aerosol speciation [Mok et al., 2016; Schuster et al., 2016]. Martins et al. [2009] show that the single scattering albedo (SSA) of urban aerosol is considerably smaller in the UV than in visible wavelengths. The increased aerosol absorption in UV wavelengths is mainly associated with the organic aerosol (OA) that absorbs primarily in the UV, explaining considerably stronger wavelength dependence of the absorption coefficient ($\sim\lambda^{-3}$) than a purely black carbon (BC) model would suggest ($\sim\lambda^{-1}$) [Kirchstetter et al., 2004]. Though UV radiation constitutes a small fraction of total incoming radiation on Earth's surface, it is could be important for estimating radiative forcing considering strong absorption in UV [Barnard et al., 2008]. It is therefore important to further develop multi-instrument atmospheric measurement techniques, which allow derivation of the extended spectrum of the refractive index: from near ultraviolet (UV-B and UV-A) through visible to near infrared (NIR) wavelengths.

Column aerosol optical depth (AOD) in visible and UV wavelengths is measured routinely at locations worldwide by NASA's AERONET network [Dubovik et al., 2000; Holben et al., 2001] (http://aeronet.gsfc.nasa.gov) and

SKYNET [Nakajima et al., 1996] and MFRSR instruments [Harrison et al., 1994; ; Slusser et al., 2000; Michalsky et al., 2001; Alexandrov et al., 2007; Kassianov et al., 2005]. Retrievals of column effective aerosol single scattering albedo (SSA, ratio of scattering to extinction) were demonstrated combining AOD with total, diffuse or direct to diffuse ratio (DD) measurements [Eck et al., 1998; Petters et al., 2003; Krotkov et al., 2005ab; Taylor et al., 2008; Corr et al., 2009; Kazadzis et al., 2016] as well as using spectrometers [Harrison et al., 1999; Bais et al., 2005; Barnard et al., 2008; Ialongo et al., 2010]. With few exceptions [Bais et al., 2005; Kazadzis et al., 2016] previous SSA retrievals were obtained during short field campaigns and not typically available on routine basis for multi-year periods. More importantly, since SSA depends not only on refractive index, but also on aerosol mixing state and size-distribution, its conversion to refractive index is not straightforward and has not been demonstrated.

To address the lack of spectral aerosol refractive index measurements in the UV, a suite of complementary ground-based instruments (Table 2.3) was established during 2002-2005 and is currently in use at NASA Goddard Space Flight Center in Greenbelt, Maryland. The primary data set consists of 1-minute measurements of diffuse and total irradiance collected with the UV-MFRSR instrument (Yankee Env.) part of UV-B Monitoring and Research Network (UVMRP). To facilitate AERONET to MFRSR calibration transfer and to compare single scattering albedo products, the 300-nm MFRSR filter was replaced with 440-nm filter used in AERONET network. Daily V_0 calibrations (using cloud-free periods) [Krotkov et al., 2005a] were performed from 2005 to

2014 by applying tilt corrections and new gaseous corrections applied for ozone and NO_2.

3.2. Long-term MFRSR calibration stability

Monitoring the behavior of the daily average extraterrestrial voltage (V_0), calibration constant from the combined AERONET-MFRSR calibration allows tracking of V_0 long-term change as shown in Figure 3.1. It was found that the UV-MFRSR-527 had relatively good day-to-day calibration stability (± 1% in daily average), but larger than expected V_0 changes were observed on seasonal and inter-annual time scale (Figure 3.1). Quartz dome was installed atop the diffuser in 2007, which stabilized long-term throughput. Since spring 2007 the modified UV-MFRSR-527 was continuously operated with a dome at NASA/GSFC site, except during few field campaigns. I have re-processed all daily V_0 calibrations (using cloud-free periods) from 2005 to 2014 applying tilt and cosine corrections (equation (2.13)) and new gaseous corrections for ozone and NO_2 (equation (2.8)). I have applied night-time voltage measurements and found that these corrections are important to retrieve the SSA. The cosine corrected diffuse and total (diffuse plus direct) voltages are divided by daily average V_0 to obtain dimensionless solar normalized direct, diffuse and total transmittances: $T_{Direct} = V_{Direct}/V_0$, $T_{Diffuse} = V_{Diffuse}/V_0$, and $T_{Total} = V_{Total}/V_0$.

The dimensionless transmittances or their ratios can be directly compared with radiative transfer (RT) model results. Since daily calibrations require direct

sun illumination, they are performed on clear days or days with scattered clouds. On such days the cosine corrected diffuse to direct irradiance ratio, DD = $V_{Diffuse}/V_{Direct}$ was directly fitted to the RT model.

After the instrument started operations at GFSC in July 2005, V_0 measurements decreased gradually over time and reached a minimum sun-Earth distance corrected value ($\ln(r^2V_0) \sim 7.95$ at 440 nm) in summer 2006. This was likely due to diffuser soiling [Krotkov et al., 2005a]. A quartz dome was then installed on top of the diffuser in 2007. This stabilized the long-term throughput at longer channels. Due to a quartz dome and improved calibration (Chapter 2.3), the calibration factor (V_0) in UV-MFRSR (head 527) has been stable within ±2% including field campaign periods [Thessaloniki, Greece for summer 2006; Santa Cruz, Bolivia for fall 2007; Xianghe, China for spring 2008] as seen in Figure 3.1. The substantial increase of V_0 in 2013 was caused by the refurbishment of the UV-MFRSR-527. The installation of new diffuser and dome in 2013 contributed to the ~13% increase in V_0 because the newly built diffuser and dome were pristine.

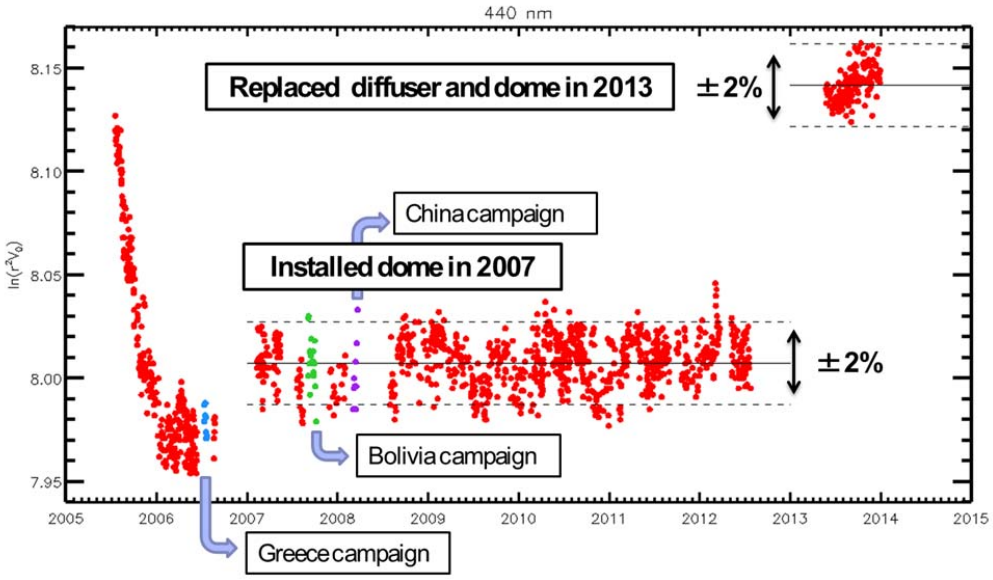

Figure 3.1. Time series of UV-MFRSR ln(V_0) normalized to the 1 AU Sun-Earth distance from 2005 to 2014. (Red dots: GSFC, Blue dots: Greece campaign, Green dots: Bolivia campaign, and Purple dots: China campaign). The initial downward trend in V_0 was attributed to observed changes in the throughput of the UV-MFRSR instrument, likely due to diffuser soiling [Krotkov et al., 2009].

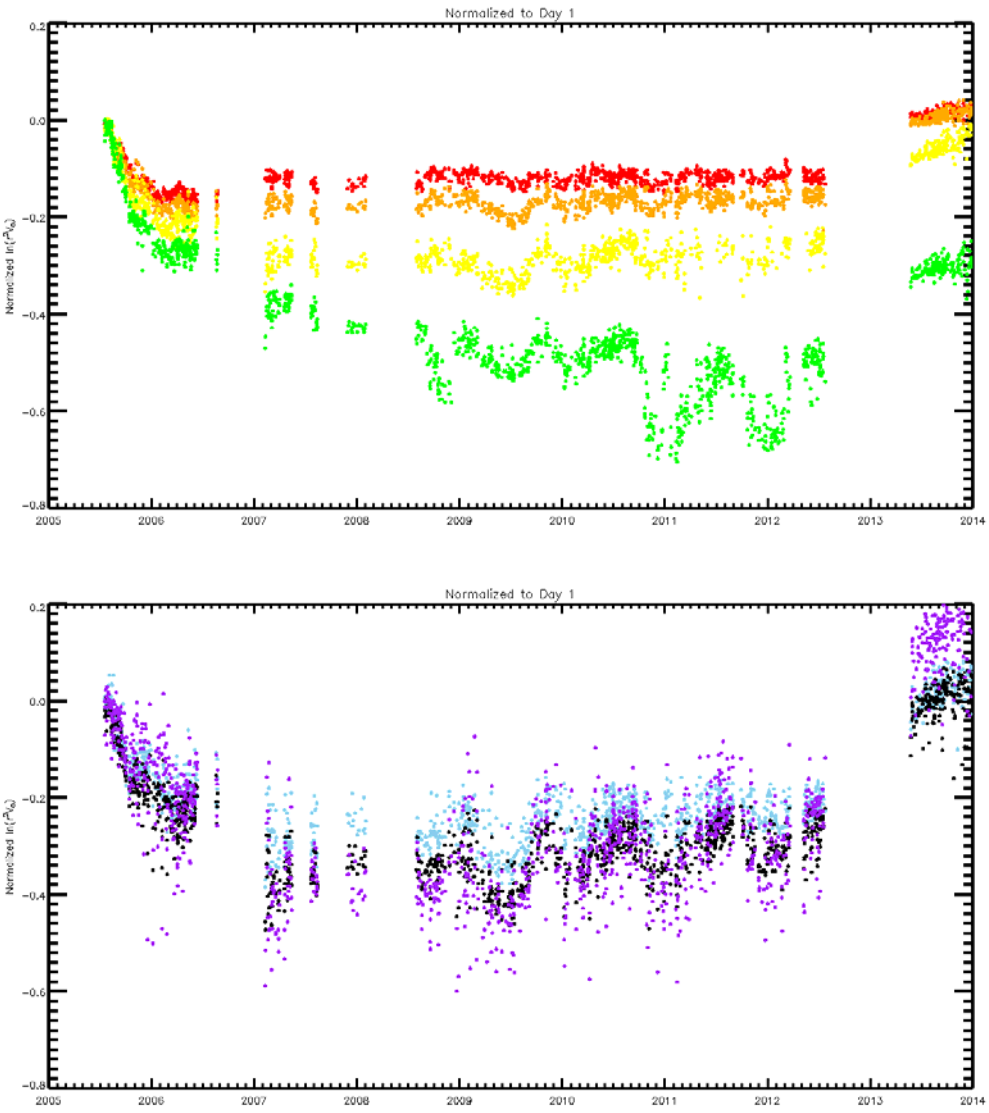

Figure 3.2. Upper panel: UV-MFRSR normalized daily V_0 calibration results at 4 longer UV-A wavelengths: V_0(440 nm) - red, V_0(368 nm) - orange, V_0(332 nm) – yellow, and V_0(325 nm) – green. Lower panel: same at 3 shorter UV-B wavelengths: V_0(317 nm) – sky blue; V_0(311 nm) – black; V_0(305 nm) – purple. In each channel the V_0 calibrations were normalized to Day 1 calibration (July 20 2005) to emphasize the spectral dependence of the long-term calibration drift. An increment of 0.01 corresponds to 1% change in V_0.

3.3. Comparisons between MFRSR and AERONET SSA inversion

Currently routine ground measurements of spectral absorption optical depth (or column effective single scattering albedo, SSA) are limited to the four discrete visible wavelength bands by the AERONET almucantar inversions (440, 670, 870, and 1020 nm). AERONET CIMEL sunphotometer has 340 and 380 channels but does not perform sky radiance measurements for the UV channels.

The long-term average SSA at 440 nm (SSA_{440}) from MFRSR retrieval (~0.969) and that from AERONET retrieval (~0.966) are generally in excellent agreement (Figure 3.3). It also agrees with the AERONET updated SSA climatology (0.96) at GSFC site reported by Giles et al. [2012]

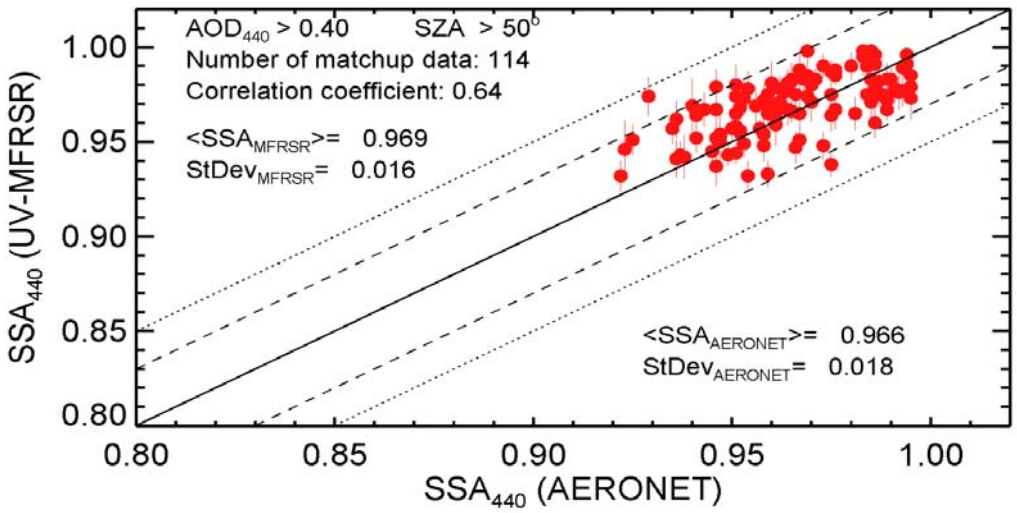

Figure 3.3. Scatter plot between SSA from AERONET almucantar retrievals and SSA retrieved from MFRSR at 440 nm. Retrievals performed at AERONET calibration site at Goddard Space Flight Center in Greenbelt, Maryland under cloud-free conditions. MFRSR SSA errors are calculated assuming 3% error in diffuse to direct ratio. For AERONET default 0.05 SSA errors are assumed. All inversions were filtered to correspond best quality level 2 AERONET data. Long-term average SSA was 0.969 for MFRSR and 0.966 for AERONET.

3.4. Recommendations for relaxing AERONET level 2 screening criteria

The criteria of the best quality of level 2 AERONET data is AOD in 440 nm (AOD_{440}) > 0.4 and solar zenith angle (SZA) > 50°. The criteria are so strict that many inversion data cannot be used especially at the relatively clean sites, such as GSFC. I extended SSA comparisons between MFRSR SSA_{440} with AERONET SSA_{440} relaxing strict SZA and AOD_{440} criteria to investigate possible biases under lower AOD and/or SZA conditions.

3.4.1. Relaxing SZA filter > 30°

Figure 3.4 shows the difference between SSA from the MFRSR retrieval and that from the AERONET binned by SZA. AERONET provides more reliable retrievals of SSA at higher SZA [Dubovik et al., 2002]. Thus, the level 2 criteria of AERONET for SZA are greater than 50º. However, Figure 3.4 shows that the median SSA difference between two retrievals remains less than 0.01 for a smaller SZA > 30º. Extending matchup conditions to a smaller SZA > 30° almost double comparison sample. However, high bias ~0.015 can be seen for smaller 20° < SZA < 30°.

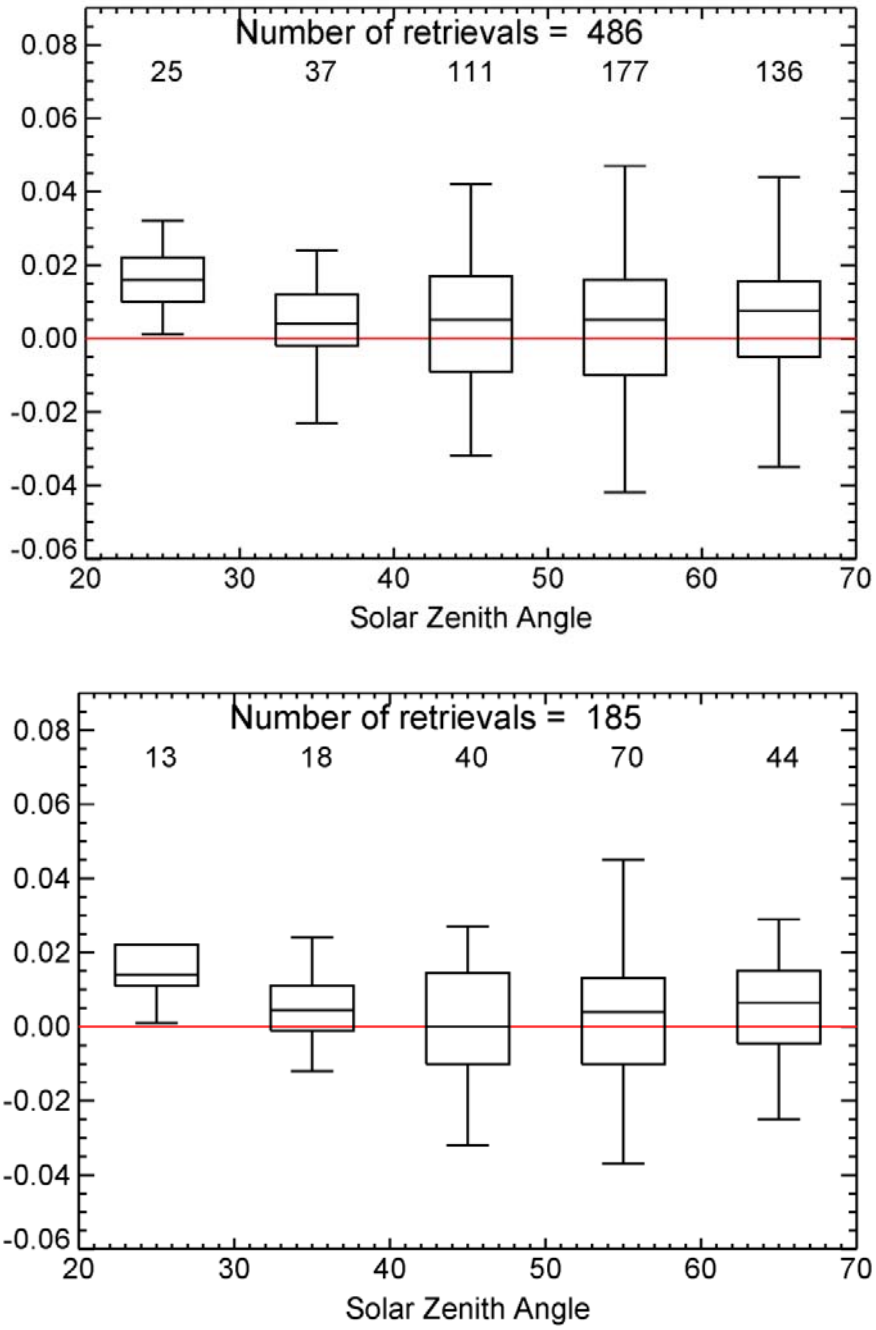

Figure 3.4. SSA difference between MFRSR and AERONET as function of SZA. Upper panel uses the retrievals when AOD_{440} > 0.2 and lower panel uses the retrieval when AOD_{440} > 0.4. The boxes show interquartile range (IQR), between 25 and 75 percentiles. The whiskers are stretched to the maximum and minimum within 1.5 times the IQR.

3.4.2. Relaxing AOD_{440} filter to > 0.2

AERONET provides more reliable retrievals of SSA at higher AOD_{440} > 0.4 [Dubovik et al., 2002]. Figure 3.5 shows the difference in SSA between MFRSR and AERONET retrievals as function of AOD_{440}. The comparison shows that despite increasing variability at lower AODs, the median values of SSA agree better than 0.02 for AOD_{440} > 0.2. Thus, I suggest relaxing AERONET level 2 quality criteria for suburban sites similar to GSFC with fine mode dominated weakly absorbing aerosols to AOD_{440} > 0.2. A summary of the strict and relaxed filters can be found in Table 3.1. This greatly increases the number of high quality refractive index and SSA retrievals available for analysis for relatively clean sites in all seasons.

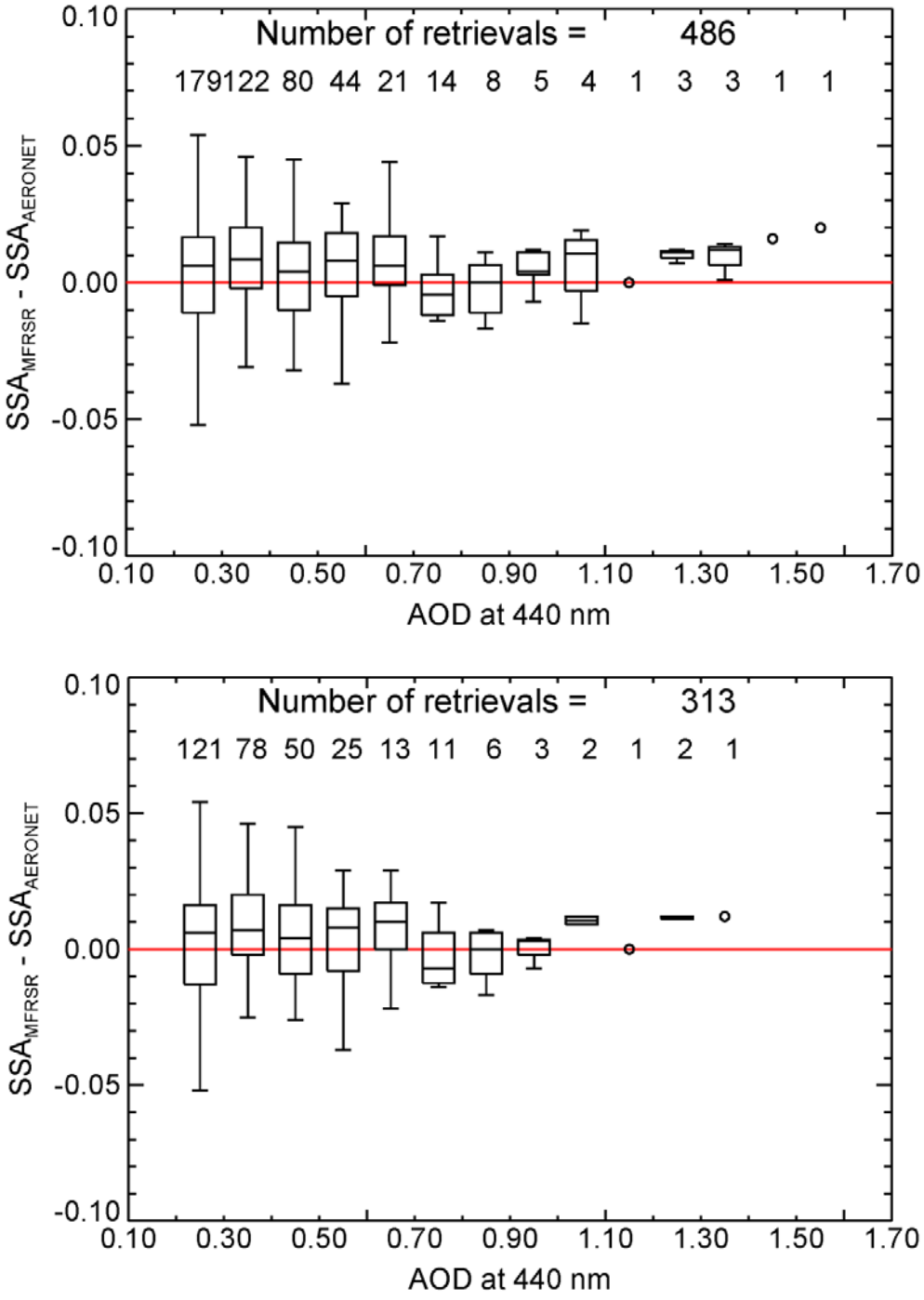

Figure 3.5. SSA difference between MFRSR and AERONET as function of AOD at 440 nm. Upper panel shows the retrievals for SZA ≥ 20°. Lower panel shows the retrievals when SZA ≥ 50°.

Table 3.1. The MFRSR and AERONET matchup selection criteria.

Parameters	Data set	Strict matchups	Extended matchups
Quality assurance level	AERONET	Level 2	Level 1.5
Solar zenith angle		50° – 75°	30° – 75°
AOD at 440 nm	AERONET	> 0.4	> 0.2
Effective sphericity[%]	AERONET	> 95%	> 95%
Sky error [%]	AERONET	< 5%	< 5%
AOD difference	AERONET/MFRSR	< 0.01	< 0.01
SSA error	MFRSR	< 0.02	< 0.02
Time difference	AERONET/MFRSR	< 8 minutes	< 8 minutes

Relaxing both SZA > 30° and AOD_{440} > 0.2 criteria allows analysis of much larger statistical sample (blue and red circles) meeting MFRSR-AERONET matchup criteria shown in Figure 3.6. The extended sample mean SSA_{440} values are lower by ~0.01 compared to stricter level 2 GSFC climatology (red circles in Figure 3.6 and Figure 3.3), and most individual matchups agree within ±0.05 (dotted lines). However, SSA variability (standard deviation) increased by 50% from < ~0.02 (Figure 3.3) to ~0.03 (Figure 3.6). The increased variability reflects cases with smaller AOD, but stronger absorption (SSA ~ 0.9). Such cases excluded from official SSA climatology [Giles et al., 2012], are nevertheless occurred at GSFC site. More complete description of SSA climatology should

include additional parameters describing SSA statistical distribution, e.g., interquartile range (Figure 3.4 and 3.5).

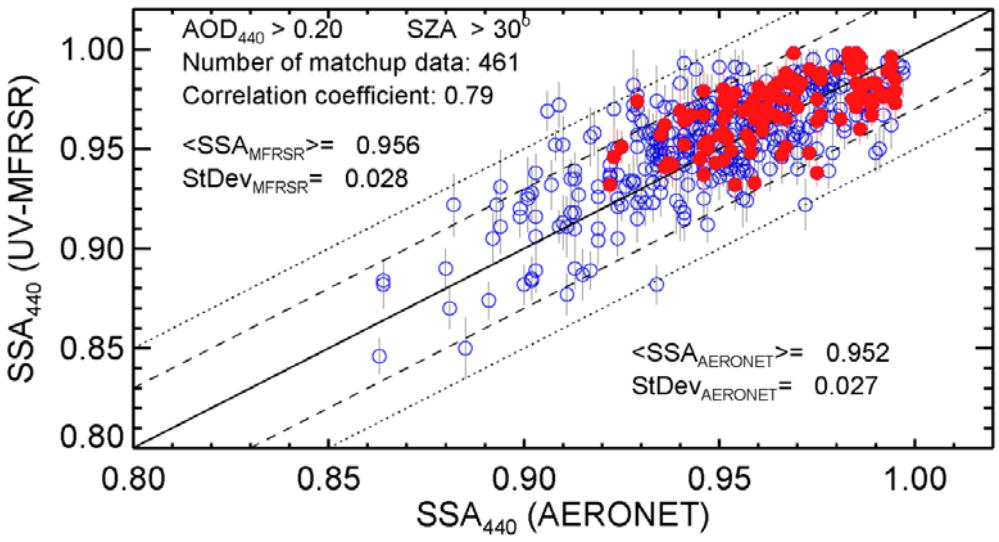

Figure 3.6. Comparison between MFRSR and AERONET single scattering albedo (SSA) at common wavelength 440 nm. Retrievals performed at AERONET calibration site at Goddard Space Flight Center in Greenbelt, Maryland under cloud-free conditions. Red solid circles: AERONET level 2 inversions only. Open blue circles: AERONET level 1.5 inversions satisfying extended matchup criteria (last column in Table 3.1). Vertical bars show MFRSR estimated mean errors. Statistics are calculated for extended matchup sample (Table 3.1): 461 near simultaneous inversions between 2005 and 2014.

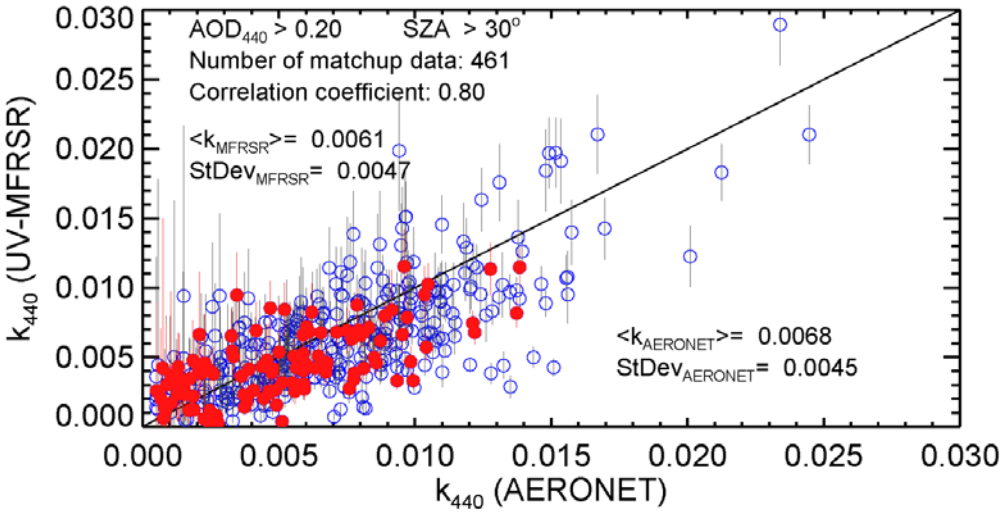

Figure 3.7. Same as Figure 3.6 for the column effective imaginary part of the refractive index (*k*).

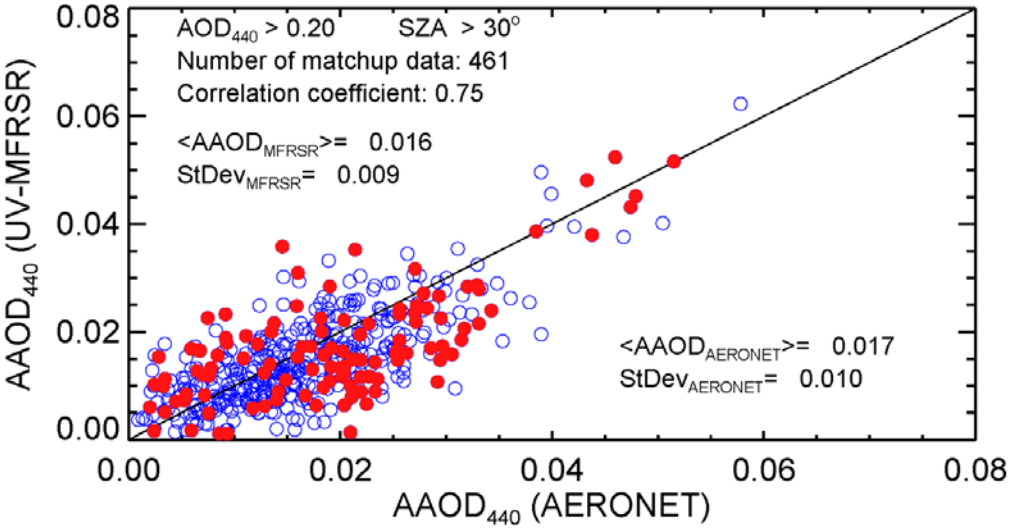

Figure 3.8. Same as Figure 3.6 for aerosol absorption optical depth (AAOD).

Figure 3.7 shows the comparison of the imaginary part of refractive index (*k*), which shows similar correlation ~0.8 as SSA comparison (Figure 3.6) and excellent agreement in mean values (~0.001). Figure 3.8 shows the comparison of the aerosol absorption optical depth (AAOD = AOD*(1-SSA)) featuring slightly reduced correlation 0.74, but excellent agreement of the mean AAOD values ~0.001.

3.5. The effect of NO_2 absorption on SSA

Unlike the MFRSR SSA retrievals, currently available AERONET version 2 inversions do not account for NO_2 absorption. This will be updated with new version (version 3) of AERONET inversions released in 2017. The AERONET version 3 will also provide error bars on SSA and *k* inversions. As shown Figure 3.9, the influence of NO_2 absorption on SSA is not significant at GSFC. The average SSA only decreases by ~0.002 neglecting NO_2 absorption. However, NO_2 absorption might have a large impact on SSA in case of low aerosol loading and high concentration of NO_2, e.g., in fall-winter seasons at GSFC [Krotkov et al., 2005c]. It will be significant factor for developing full seasonal SSA climatologies including low AOD conditions.

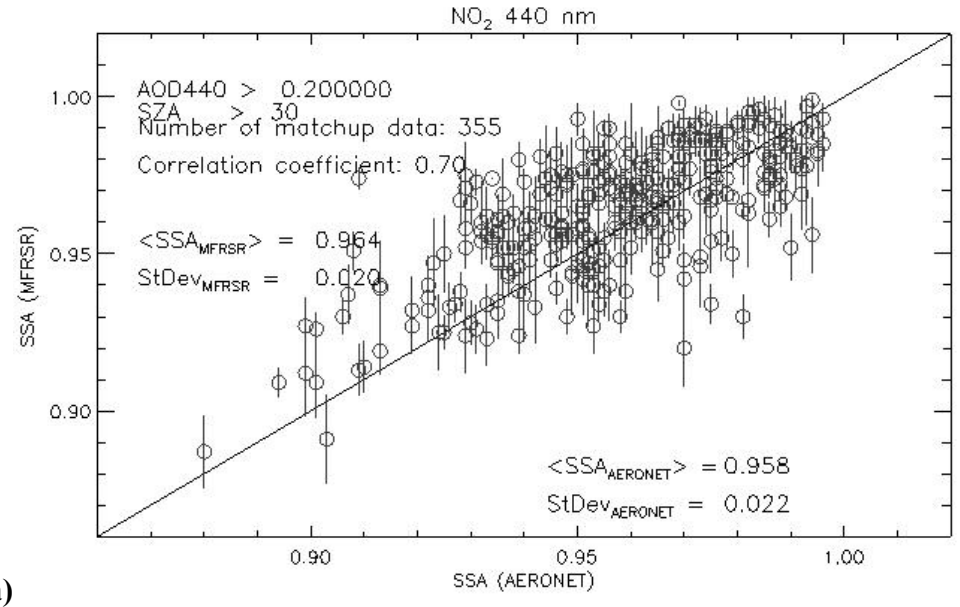

(a)

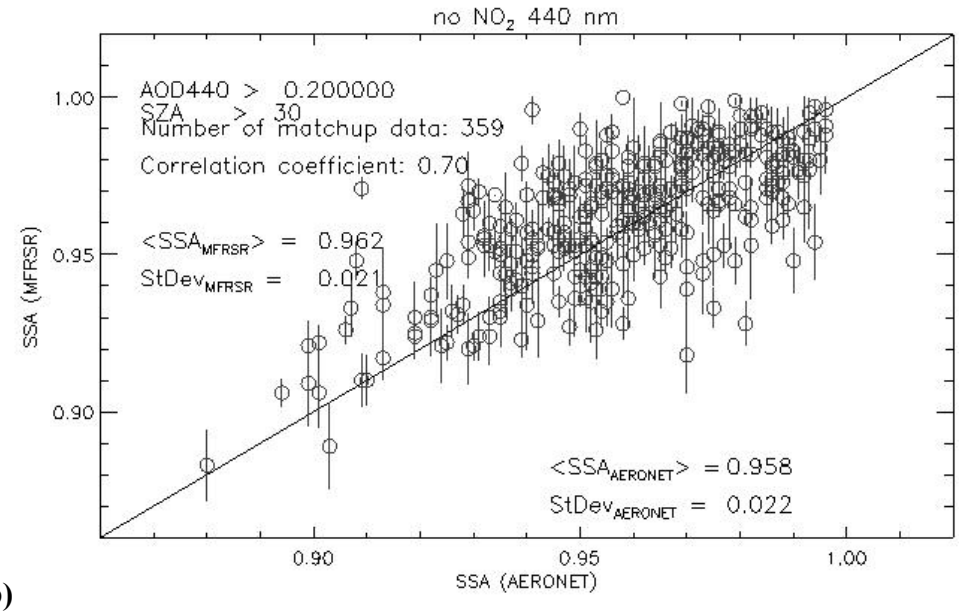

(b)

Figure 3.9. Comparison between MFRSR and AERONET SSA (a) accounting for NO_2 absorption in the MFRSR inversion and (b) without accounting for NO_2 absorption in the MFRSR inversion. Matchup retrievals performed at AERONET calibration site at Goddard Space Flight Center in Greenbelt, Maryland under cloud-free conditions from 2005 to 2012.

3.6. Long-term aerosol absorption retrievals at GSFC site

3.6.1. Time series of aerosol absorption

Figure 3.10 shows time series of daily mean SSA from AERONET almucantar and MFRSR retrievals. Most of SSAs in Figure 3.10 were measured during summers when AOD_{440} measured at GSFC frequently exceed 0.2. Derived SSAs at common wavelength 440 nm by two different techniques are generally in good agreement as already shown in Figure 3.6.

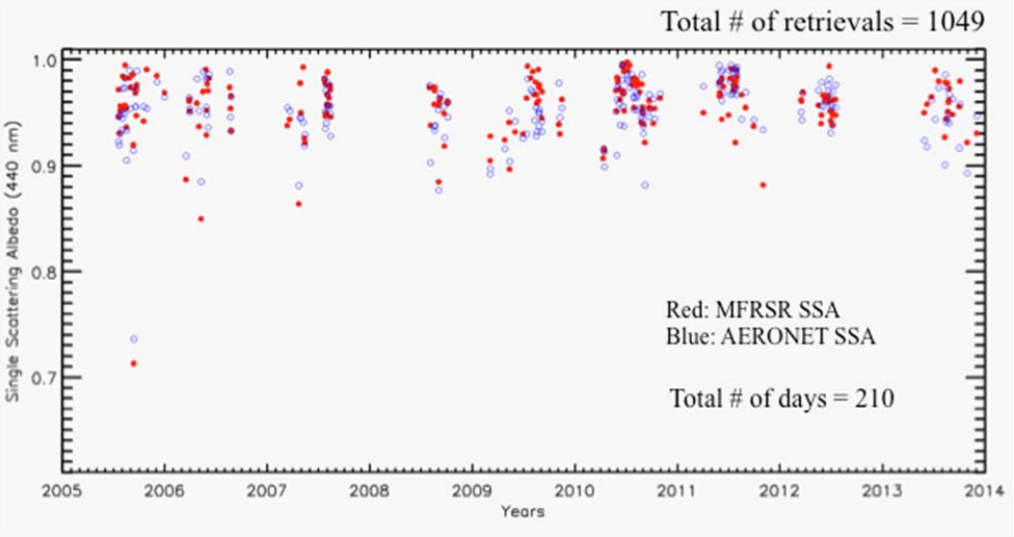

Figure 3.10. Daily mean SSA at 440 nm using relaxed filters (SZA > 30º and AOD_{440} > 0.2). (Red circles: SSA retrieved from MFRSR, blue circles: SSA from AERONET almucantar retrievals).

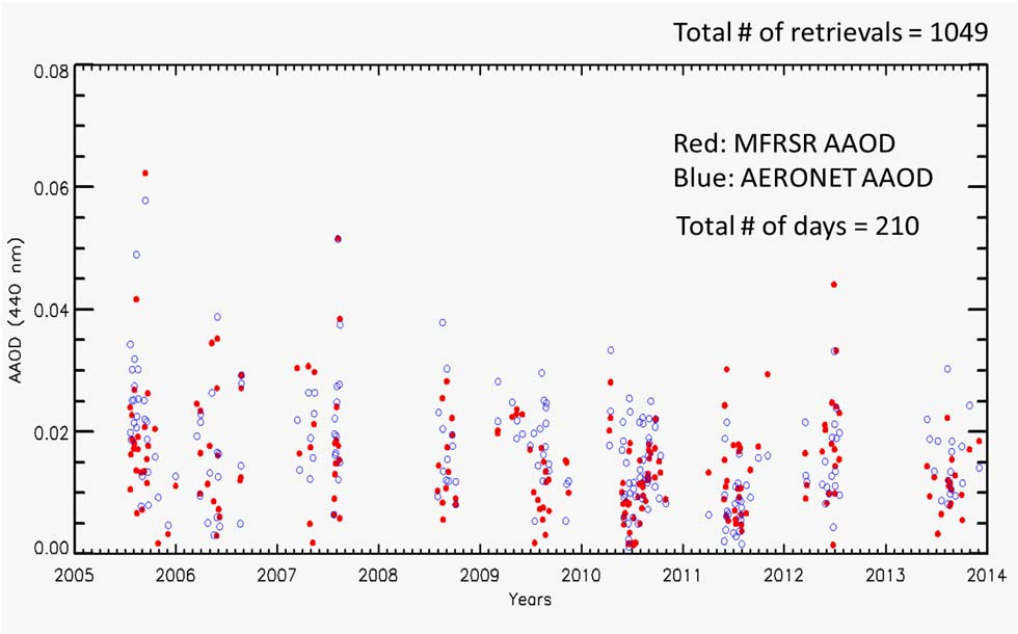

Figure 3.11. Same as Figure 3.10 for absorbing aerosol optical depth (AAOD = AOD*(1-SSA)).

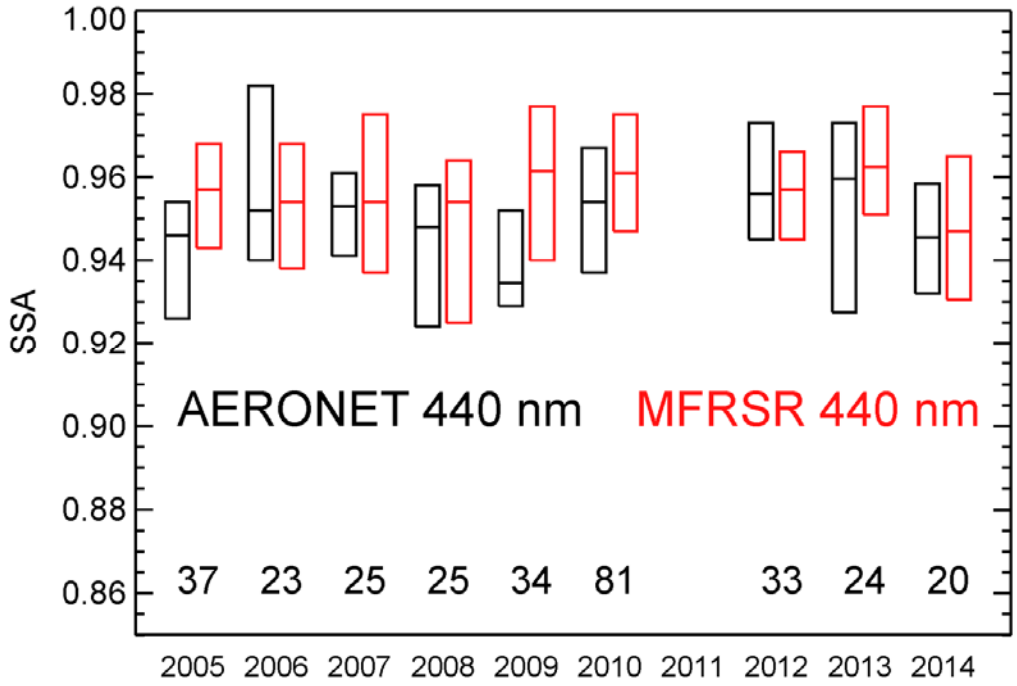

Figure 3.12. Annual time series of SSA at 440 nm retrieved from MFRSR (red) and AERONET (black). The box shows interquartile range (IQR), which defines IQR75-IQR25.

Figure 3.12 shows relatively large interannual SSA variations but suggests no significant temporal trend in the annual median values. I also found that SSA becomes smaller in the UV wavelengths and has strong wavelength dependence across blue and near-UV spectral range (Figure 3.13). The measured enhanced UV absorption suggests the presence of selectively UV absorbing aerosols (i.e., brown carbon (BrC)). Interestingly, there is a decrease of SSA in 2007 for all wavelengths except 440 nm in Figure 3.13. This demonstrates different types of aerosol showing less absorption at visible wavelength but strong absorption at UV wavelengths (i.e., selectively UV absorbing aerosols) is prevalent in 2007 compared to other years.

Figure 3.13. Time series of median SSA at 305 to 440 nm measured with the UV-MFRSR at GSFC.

3.6.2. Seasonal time series of aerosol absorption

Compared to other seasons, the highest aerosol absorption was measured in April (Figure 3.14). The principal source of this additional absorption might come from the biogenic sources especially pollen from trees. April is the peak pollen season in Maryland.

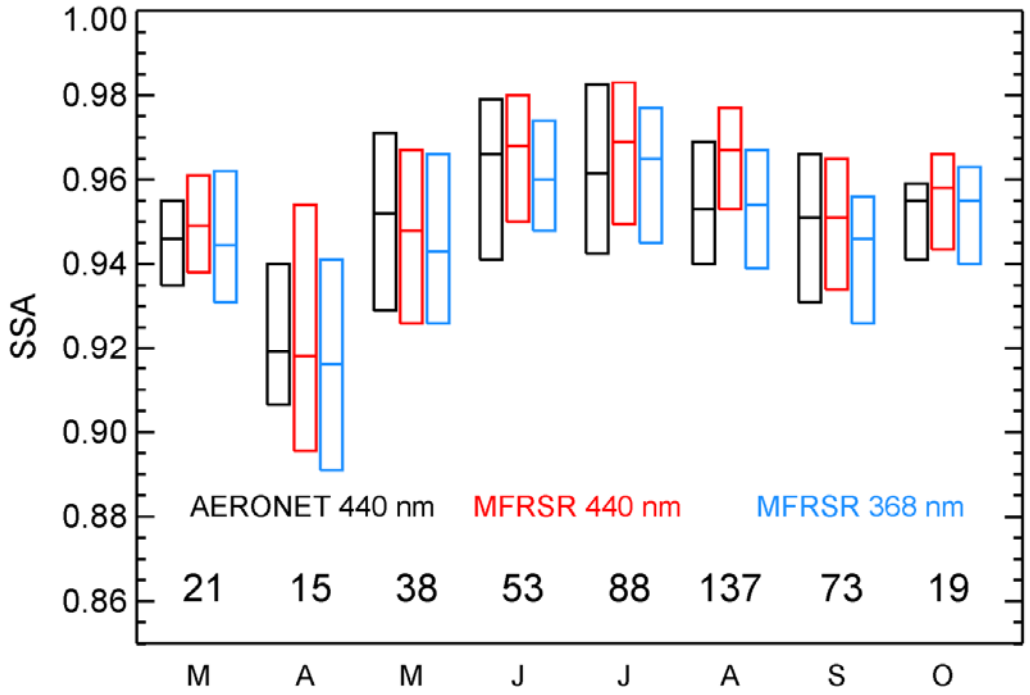

Figure 3.14. Monthly SSA at 440 and 368 nm from 10 years (2005 to 2014) of UV-MFRSR operation at NASA GSFC site. Boxes show the interquartile range (IQR; 25 to 75 percentiles) with horizontal lines showing median values.

3.6.3. Spectral dependence of aerosol absorption at GSFC site

Jethva and Torres [2011] showed that AOD retrieved in UV channels (354 and 388 nm) from satellite Ozone Monitoring Instrument (OMI) are largely dependent on the estimation of spectral dependence in *k* (Figure 3.6). They illustrate that the assumed spectral dependence of *k* is very important to retrieve AOD, SSA, and AAOD in UV wavelengths.

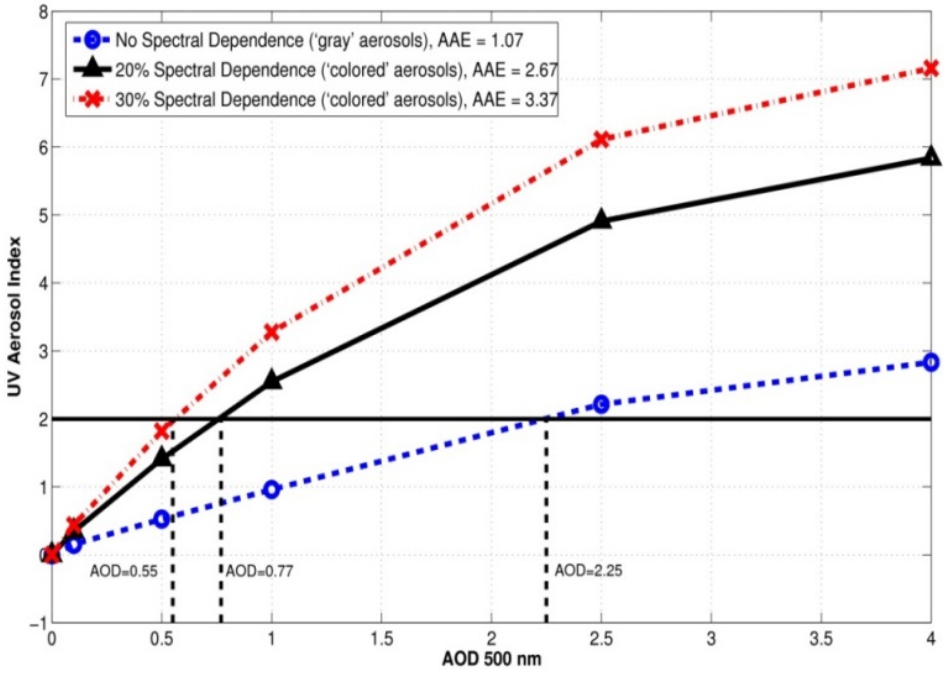

Figure 3.15. UV Aerosol Index as a function of aerosol optical depth for varying the spectral dependence of the aerosol absorption in the range 354 – 388 nm [Jethva and Torres, 2011]. Horizontal black line represents a measured value of UV-AI (=2.0) and vertical dashed lines show retrieved values of AOD (0.55, 0.77, and 2.25) assuming different assumed values of *k* spectral dependence.

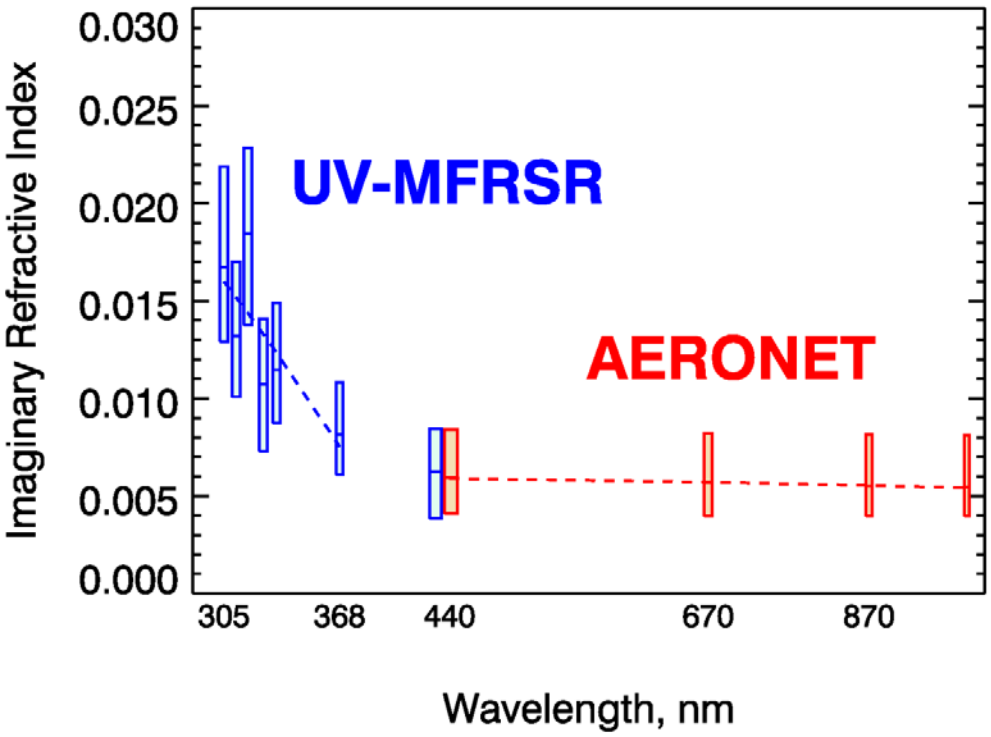
Imaginary Refractive Index
0.030
0.025
0.020
0.015
0.010
0.005
0.000
UV-MFRSR
AERONET
305
368
440
670
870
Wavelength, nm

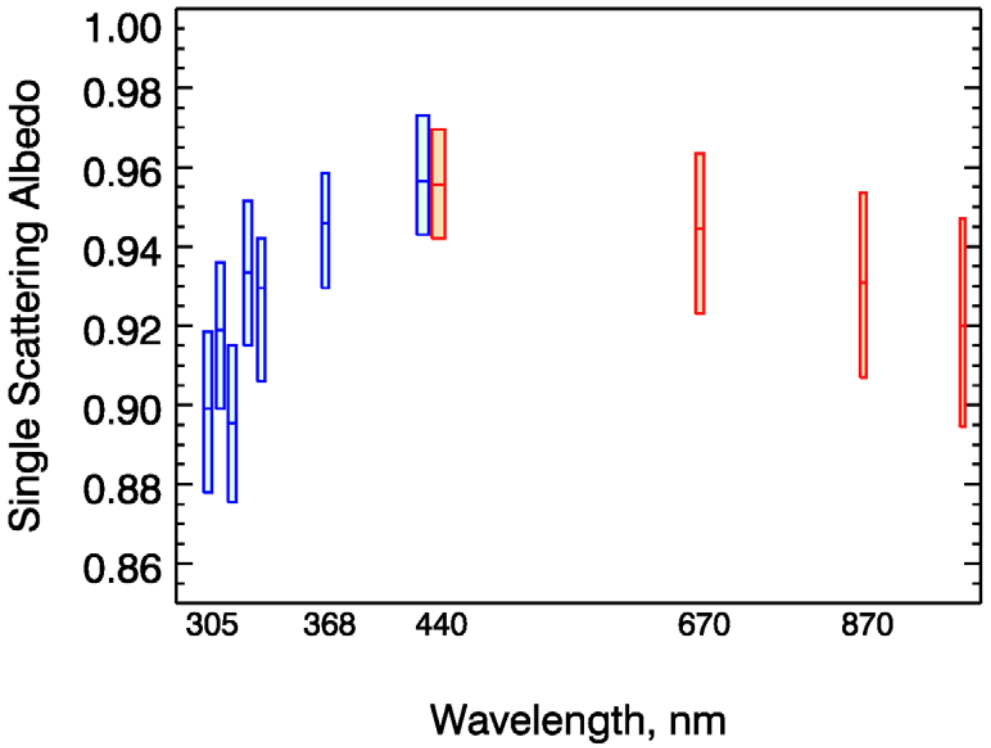
Single Scattering Albedo
1.00
0.98
0.96
0.94
0.92
0.90
0.88
0.86
305
368
440
670
870
Wavelength, nm

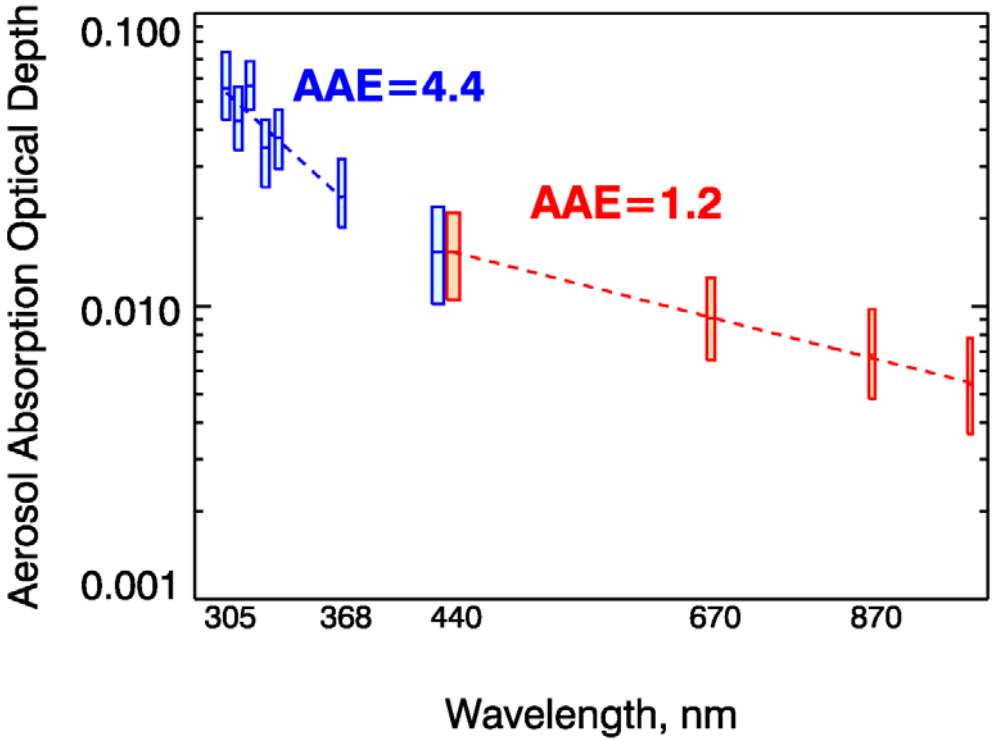

Figure 3.16. Spectral dependence of (a) the column effective imaginary refractive index (*k*), (b) SSA, and (c) AAOD at GSFC site. The box is the same as described in Figure 3.14.

3.7. Summary and Conclusion

In this chapter, relaxing AERONET Level 2 filters are suggested to accept retrievals with $AOD_{440} > 0.2$ and SZA > 30º. Therefore, the number of matchup retrievals is increased significantly by a factor of 4. The range in SSA values doubles from 0.07 to 0.15, meaning that the minimum SSA value decreased from 0.93 to 0.85. As a result, the SSA_{440} correlation coefficient improves from 0.6 to

~0.8. The average SSA_{440} decreases by 0.01 to 0.957 for MFRSR and 0.952 for AERONET. The latter value is within 0.02 uncertainty range for AERONET climatological value of 0.96 ± 0.02 [Giles et al., 2012].

Chapter 4: Impacts of brown carbon from biomass burning on surface UV and ozone photochemistry in the Amazon Basin

4.1. Introduction

Biomass burning emits large amounts of black carbon (BC) and organic carbon (OC) particles into the atmosphere. This has profound effects on Earth's radiation budget and on atmospheric photochemistry. Most current aerosol models treat all OC from biomass burning as purely scattering, thus underestimating heating effect of the total carbon (OC + BC), the primary absorbing component of carbonaceous aerosols [Myhre et al., 2013]. However, recent studies [Kirchstetter et al., 2004; Chen and Bond, 2010; Lack et al., 2012; Saleh et al., 2013; 2014] suggest that the light absorbing component of OC known as "brown carbon" (BrC) is capable of enhancing total absorption efficiency of OC, altering direct radiative forcing (DRF) at the top of the atmosphere from negative to positive [Feng et al., 2013; Saleh et al., 2014]. Our 'assumed BrC' is defined by the retrieved total absorption minus the retrieved absorption by the BC component. Measuring BrC absorption is also essential due to its effect on photolysis rates [Dickerson et al., 1997; He and Carmichael, 1999] and solar UV radiation reaching the surface [Krotkov et al., 1998; 2005; Arola et al., 2009] with important implications for plant growth [Teramura and Sullivan, 1994; Rousseaux et al., 1999] and human health [Lautenschlager et al., 2007].

Field measurements of light absorption by aerosols (defined as column

effective imaginary part of the complex refractive index, *k*) in the visible and near-infrared (NIR) wavelengths (440, 670, 870, and 1020 nm) are available from ~400 global locations of the Aerosol Robotic Network (AERONET) [Holben et al., 1998; Dubovik et al., 2002]. Schuster et al. [2005] used those measurements to infer the column-averaged mass density and mass absorption efficiency (MAE) of BC at selected AERONET sites. Arola et al. [2011] advanced the method of Schuster et al. [2005] to infer both BC and BrC volume fractions from the AERONET inversions that show enhanced values of *k* at 440 nm relative to the red and NIR wavelengths. The spectral dependence of BrC absorption can vary strongly depending on the type of aerosol emissions (fossil fuel combustion versus biomass burning), as well as physical-chemical transformation (primary versus secondary organic aerosols) [Saleh et al., 2014; Lu et al., 2015]. As a result, the 440-nm wavelength does not have enough sensitivity to properly detect some types of BrC. I combine AERONET almucantar inversions in the visible–NIR wavelengths with diffuse and direct surface irradiance measurements from UV Multifilter Rotating Shadowband Radiometer (UV-MFRSR) [Krotkov et al., 2005a; 2005b] to estimate the BrC column mass density; this is not possible from standalone AERONET inversions. Previous measurements of column aerosol absorption in UV wavelengths have been conducted in urban/suburban locations [Krotkov et al., 2005a; Krotkov et al., 2009; Buchard et al., 2011]. This study presents the first measurements of the spectral dependence of *k* for smoke down to the biologically active, UV-B wavelengths (~ 305 nm) to estimate the MAE of BrC, the BrC/BC column mass density ratio, and effects on tropospheric ozone

photochemistry.

To measure UV absorption by smoke, we conducted a field campaign in Santa Cruz, Bolivia in September 2007, the month of peak carbonaceous aerosol production in South America from agricultural biomass burning in the Amazon Basin [Eck et al., 1999; Torres et al., 2010], using UV-MFRSR irradiance measurements. The total (scattering and absorption) aerosol optical depth measured by AERONET at 440 nm ranged from 0.74 to 2.27. Satellite measurements of UV aerosol absorption optical depth (AAOD) from Ozone Monitoring Instrument (OMI) on board NASA's Earth Observing System Aura satellite [Torres et al., 2007; Jethva et al., 2014] clearly show elevated AAOD values over Santa Cruz in September 2007 (Figure 4.1). The flow of smoke was blocked by the Andes Mountains (Figure 4.2), so smoke accumulated over the area to the east of the mountain range. This increased the fraction of aged brown secondary organic aerosol, with less absorption at visible wavelengths but stronger absorption in the UV [Saleh et al., 2013; Laskin et al., 2015]. Biomass burning in the tropics also produces elevated levels of tropospheric ozone, a secondary pollutant resulting from photochemical reactions involving nitrogen oxides ($NO_x = NO + NO_2$) and volatile organic compounds (VOC) in the presence of sunlight [Dickerson, 1984; Pickering et al., 1991]. Tropospheric ozone negatively affects agricultural crops, the human respiratory system, and is the main culprit responsible for photochemical smog.

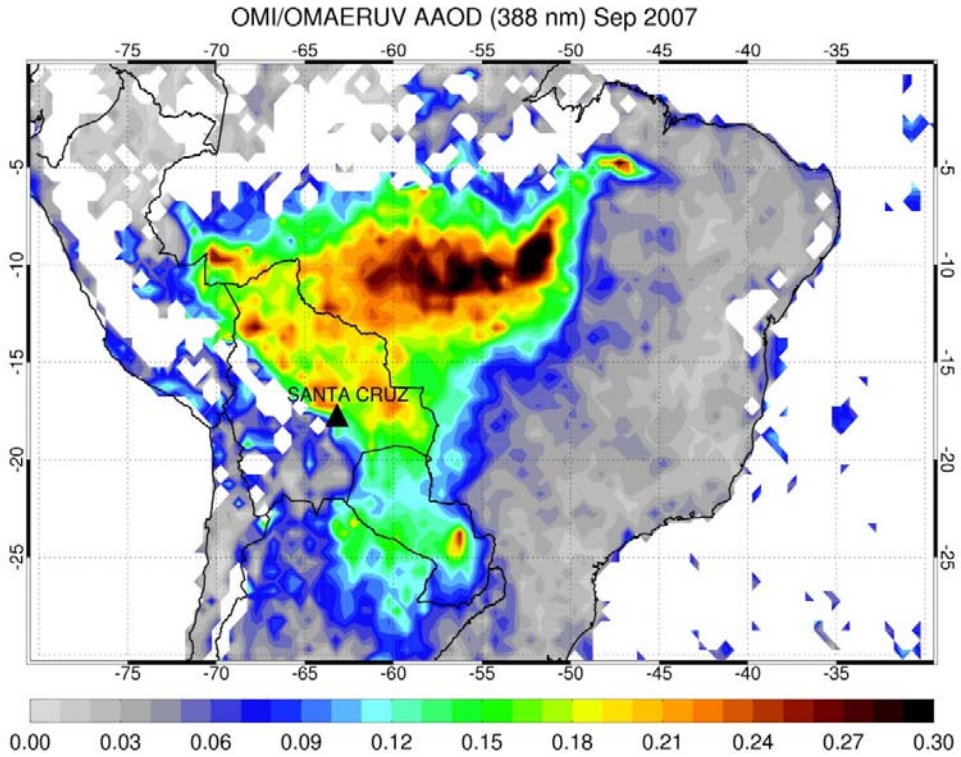

Figure 4.1. Distribution of biomass burning and resultant smoke over South America. Satellite map of monthly mean aerosol absorption optical depth (AAOD) at 388 nm from Ozone Monitoring Instrument (OMI) on board NASA Aura satellite for September 2007. A solid black triangle shows the location of Santa Cruz.

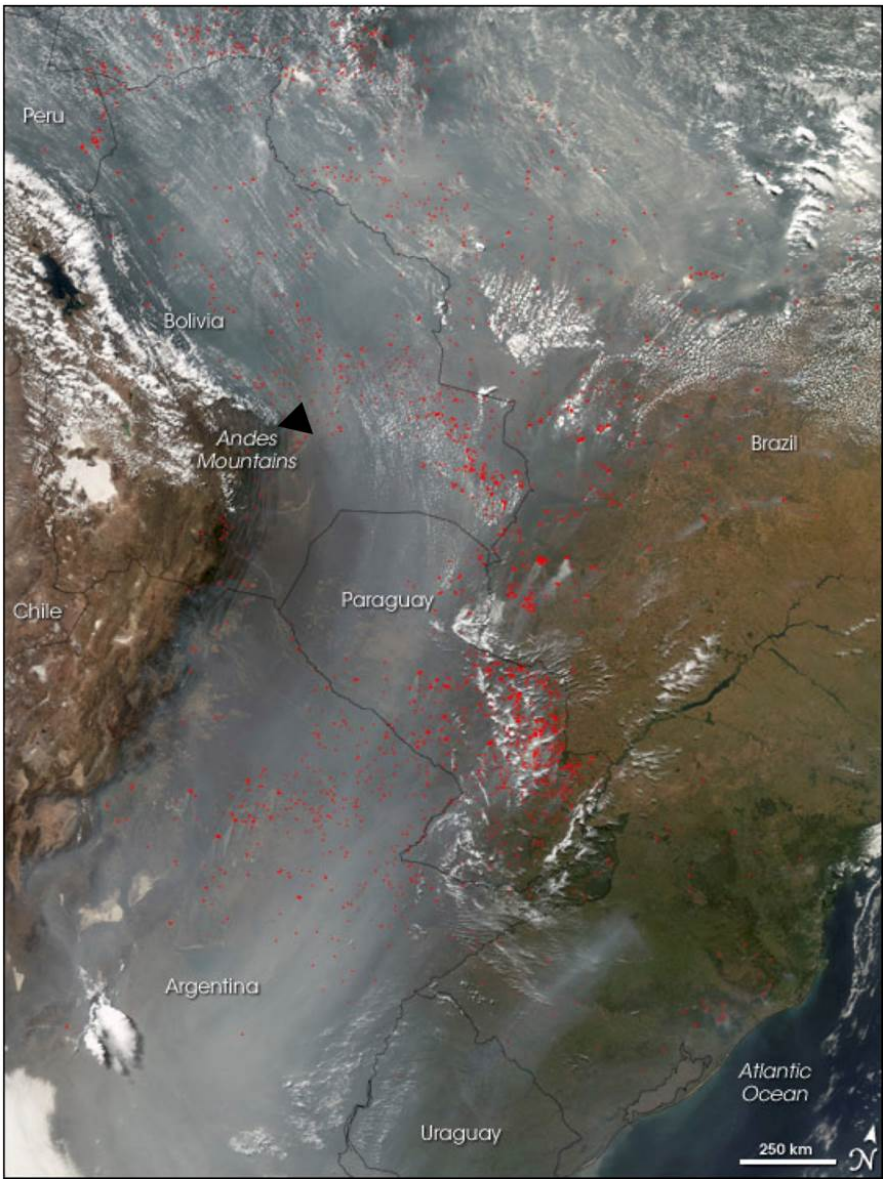

Figure 4.2. MODIS (Moderate Resolution Imaging Spectroradiometer) true color image on 9 September 2007 over the same region showing active fire locations (marked in red) and a thick blanket of smoke stretching from the Amazon to Argentina. The background image was obtained from NASA's Earth Observatory website (http://earthobservatory.nasa.gov/IOTD/view.php?id= 8033&eocn= image&eoci= related_image). A solid black triangle shows the location of Santa Cruz.

4.2. Data and Methodology

Our field measurements of BrC and BC aerosol absorption are based on retrievals of total column effective imaginary refractive index (k_{ret}) from AERONET inversions at visible and NIR wavelengths [Dubovik et al., 2002] and diffuse/direct irradiance inversions at UV wavelengths [Krotkov et al., 2005b]. First, I derive the BC volume fraction (f_{BC}) from AERONET k_{ret} at visible and NIR wavelengths from 670 to 1020 nm [Schuster et al., 2005]. Next, I calculate the BrC volume fraction (f_{BrC}) assuming (1) flat spectral dependence of k_{BC}, (2) known value of k_{BrC} at 368 nm from laboratory absorption measurements or smoke chamber experiments as shown in Figure 4.3. Finally, I use the inferred f_{BC} and f_{BrC} to calculate k_{BrC} at short UV-B wavelengths by fitting k_{ret} at 305, 311, 317, 325, and 332 nm using MG mixing rule. The details are given below.

4.2.1. BrC volume fraction calculation

Here the strategy of BrC retrievals combining AERONET and UV-MFRSR inversions at UV and visible wavelengths is demonstrated. At step 1, the BC volume fraction is obtained from AERONET retrieved k values at red and NIR wavelengths (670, 870, and 1020 nm) following the method of Schuster et al. [2005]. At step 2, Arola et al. [2011] method is applied to calculate the BrC column volume fraction using UV-MFRSR retrievals of k at 368 nm ($k_{ret\text{-}368}$)

instead of 440 nm. The method assumes a mixture of BC and BrC components embedded in non-absorbing host and applies the Maxwell-Garnett (MG) mixing rule to calculate the effective imaginary refractive index (k_{calc}), which depends on the volume fractions of BC (f_{BC}) and BrC (f_{BrC}) and their known a priori complex refractive indices (k_{BC} and k_{BrC}). I calculate f_{BrC} by fitting $k_{calc}(f_{BrC}, f_{BC}, k_{BrC}, k_{BC})$ to $k_{ret\text{-}368}$ assuming lower and upper limits of $k_{BrC\text{-}368}$ (Figure 4.3) and known fixed BC volume fraction (f_{BC} =0.019) from step 1. Compared to shorter UV-MFRSR UV channels, the 368-nm channel has the advantage of large signal-to-noise (S/N), negligible gaseous absorption, and moderate Rayleigh optical thickness ~ 0.5 thus reducing uncertainties in UV-MFRSR *k* inversions.

The retrieval requires a priori knowledge of the BrC complex refractive index. The real part of refractive index, n_{BrC}, is fixed similar to Arola et al. [2011]. The possible range of the imaginary part, k_{BrC} is determined from prior chamber and laboratory measurements for absorbing organic aerosols from biomass burning sources (Figure 4.3).

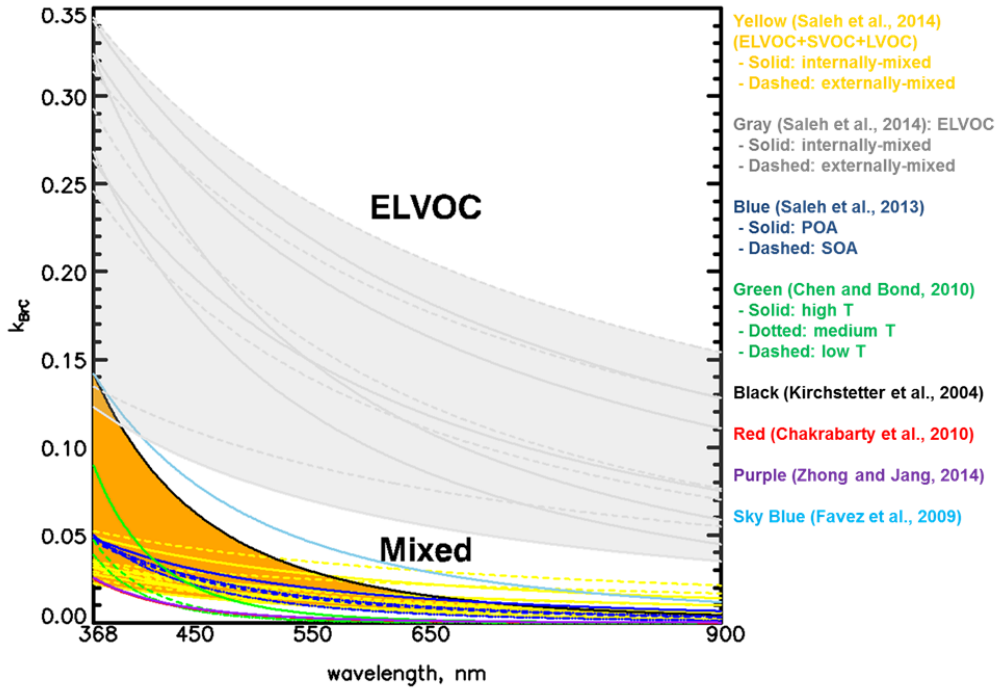

Figure 4.3. Summary of studies of brown carbon imaginary refractive indices for biomass burning. k_{BrC} from previous literature studies are parameterized by equation (1). POA and SOA correspond to primary organic aerosol and secondary organic aerosol, respectively. The topmost value of k_{BrC} at 368 nm ($k_{BrC\text{-}368}$ ~ 0.34) are found from smoke chamber experiments [Saleh et al., 2014] shown as gray shade. However, this highest value is not used because it is obtained by heating the aerosol to 250 °C to measure only highly absorptive extremely low-volatility organic compounds (ELVOC). Under typical conditions, ELVOCs are usually mixed with other OA components (semi-volatile organic compounds (SVOC) and low-volatile organic compounds (LVOC)). Excluding ELVOC, I use the highest $k_{BrC\text{-}368}$ (~0.14) in the mixed condition that Kirchstetter et al. [2004] measured acetone soluble BrC extracted from African savanna biomass burning smoke samples. The lowest value of $k_{BrC\text{-}368}$ in the mixed condition is 0.025 measured by Saleh et al. [2014]. The used range of $k_{BrC\text{-}368}$ is shown as orange shade.

Prior k_{BrC} measurements shown in Figure 4.3 are interpolated to the 368 nm wavelength ($k_{BrC\text{-}368}$) using least squares fitting to the power law spectral dependence (4.1):

$$k_{BrC}(\lambda) = k_{BrC\text{-}550}\left[\frac{550}{\lambda}\right]^{w} \quad (4.1)$$

where k_{BrC} is the BrC imaginary refractive index and $k_{BrC\text{-}550}$ is the measured BrC imaginary refractive index at reference wavelength (550 nm) [Kirchstetter et al., 2004; Saleh et al., 2014].

This range of $k_{BrC\text{-}368}$ from 0.025 to 0.14 together with the specific MG mixing rule assumption determines the possible range of calculated f_{BrC} and BrC/BC fraction ratio that are consistent with our retrievals of k: the larger the assumed value of $k_{BrC\text{-}368}$, the smaller the inferred value of f_{BrC}. The upper limit on f_{BrC} = 0.27 is obtained by using the smallest reported a priori value of $k_{BrC\text{-}368}$ ~ 0.025 from Saleh et al. [2014]. The lower limit value of f_{BrC} = 0.05 is acquired by the upper limit of $k_{BrC\text{-}368}$ ~ 0.14 from Kirchstetter et al. [2004].

4.2.2. BrC column mass density calculation

In order to derive column mass density for BC and BrC, their calculated volume fractions (f_{BC} and f_{BrC}) are multiplied by the AERONET-inferred total volume column density integrated over particle size distribution, and the assumed mass density:

$$[BC]=f_{BC}\cdot\rho_{BC}\cdot\int\frac{dV}{dlnr}dlnr \tag{4.2}$$

$$[BrC]=f_{BrC}\cdot\rho_{BrC}\cdot\int\frac{dV}{dlnr}dlnr \tag{4.3}$$

where ρ_{BC} is BC mass density, ρ_{BrC} is BrC mass density, $\frac{dV}{dlnr}$ is the particle volume distribution (cf. equation (6) in Schuster et al. [2005] for BC and equation (2) in Arola et al. [2011] for BrC). The BrC mass density is assumed as 1.2 gm^{-3} [Turpin and Lim, 2001]. Thus, lower and upper limits of the BrC column mass density are 10.9 and 61.2 mg/m^2, while the average BC column mass density is 6.5 mg/m^2 assuming a BC mass density equal to 1.8 gm^{-3} [Bond and Bergstrom, 2006]. Details are shown in Table 4.1.

Table 4.1. The calculated BrC volume fraction (f_{BrC}) and column mass density. The estimated ranges are the uncertainty bound.

Used k_{BrC} at 368 nm ($k_{BrC-368}$)	Kirchstetter et al. [2004]	Saleh et al. [2014]
BrC volume fraction	0.048	0.270
BrC column mass density ([BrC], mg/m^2)	10.89	61.24
[BrC]/[BC]	1.68	9.47

f_{BC} = 0.019 calculated from AERONET wavelengths (670, 870, and 1020 nm)

BC column mass density ([BC]) = 6.46 [mg/m^2]

4.2.3. BrC spectral absorption calculation in UV

I derive k_{BrC} at UV wavelengths of 332, 325, 317, 311, and 305 nm by fitting UV-MFRSR retrieved k_{ret} assuming a fixed value of f_{BrC} = 0.05 (0.27) inferred from $k_{ret-368}$ and known f_{BC} = 0.019 calculated from step 1 at Section 4.2.1. In other words, I modified the algorithm to infer k_{BrC} by fitting retrieved k_{ret} and k_{calc} at short UV wavelengths using fixed values of f_{BC} and f_{BrC} calculated in previous steps 1 and 2 of Section 4.2.1. Finally, derived k_{BrC} at several UV-B and UV-A wavelengths is fitted to the power law equation (4.4) similarly to equation (4.1).

$$k_{\mathrm{BrC}}(\lambda) = k_{\mathrm{BrC\text{-}368}} \left[\frac{368}{\lambda}\right]^{w_{\mathrm{MFRSR}}} \quad (4.4)$$

4.2.4. OMI retrievals of carbonaceous aerosols

The Ozone Monitoring Instrument (OMI) flown onboard the EOS-Aura satellite as part of the A-train satellite constellation measures sun backscattered radiance from the Earth's atmosphere and surface in the UV and visible region (270 – 500 nm) on a global scale and on daily basis [Levelt et al., 2006; Torres et al., 2007]. With a cross-track swath of about 2600 km, OMI scans the entire Earth in 14 to 15 orbits per day with a nadir ground pixel spatial resolution of 13 × 24 km^2. The primary objective of OMI is to measure concentrations of trace gases such as ozone, sulfur dioxide, and nitrogen dioxide along with the optical properties of tropospheric aerosols. OMI observations in the near-UV region at 354 nm and 388 nm are used to derive UV Aerosol Index (UV-AI) which is a well-accepted indicator for detecting and tracing the absorbing aerosols such as carbonaceous aerosols and dust [Torres et al., 1998; 2002; 2005] and to retrieve AOD and SSA at 388 nm (OMAERUV product) [Torres et al., 2007; 2013]. The most recent operational algorithmic upgrades are documented in Jethva and Torres [2011] and Torres et al. [2013] that include three major modifications: (1) improved representation of organic aerosols in the biomass burning smoke aerosols, (2) use of aerosol height climatology derived from Cloud-Aerosol Lidar

with Orthogonal Polarization (CALIOP) lidar-based measurements of the vertical profiles in conjunction with OMI UV-AI, and (3) robust identification of aerosol types by taking advantage of concurrent observations of carbon monoxide (CO) measured by the Atmospheric Infrared Sounder (AIRS). The upgraded OMAERUV aerosol product has been validated globally using ground-based measurements of AOD [Ahn et al., 2014] and SSA [Jethva et al., 2014] inversions at 440 nm by the AERONET global network of ground sun-sky photometers. The comparisons of OMI-retrieved SSA against equivalent inversions made by AERONET revealed a good level of agreement between the two fundamentally different techniques in which most matchup data points are found to fall within their expected retrieval uncertainties (± 0.03) for SSA at 440 nm [Jethva et al., 2014]. In the present study, the latest research version 1.7.3.1 of the OMAERUV aerosol product is used. This product includes major upgrades already documented in Jethva and Torres [2011] and Torres et al. [2013] plus a few more improvements that are mostly related to the assignments of retrieval quality flags.

4.2.5. Photolysis rate

Actinic fluxes in the atmosphere are computed in the 290 – 425 nm spectral range using the Discrete Ordinates Radiative Transfer Model (DISORT) [Stamnes et al., 1988] for a Multi-Layered Plane-Parallel Medium with the 16-stream setup. Chemical composition of the atmosphere is prescribed according to

the monthly climatology derived from the Global Modeling Initiative (GMI) model output. The GMI 3-D chemistry and transport model is integrated with meteorological fields from the Modern Era Retrospective-analysis for Research and Applications (MERRA) and includes full chemistry for both the troposphere and the stratosphere [Douglass et al., 1999; Strahan et al., 2011]. Gas absorption and scattering optical depths are computed using components from the Line-By-Line Radiative Transfer Model [Clough et al., 1992; 2005]. The aerosol optical properties (extinction, single scattering albedo, and phase function) are calculated for a given size distribution assuming the sphericity of particles using analytic Mie solution [Veihelmann et al., 2006]. Lower boundary conditions assume a Lambertian reflection with the ultraviolet surface albedo of 0.04. Photolysis rate calculations are based on the absorption cross section and quantum yield data [Sander et al., 2011].

Table 4.2. Summary of explicit input aerosol parameters for radiative transfer model and chemical model simulation (See Figure 4.5).

Wave length (nm)	305	311	317	325	332	368	440	670	870	1020
Model 1: k (BC only)	0.0126	0.0126	0.0126	0.0126	0.0126	0.0126	0.0126	0.0126	0.0126	0.0126
Model 2: k (BrC+ BC)	0.0342	0.0271	0.0296	0.0209	0.0245	0.0192	0.0144	0.0125	0.0136	0.0122

median of real part of the refractive index at 440 nm from AERONET: 1.4905

median of surface albedo at 440 nm from AERONET: 0.04085

median of volume concentration for fine mode from AERONET: 0.1525

median of volume concentration for coarse mode from AERONET: 0.0365

median of (standard deviation from) volume median radius for fine mode from AERONET: 0.1810 (0.4320)

median of (standard deviation from) volume median radius for coarse mode from AERONET: 3.7410 (0.6585)

4.2.6. Box model

The box model is based on the Regional Atmospheric Chemical Mechanism Version 2 (RACM2) [Goliff et al., 2013] and is run on the FACSIMILE platform for Windows software (MCPA Software, Ltd). RACM2 is well known and has been used in research and regulatory applications. The

RACM2 mechanism with the chemical kinetic data replaced with the most recently evaluated set of chemical kinetic data [Atkinson et al., 2008; Sander et al., 2011] was used in this study.

RACM2 is a revised version of Regional Atmospheric Chemical Mechanism Version 1 (RACM) [Stockwell et al., 1997]. It is intended to be valid for conditions ranging from pristine to polluted and from the Earth's surface through the upper troposphere. The main revisions have been performed for organic chemistry such as the oxidation mechanisms for isoprene, α-pinene, and d-limonene. Most of the organic species are aggregated into the model species based on their similarity in functional groups and reactivity toward OH. For instance, alkenes other than ethene are represented by three species: terminal alkenes, internal alkenes, and dienes. Some organic species such as formaldehyde and isoprene are treated explicitly.

The box model was initialized with a NO_x (= NO + NO_2) concentration of 100 ppbv and a VOC concentration of 200 ppbv. To represent the smoke plume in this work, the mean NO to NO_2 ratio, VOC speciation, mean concentrations of long-lived species like CO and CH_4, as well as mean temperature, pressure and humidity in the Canadian wildfire plumes observed during the Arctic Research of the Composition of the Troposphere from Aircraft and Satellites (ARCTAS) in 2008 (espo.nasa.gov/arctas). The photolysis reaction coefficients, or photolysis frequencies, used in the model were calculated by radiative transfer model using DISORT with 16 streams (details shown in Section 4.2.5). The box model was run for 20 days and the output calculated OH, HO_2, and other reactive intermediates.

The net instantaneous O_3 production rate, $P(O_3)$, can be written approximately as the following equation:

$$P(O_3) = k_{HO_2+NO}[HO_2][NO] + \sum k_{RO_{2i}+NO}[RO_{2i}][NO] - k_{HO_2+O_3}[HO_2][O_3] - k_{OH+O_3}[OH][O_3] - k_{O(^1D)+H_2O}[O(^1D)][H_2O] \quad (4.5)$$

where k terms are the reaction rate coefficients and RO_{2i} is the individual organic peroxy radicals. The negative terms correspond to the reaction the reactions of OH and HO_2 with O_3 and the photolysis of O_3 followed by the reaction of $O(^1D)$ with H_2O.

4.3. Retrieval and evaluation of spectral dependence of smoke absorption

Figure 4.4(a) shows joint UV-MFRSR and AERONET retrievals of spectral *k*. Our assumptions about mixing state, size distribution, and sphericity are fully consistent with the standard AERONET inversions [Dubovik et al., 2002; Schuster et al., 2016]. I only use sphericity retrievals by AERONET exceeding 95% to justify the sphericity assumption. Both retrievals agree at 440 nm. The flat spectral dependence of *k* in the visible–NIR region is consistent with a "BC only absorption" assumption [Schuster et al., 2005; Moosmuller et al., 2011]. However,

this hypothesis (see the extrapolated red line in Figure 4.4(a)) is grossly inconsistent with the observed enhanced values of k in the UV. This study postulates that the enhanced k values in the UV are a manifestation of the presence of a selectively UV absorbing BrC component of the aged carbonaceous aerosols from tropical forest burning [Saleh et al., 2013; Wang et al., 2014].

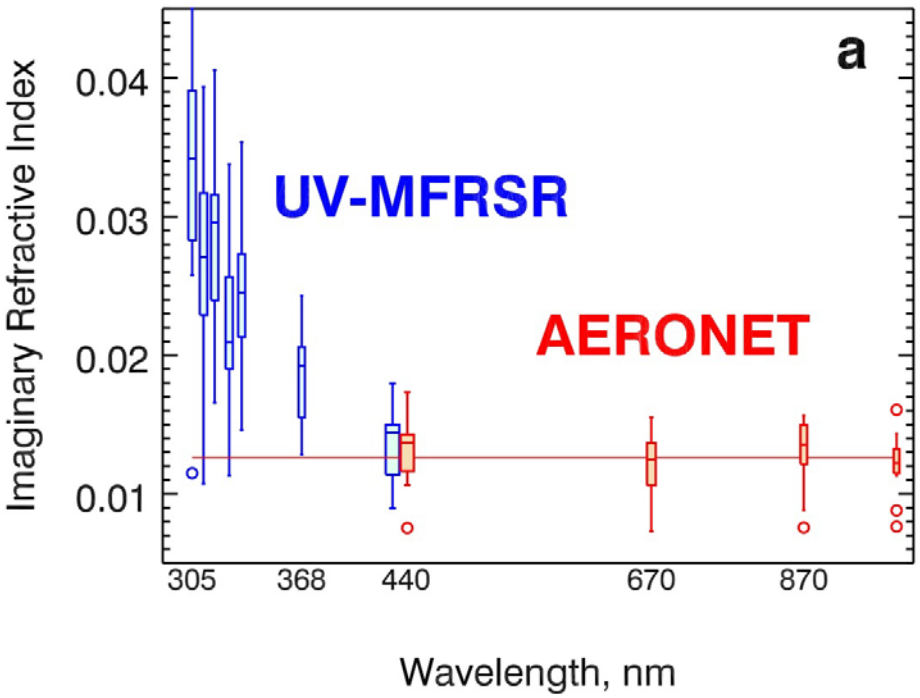
a
UV-MFRSR
AERONET
Imaginary Refractive Index
0.04
0.03
0.02
0.01
305
368
440
670
870
Wavelength, nm

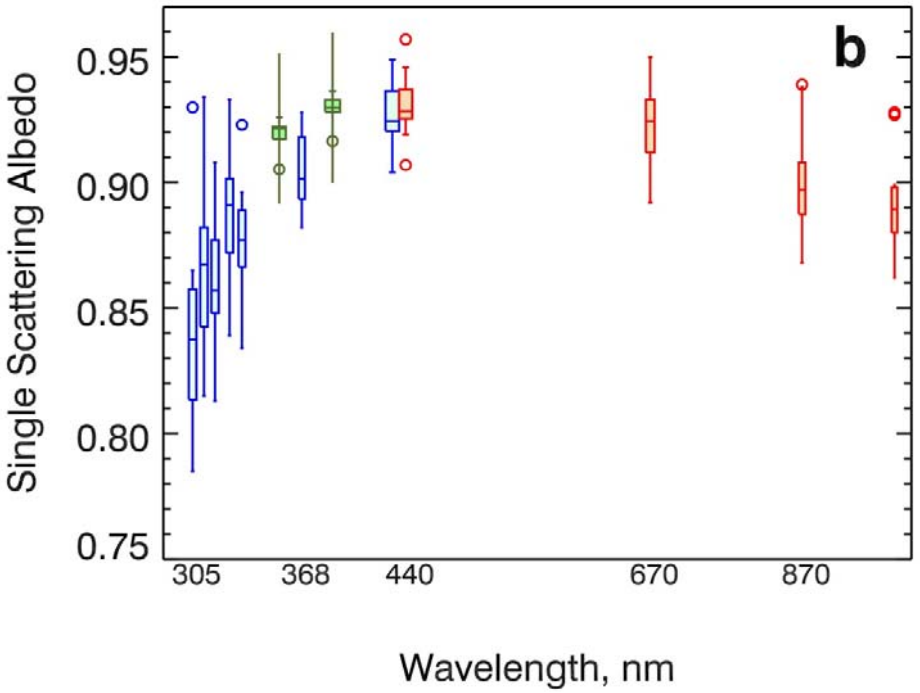
b
Single Scattering Albedo
0.95
0.90
0.85
0.80
0.75
305
368
440
670
870
Wavelength, nm

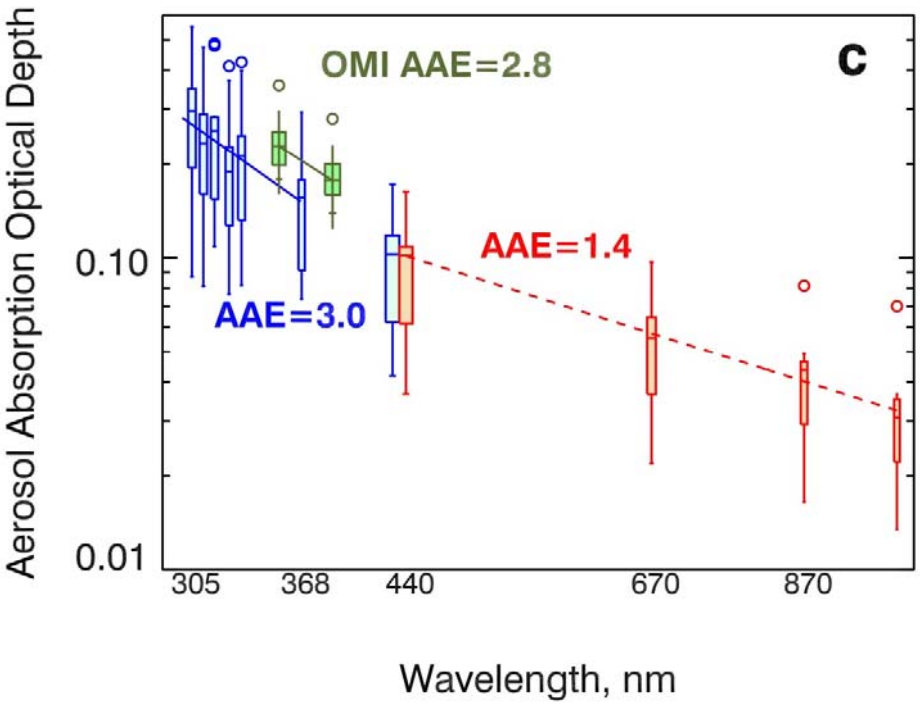

Figure 4.4. Spectral dependence of smoke aerosol absorption parameters derived from ground-based and satellite (OMI) retrievals during the field campaign in Santa Cruz, Bolivia in September-October 2007. (a) Imaginary part of the column effective refractive index (*k*), (b) Single scattering albedo (SSA), and (c) Aerosol absorption optical depth (AAOD = AOD*(1-SSA)). Retrievals are from UV-MFRSR (blue symbols), Vis–NIR AERONET (red symbols), and satellite OMI UV (green symbols). All retrievals are shown as box-whisker plots. Boxes are the interquartile range (IQR; 25 to 75 percentiles) and whiskers are stretched to the maximum and minimum within 1.5 times the IQR. The circles show the outliers. The solid red line in (a) shows the theoretically calculated campaign–average *k* assuming that BC is the only absorbing component. The error bars in (b) and (c) for OMI-retrieved SSA and AAOD (± 0.03 for SSA and ± 30% for AAOD) are shown as thin vertical lines exceed the whisker's range.

To compare with OMI retrievals at 354 nm and 388 nm, the UV-MFRSR-retrieved *k* is converted into single scattering albedo (SSA) assuming AERONET inferred aerosol size distribution and spherical aerosol shape (AERONET

spherical particles fraction > 95%) (Figure 4.4(b)). The average UV-MFRSR SSA at 388 nm (linearly interpolated from retrievals at 368 nm and 440 nm) is slightly smaller than the OMI values, but within the 0.03 error typically assumed in OMI retrievals [Jethva et al., 2014]. Figure 4.4(c) shows derived spectral dependence of AAOD, which describes the total column smoke absorption optical depth due to both BC and BrC. The UV-MFRSR AAOD values agree well with AERONET AAOD at 440 nm and are within the ± 30% error bar of the OMI-retrieved AAOD at UV-A wavelengths (Figure 4.4(c)).

Similarly to the Angstrom Exponent (AE), which characterizes the spectral dependence of AOD parameterized by power law, the absorption Angstrom Exponent (AAE) characterizes the spectral dependence of AAOD=AOD*(1-SSA). For smoke aerosols, there is no single power law parameterization describing AAOD spectral dependence from UV to the NIR wavelengths. This results in spectrally dependent values of AAE. The UV-MFRSR derived AAE in UV wavelengths (~3.0 in the range 305 – 368 nm) agrees well with the OMI assumed AAE (~2.8 between 354 nm and 388 nm) [Jethva and Torres, 2011] which is based on Kirchstetter et al. [2004] observations. This derived AAE in UV is significantly larger than the AAE in the visible–NIR wavelengths (AAE ~ 1.1 ± 0.3 for BC only absorption) [Lack and Langridge, 2013]. This confirms the general assumption that smoke absorption in the visible-NIR wavelengths is dominated by BC component, while in the UV band absorption by BrC plays a significant role. I calculated AAE_{BrC} by fitting a power law equation to the retrieved values of BrC absorbing optical depth ($AAOD_{BrC}$)

from 305 – 368 nm. $AAOD_{BrC}(\lambda)$ = total $AAOD(\lambda)$ - $AAOD_{BC}(\lambda)$ (See Table 4.3) where $AAOD_{BC}$ is calculated assuming a constant refractive index from the AERONET retrievals at 440 nm. Our estimated AAE_{BrC} falls within the range of the previous measurements, *e.g.* 5.1 ± 1.9 in Indo-Gangetic Plain [Srinivas et al., 2016], 5.83 ± 0.51 in Beijing [Yan et al., 2015], and slightly less than the higher values of 6 – 7 measured for humic-like substances in the Amazon basin [Hoffer et al., 2006]. This confirms the spectral dependence that we believe describes South American forest burning BrC optical properties in chemistry- and aerosol-transport models.

4.4. Estimating the BrC volume fraction and BrC/BC ratio

Arola et al. [2011] inferred BrC volume fraction (f_{BrC}) in addition to BC volume fraction (f_{BC}), but only for cases when the AERONET retrieved *k* value at 440 nm is enhanced, compared to the longer visible and NIR wavelengths (670 – 1020 nm). This enhancement was attributed to additional BrC absorption and allowed the calculation of f_{BrC} using *a priori* information about the complex refractive index of BrC from previous measurements. The method uses Maxwell-Garnett (MG) mixing rule assuming an internal mixture of BC and BrC embedded in non-absorbing host. The assumed refractive indices for these components are given in Arola et al. [2011]. Our measurements show no evidence of enhanced BrC absorption at visible wavelengths (*i.e.*, insignificant *k* enhancements at 440 nm compared to longer wavelengths, Figure 4.4(a)), but significantly higher *k* in

UV. Therefore, this study advances the approach of Arola et al. [2011] to estimate f_{BrC} using enhanced k values at a longer UV-A wavelength (*i.e.,* 368 nm) which is not available from AERONET inversions. We also reduce the lower limit of the *a priori* BrC imaginary refractive index at 368 nm, $k_{BrC\text{-}368}$ = 0.025, from recent smoke chamber experiments [Saleh et al., 2014]. The upper limit on $k_{BrC\text{-}368}$ = 0.14 is assumed from laboratory measurements of more absorbing African smoke samples [Kirchstetter et al., 2004] (Figure 4.3). Consequently, a range of values of f_{BrC} from ~0.05 (using upper limit of $k_{BrC\text{-}368}$) [Kirchstetter et al., 2004] to ~0.27 (using lower limit of $k_{BrC\text{-}368}$) [Saleh et al., 2014] are calculated. The low sensitivity of f_{BrC} to the relative humidity is verified by varying the real part of the refractive index (n) of host [Schuster et al., 2009]. For instance, changing n by 10% would modify the BrC volume fraction by less than 2%. Assuming BrC mass density of 1.2 g/cm^3 [Turpin and Lim, 2001], the range of BrC column mass densities is estimated from ~11 to 61 mg/m^2, where the higher limit corresponds to the assumed lower limit of k_{BrC} [Saleh et al., 2014] typical for Amazon forest burning smoke.

The inferred BrC/BC column mass density ratio ranges from 1.7 to 9.5 (Table 4.1). Previous studies have reported OC/BC ratios ranging from 4.3 to 12.5 for tropical forests, 8.3 to 16.7 for the Cerrado (South American savanna), and 12.5 to 33.3 for boreal forests [Reid et al., 2005]. These ratios are larger than our measured BrC/BC ratios because total OC is composed of absorbing (BrC) and non-absorbing OC. Thus, the ratio of BrC to BC is expected to be smaller than the ratio of total OC to BC. The primary sources of aged smoke in Santa Cruz are

Cerrado and Amazon basin tropical forest burning, which is done for the purpose of clearing land for agricultural use, and the burning of crop residue after harvesting on existing agricultural land [Reid et al., 2004]. The highest smoke concentrations measured downwind at Santa Cruz are likely from tropical forest burning [Reid et al., 2004]. Our maximum estimated BrC/BC ratio (~9.5 using lower limit of k_{BrC} values from Saleh et al. [2014]) is consistent with the previous measurements for tropical forest and Cerrado burning. The lower limit of BrC/BC (~1.7) was obtained by assuming the upper limit of $k_{BrC\text{-}368}$ from laboratory measurements of African savanna smoke samples collected on filters during the Southern African Regional Science Initiative (SAFARI 2000) [Kirchstetter et al., 2004]. A good agreement is found between BrC/BC and the OC/BC ratio (1.7) measured from agricultural land [Reid et al., 2005].

4.5. Enhanced BrC spectral absorption in UV

Previous measurements [Kirchstetter et al., 2004; Saleh et al., 2014] of spectral absorption in the UV do not extend to biologically important wavelengths shorter than 350 nm. I use BrC volume fraction derived at 368 nm to infer the spectral dependence of k_{BrC} at shorter, more biologically active UV-B wavelengths down to 305 nm (Figure 4.5). Specifically, the retrieved k_{ret} is partitioned into its k_{BrC} and k_{BC} components assuming that the smoke layer can be represented by a mixture of BC and BrC embedded into a non-absorbing host. The partitioning is carried out by applying the MG mixing rule to express the measured effective

imaginary refractive index (k_{ret}), in terms of the volume fractions of BC (f_{BC}) and BrC (f_{BrC}) and their complex refractive indices (k_{BC} and k_{BrC}). The real part of the refractive index for the non-absorbing host, BC, and BrC is assumed to be spectrally constant as in Arola et al. [2011]. Following this approach, k_{BrC} values at 305, 311, 317, 325, and 332 nm are calculated by fitting the retrieved spectral k_{ret} using the MG mixing rule with the previously calculated and spectrally independent f_{BC}, f_{BrC}, and k_{BC}. The calculated spectral dependence of k_{BrC} in the UV-B (characterized by the power exponent, w = 5.4 – 5.7) is significantly stronger than previous laboratory estimates, e.g. by Kirchstetter et al. [2004] (w = 3.9) and smoke chamber experiments by Saleh et al. [2014] (w = 1.6) (Figure 4.5). Thus, our measurements show that BrC in aged Amazonian smoke absorbs UV solar radiation with stronger spectral dependence than previously reported. This result has important implications for tropospheric photochemistry and biological effects of UV-B as discussed next.

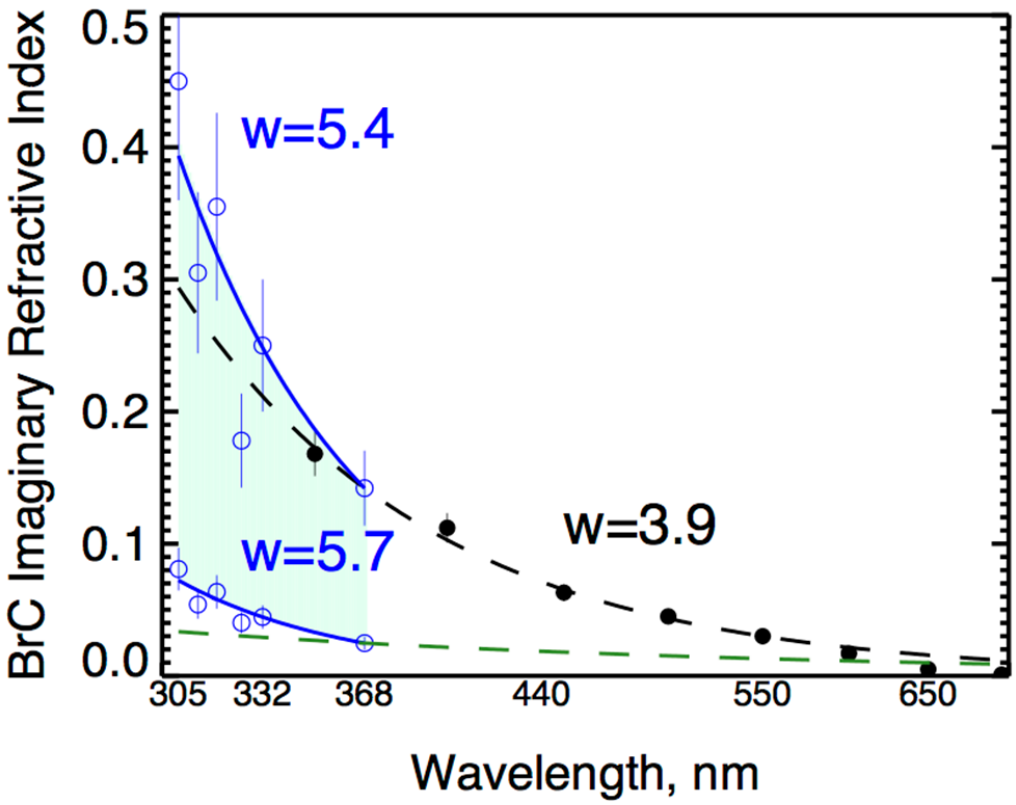

Figure 4.5. The inferred spectral dependence of BrC imaginary refractive index (k_{BrC}) in UV (blue circles with 20% error bars). Black circles show the upper limit for $k_{BrC\text{-}368}$ values derived from African savanna burning samples (10% uncertainty) [Kirchstetter et al., 2004]. Lower limit of $k_{BrC\text{-}368}$ parameterization (green dashed lines) is based on smoke chamber experiments [Saleh et al., 2014] showing low spectral dependence (w=1.6). The shaded area shows the variability range in our inferred k_{BrC} in the UV wavelengths. We inferred much larger spectral dependence (w ~ 5.4 – 5.7) in the UV-B than previously reported (~1.6 – 4) in longer UV and visible wavelengths [Kirchstetter et al., 2004; Saleh et al., 2014].

I further convert our calculated AAOD for BrC ($AAOD_{BrC}$) and column mass density for BrC into specific mass absorption efficiency for BrC (MAE_{BrC}) in the UV wavelengths (Table 4.3). MAE_{BrC} is a useful parameter to compare with laboratory measurements and can be directly used in aerosol transport models. It has not been previously measured in the field under smoky conditions. The derived MAE_{BrC} spectral dependence for smoke shows a strong increase at the shorter UV-B wavelengths similarly to those previously measured in anthropogenic aerosols [Barnard et al., 2008]. The maximum and minimum values of MAE_{BrC} (Table 4.3) are associated with the assumed range of $k_{BrC\text{-}368}$ [Kirchstetter et al., 2004; Saleh et al., 2014]. Our minimum values (MAE_{BrC} = 0.9 – 2.9 m^2/g) are comparable with the previous measurements of low absorbing organic compounds in smoke from different locations, such as Alaska and Siberia [Chakrabarty et al., 2016], Indo-Gangetic Plain [Srinivas et al., 2014], Beijing [Yan et al., 2015], Colorado [Lack et al., 2012], and Amazon basin [Hoffer et al., 2006]. Our maximum values (MAE_{BrC} ~ 5 – 16 m^2/g) are consistent with previous measurements for more absorbing organic aerosols originated from urban pollution [Barnard et al., 2008] and savanna burning [Kirchstetter et al., 2004]. The different ranges of MAE_{BrC} for different wavelengths in Table 4.3 suggest that BrC absorption should be treated regionally in chemical transport models. The upper limits of MAE_{BrC} ranges should be used in areas where there is savannah burning. The lower limits of MAE_{BrC} ranges should be used in areas where BrC is expected to be less absorbing. For Santa Cruz, the lower limits are more appropriate.

Table 4.3. Estimated BrC mass absorption efficiency (MAE_{BrC}). MAE_{BrC} in the UV wavelengths (MAE_{BrC}=0 in the visible wavelengths) is estimated using specific $AAOD_{BrC}$ divided by BrC column mass density. The maximum and minimum values of MAE_{BrC} are associated with the range of previously measured k_{BrC} at 368 nm [Kirchstetter et al., 2004; Saleh et al., 2014].

Wavelength [nm]	Total AAOD	$AAOD_{BC}$	$AAOD_{BrC}$ =AAOD-$AAOD_{BC}$	MAE_{BrC} [m^2/g] (min [$k_{BrC-368}$], max [$k_{BrC-368}$])
305	0.296	0.121	0.175	(2.9 – 16.1)
311	0.233	0.120	0.113	(1.8 – 10.4)
317	0.255	0.117	0.138	(2.3 – 12.7)
325	0.189	0.115	0.074	(1.2 – 6.8)
332	0.212	0.114	0.098	(1.6 – 9.0)
368	0.156	0.102	0.054	(0.9 – 5.0)

*min [$k_{BrC-368}$]: minimum value of $k_{BrC-368}$ from Saleh et al. [2014]

*max [$k_{BrC-368}$]: maximum value of $k_{BrC-368}$ from Kirchstetter et al. [2004]

4.6. BrC absorption effect on surface UV and photochemistry

Excessive exposure to UV-B radiation causes damage to the eyes, suppression of the immune system, photoaging, and skin cancer [Lautenschlager et al., 2007; Mancebo and Wang, 2014]. There is also mounting evidence that it alters plant development and growth [Teramura and Sullivan, 1994; Rousseaux et al., 1999]. Under unpolluted and clear sky conditions, the levels of surface UV are high in Santa Cruz because of low overhead ozone and low solar zenith angles. Thus, the enhanced absorption of BrC at the most damaging UV-B wavelengths might play a role as a natural sunscreen. To quantify the specific spectral reduction of the surface UV due to absorption by BrC, radiative transfer simulations of the spectral surface UV with and without BrC absorption are performed. Figure 4.6 shows that the effect of BrC absorption causes an additional 20 – 25% reduction at the most damaging UV-B wavelengths reaching the surface (*i.e.,* 305 nm) compared to the BC only (spectrally flat) absorption. This previously unaccounted reduction in surface UV-B irradiance is important for health risk assessments [Lautenschlager et al., 2007; Mancebo and Wang, 2014] and estimating UV-B effects on crop yield [Teramura and Sullivan, 1994; Rousseaux et al., 1999]. Unaccounted absorption by BrC can also explain the positive bias in satellite derived surface UV-B compared to ground-based measurements [Krotkov et al., 2005b; Arola et al., 2005]. The BrC absorption effect is smaller at longer UV-A wavelengths (~10% reduction at 320 – 330 nm).

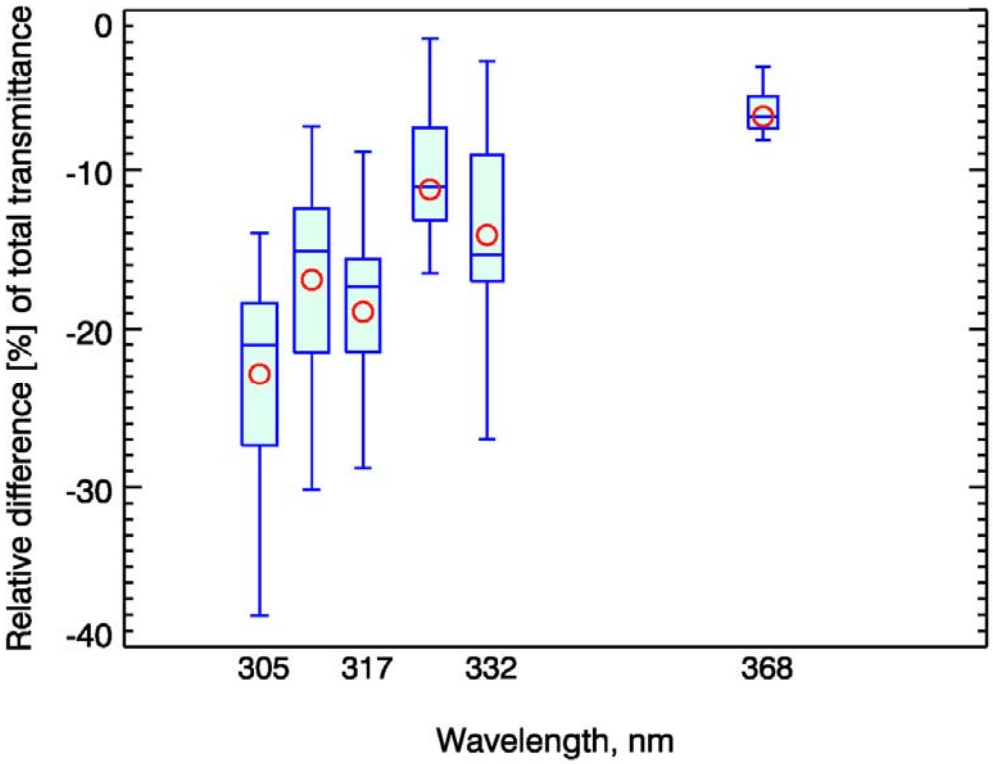

Figure 4.6. Enhanced BrC absorption causes 20% decrease in the most damaging short wavelength surface UV-B irradiance (305 – 320 nm). Box-whisker plots show the relative difference [%] between our measured surface spectral UV (BC plus BrC absorption) and model (assuming BC only) surface UV: ($UV_{meas} - UV_{BC}$) / UV_{BC} × 100%. Red circles show independent model estimates using different LibRadtran (http://www.libradtran.org) RTM for the fixed SZA (45°) and ozone column amounts (272 DU).

The following photochemical reactions explain that J_{NO2} and J_{O3} play critical roles in ozone production and loss, respectively.

$$NO_2 + h\nu \rightarrow NO + O \qquad \lambda \leq 430 \text{ nm, peak} \sim 390 \text{ nm} \tag{4.6}$$

$$O + O_2 \rightarrow O_3 \tag{4.7}$$

$$O_3 + h\nu \rightarrow O_2 + O(^1D) \qquad \lambda \leq 318 \text{ nm, peak} \sim 308 \text{ nm} \tag{4.8}$$

$$O(^1D) + H_2O \rightarrow 2OH \tag{4.9}$$

The stronger absorption of BrC at UV-B wavelengths affects the atmospheric photochemistry. Dickerson et al. [1997] and other studies [Castro et al., 2001; Hodzic et al., 2007] show that carbonaceous aerosols reduce the photolysis rate of NO_2 (J_{NO2}) responsible for ozone production by 10 – 30%. In extreme cases, J_{NO2} is reduced by 70% near the ground, while it is increased by 40% above the smoke layer due to aerosol backscattering [Albuquerque et al., 2005]. Yet, these studies [Dickerson et al., 1997; Castro et al., 2001; Albuquerque et al., 2005; Hodzic et al., 2007] did not have the information necessary to discriminate between BC and BrC absorption.

Our measurements allow us to isolate the effect of BrC absorption on photolysis rates (Figure 4.7) and ozone production using a radiative transfer model and a chemical box model. The enhanced absorption of BrC at the UV-B

wavelengths around 308 nm (Figure 4.5) decreases the photolysis rate of O_3 (J_{O3}) linked to the OH production by ~25% at the surface relative to BC only absorption (Figure 4.8). But smaller absorption at longer UV wavelength (390 nm) decreases J_{NO2} linked to the ozone production mechanism by only 10%. Photolysis of carbonyls such as aldehydes is also inhibited by BrC, and this slows production of radicals OH, HO_2, and RO_2. Our box chemical model runs considering all major species subject to rapid photolysis (e.g., HCHO, CH_3CHO, CH_3OOH, HONO, H_2O_2, CHOCHO, CH_3COCHO, and CH_3COONO_2) reveal that the optical effects of BrC inhibit net surface and lower tropospheric ozone production by up to 18% shown in Figure 4.9. A recent study [Hammer et al., 2016] also reports that the absorption of BrC decreases OH concentration in South America in September by up to 35%. The reduced ozone and VOC photolysis rates due to BrC reduce concentrations of radicals OH, HO_2, and RO_2 by up to 17%, 15%, and 14%, respectively (Figure 4.10), which in turn, produces less surface ozone. The reduction in the HO_x (OH + HO_2) and RO_2 concentration also decreases the rate of removal of many other trace gases.

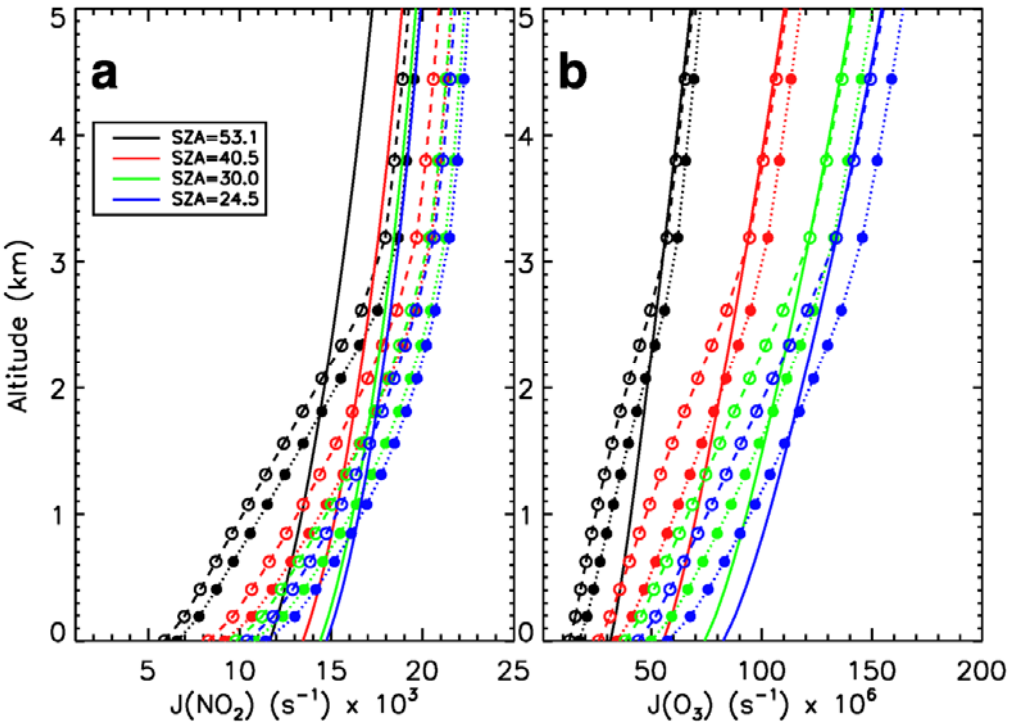

Figure 4.7. Model simulation for BrC effect on the photolysis rate. The vertical profile of (a) J_{NO2} and (b) J_{O3} from SZA=24.5° to SZA=53.1°. Solid line: no aerosol, dotted line with filled circle: BC only, and dashed line with open circle: BC+BrC (See Table 4.2 for details). Comparing with the no aerosol case, J_{O3} and J_{NO2} for both BC only and BC+BrC cases show reduced values below the smoke layer due to the absorption of solar radiation but increased values above the smoke layer due to the higher backscattering. Interestingly, BrC causes not only more absorption below the smoke layer but also less backscattering above the layer than BC. In other words, BrC absorbs more UV flux in the boundary layer and cause less backscattering flux above the layer.

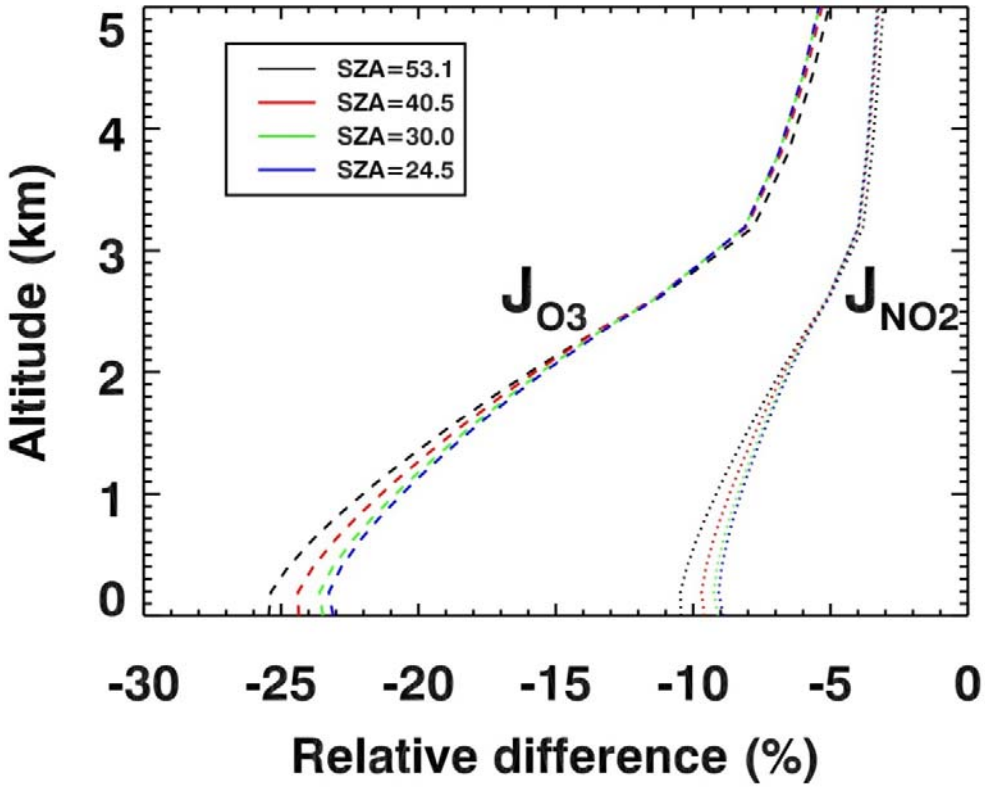

Figure 4.8. Modeling the impact of BrC absorption on the rate of tropospheric ozone production. The vertical profiles show relative differences [%] in photolysis rates for NO_2 (J_{NO2}: dotted line) and ozone to $O(^1D)$ (J_{O3}: dashed line) due to enhanced BrC UV absorption for different SZAs using a radiative transfer model. We assumed a homogeneously distributed smoke layer below 3 km as measured by space-based lidar. The ozone loss mechanism linked to J_{O3} is more significantly reduced than the production mechanism linked to J_{NO2}. Input k_{ret} values for calculating photolysis rates are described in Table 4.2.

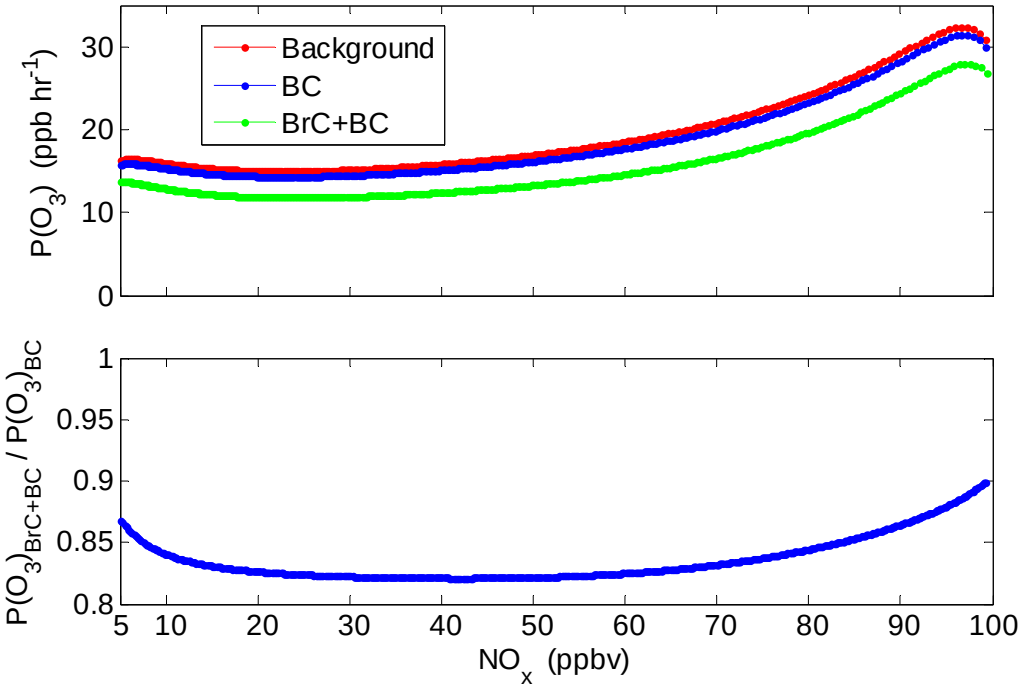

Figure 4.9. Modeling the impact of BrC absorption on surface ozone. (a) Net ozone production ($P(O_3)$) in three cases: background (no aerosols), BC, and BrC+BC, and (b) the ratio of $P(O_3)$ in the BrC+BC case to $P(O_3)$ in the BC case. The box model was initialized with 200 ppbv VOCs and 100 ppbv NO_x. Both VOCs and NO_x are unconstrained in the model. The plotted NO_x range of 5 – 100 ppbv reflects ~2 – 3 days that are needed for a smoke plume to travel from the sources in Amazonia to Santa Cruz.

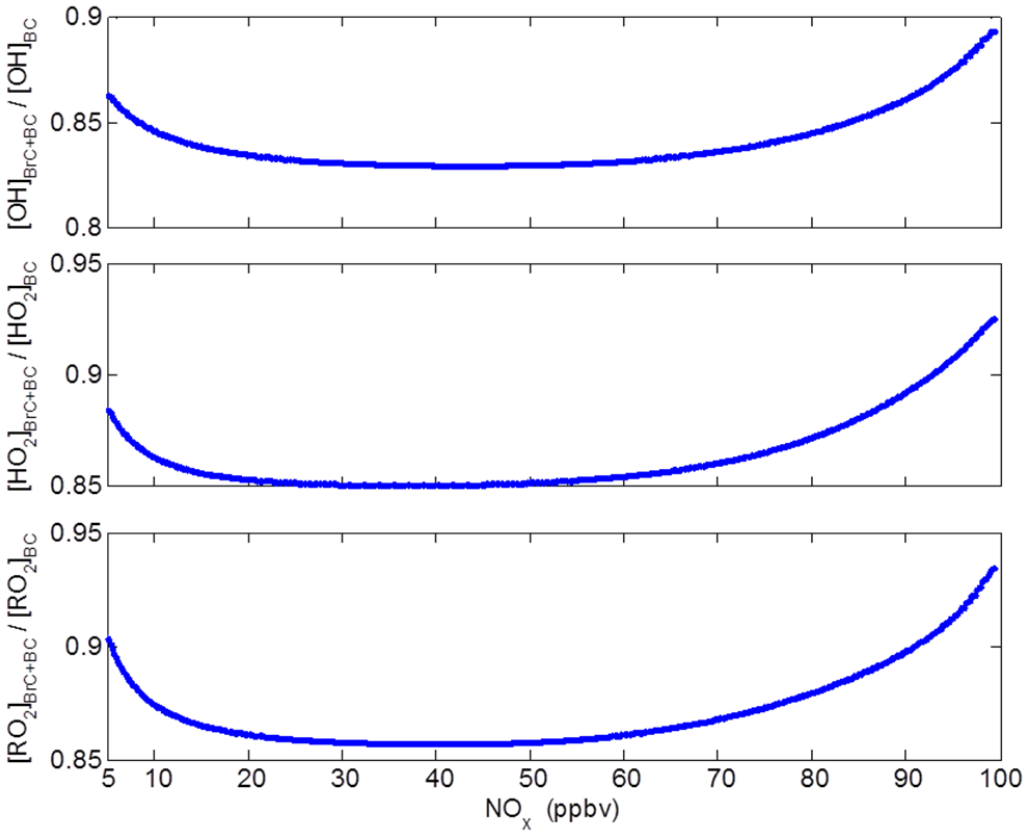

Figure 4.10. Modeling the impact of BrC absorption on OH, HO_2, and RO_2 concentration. (a) The ratio of [OH] in the BrC+BC case to [OH] in the BC case, (b) The ratio of $[HO_2]$ in the BrC+BC case to $[HO_2]$ in the BC case, and (c) The ratio of $[RO_2]$ in the BrC+BC case to $[RO_2]$ in the BC case. The box model was initialized with 200 ppbv VOCs and 100 ppbv NO_x. Both VOCs and NO_x are unconstrained in the model. The plotted NO_x range of 5 – 100 ppbv reflects ~2 – 3 days that are needed for a smoke plume to travel from the sources in Amazonia to Santa Cruz.

4.7. Summary and Conclusion

The combination of surface and space-based remote sensing of aerosol optical properties shows that biomass burning of the Cerrado, Amazonian forest, and agricultural lands in South America generates substantial amounts of light absorbing "brown carbon", BrC. For the first time this study have characterized the wavelength dependence of BrC absorption at the shortest and most biologically and chemically active UV-B wavelengths reaching Earth's surface under aged biomass burning smoke conditions. The estimated optical properties of this BrC differ significantly from the optical models of BC or OC currently assumed in chemical- and aerosol-transport models. While the strong absorption of UV-B radiation seen for BrC can ameliorate some of the adverse health effects of smoke, biomass burning aerosols remain major environmental and health hazards [Johnston et al., 2012].

Our estimated range of the column volume fraction of BrC is 0.05 to 0.27 and of its column mass density is ~11 to 61 mg/m^2. The best estimate is likely close to the upper limit because the lower limit represents more absorbing BrC (therefore, lower mass) from high temperature burn conditions in southern Africa savanna. The mass absorption efficiencies of BrC are largest at 305 nm, but vary significantly (e.g., 2.9 to 16.1 m^2/g) due to variability in BrC column effective imaginary refractive index, k_{BrC}. Regardless of this uncertainty in absolute values of k_{BrC}, this study was able to constrain its spectral dependence with improved accuracy. The best fit to the spectral dependence of k_{BrC} in UV wavelengths is the

power-law with retrieved exponent of 5.4 to 5.7.

Our derived total (BC + BrC) absorption Angstrom Exponent (AAE) in UV wavelengths (~3.0 in the range 305 – 368 nm) agrees well with the OMI assumed AAE (~2.8 between 354 nm and 388 nm) [Jethva and Torres, 2011], validating this *a-priori* assumption regarding *k* spectral dependence for smoke aerosols.

The primary difference between BrC and BC is the strong spectral dependence of the absorption of UV radiation by BrC. In comparison to BC alone, the combination of BC and BrC strongly decreases surface UV-B actinic flux, photolysis rates, and the rates of production of radicals RO_x (RO_x = $OH+HO_2+RO_2+RO$) and O_3. Although a complex and nonlinear relationship exists with respect to concentrations of nitrogen oxide precursors, the observed optical properties of BrC reduce the rate of ozone production by up to ~18% over the full range of possible NO_x values, from 100 ppb near the fires to 5 ppb well downwind of the fires. Radicals are also produced more slowly, and the lower concentrations of RO_x mean longer lifetimes for ozone and its precursors (NO_x and VOCs). This could lead to greater ozone concentrations downwind. The net impact will depend on the rate of dispersion and non-linear photochemistry including the speciation of VOCs. Future studies should include sufficient ambient measurements to initialize and constrain a 3-D chemical transport model.

Chapter 5: Multi-instrument approach for measuring spectral aerosol absorption and comparison with SKYNET

5.1. Introduction

The SKYNET is an international network for studying aerosol, cloud, and solar radiation [Nakajima et al., 1996; 2007]. Using the direct sun and diffuse sky radiance, aerosol optical properties (e.g., AOD, column effective SSA, refractive index, and volume particle size distribution (PSD)) are retrieved. The processing software package called SKYRAD.pack was developed by Nakajima et al. [1983; 1996]. With the growing interest in aerosol composition retrieval, shorter UV (340 and 380 nm) and longer NIR (1627 and 2200 nm) channels were added to the PREDE POM-02 skyradiometer used by SKYNET.

Using SKYNET measurements in Hefei, China, Wang et al. [2014] reported smaller SSA at 380 nm during the autumn (0.93 ± 0.04) and winter (0.91 ± 0.04) than that in spring (0.95 ± 0.03) and summer (0.97 ± 0.02). They explained lower SSA by absorption from carbon in smoke from the local farm burning in autumn and urban black carbon (BC) absorption in winter. Their study shows that seasonal differences of SSA are within 0.05. Thus, reducing and estimating the uncertainties of SSA retrievals is important because even a small bias in SSA could lead to significant errors in aerosol radiative forcing and also the misinterpretation of aerosol composition.

Although the SKYNET provides SSA at UV wavelengths, recent comparison studies focus on visible and NIR wavelengths due to the lack of co-incident measurements of aerosol and gaseous absorption properties in the UV [Che et al., 2008; Khatri et al., 2016].

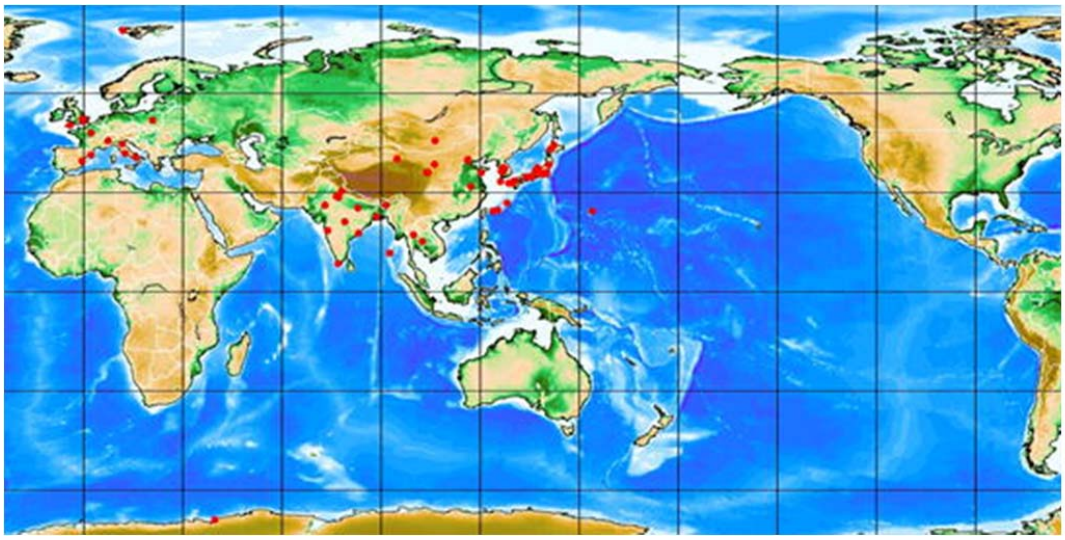

Figure 5.1. SKYNET/Skyradiometer site map. SKYNET is the international network for aerosol, clouds, and solar radiation studies (source: http://atmos2.cr.chiba-u.jp/skynet/).

The objective of this chapter is to compare the SKYNET-retrieved SSA in UV and visible wavelengths with the SSA derived from a combination of AERONET, MFRSR, and Pandora inversion retrievals (hereafter referred to as AMP) from Seoul, South Korea during and after KORUS-AQ international field campaign in 2016. The advantage of using the AMP inversion for the comparison against the SKYNET inversion is that it retrieves SSA in UV as well as visible

and NIR wavelengths (305 – 1020 nm). The AERONET inversion provides SSA only at four visible and NIR wavelengths, i.e., 440, 670, 860, and 1020 nm. Therefore, it is not possible to compare the SKYNET-retrieved SSA in UV wavelengths using AERONET retrievals alone.

5.2. Experimental site and instrumentation

The data used in this study are UV- and VIS-MFRSR, SKYNET sun-sky radiometer and AERONET measurements made from April 5 to August 24, 2016 on the roof of Science Hall, Yonsei University at Seoul in South Korea. Recently, a field study, called the Korea U.S.-Air Quality (KORUS-AQ) has been carried out to understand and monitor air quality over the South Korean peninsula during May to June 2016 (https://espo.nasa.gov/home/korus-aq/content/KORUS-AQ). The Seoul metropolitan region has a population of 25 million. Also, Seoul is located in the downwind region from heavy aerosol pollution sources: dust from the Taklimakan and Gobi deserts, biomass burning aerosols from wildfires and crop fires in China, Russia, and North Korea, and fossil fuel combustion from industrial areas in East China.

To measure UV aerosol optical properties from these sources, the modified UV-MFRSR and the modified VIS-MFRSR were installed on the roof of Yonsei University in Seoul, South Korea (Table 5.1 and Figure 5.2). Yonsei University has been operating a CIMEL sunphotometer as part of the AERONET network since 2011 as well as a new Pandora spectrometer system to measure

trace gases (ozone, NO_2, SO_2, and HCHO). To facilitate the AERONET-to-MFRSR calibration transfer and to compare aerosol absorption products such as SSA and the imaginary part of the refractive index (k), the 300-nm filter of the UV-MFRSR and unfiltered channel of the VIS-MFRSR were re-furbished with 440-nm filters, used by the AERONET. In addition, the 317- and 368-nm filters of the UV-MFRSR were replaced with 340- and 380-nm filters, also used by the AERONET. A summary of the UV- and VIS-MFRSR instruments can be found in Table 5.1.

Figure 5.2. Instrumentation at Yonsei University in Seoul, South Korea. Top-left: UV-MFRSR, top-right: VIS-MFRSR, bottom-left: Skyview, and bottom-right: SKYNET Skyradiometer.

Table 5.1. Instruments and wavelengths of retrieved absorption properties. Each superscript (a – g) indicates matching channels in AERONET, MFRSR, and SKYNET.

Instruments	Measurements	Wavelengths
CIMEL sun and sky photometers (AERONET)	Direct sun and almucantar sky radiance, Filters (2 – 10 nm)	439[a], 675[b], 870[c], 1020[d] nm
Modified UV-MFRSR	Diffuse and total irradiance, Filters (2 nm)	305, 311, 325, 332, 340[e], 380[f], 440[a] nm
Modified VIS-MFRSR	Diffuse and total irradiance, Filters (2 nm)	415[h], 440[a], 500[g], 615, 673[b], 870[c] nm
Skyradiometer (SKYNET)	Sun and sky radiance, Filters (10 nm)	340[e], 380[f], 400[h], 500[g], 675[b], 870[c], 1020[d] nm

5.3. Data and Methodology

5.3.1. Skyradiometer (SKYNET)

Two kinds of on-site SKYNET calibrations are available to determine the solar calibration constant. The first way is to use the calibration constants derived by the on-site Improved Langley (IL) method [Campanelli et al., 2004]. This method can characterize possible temporal variation of the calibration constants (e.g., due to temperature variations). The second way is to use the calibration

constants derived through the comparison with the master skyradiometer (hereafter referred to as ‘master calibration’), which was calibrated at the Mauna Loa Observatory (MLO) in December 2015. This method cannot consider the possible temporal variations of the calibration constants between the comparisons, unless a post-deployment calibration is used for time interpolation with the pre-deployment calibration.

5.4. Comparison of single scattering albedo between AERONET and MFRSRs

Currently routine ground measurements of spectral absorption optical depth (or column effective single scattering albedo, SSA) are limited to the 4 discrete visible wavelength bands by AERONET almucantar inversions (440, 670, 870, and 1020 nm). An AERONET CIMEL sunphotometer has 340 and 380 channels but does not provide SSA inversions because it does not perform sky radiance measurements at those UV channels. But it should be noted that the final calibration has not yet been applied to the AERONET and SKYNET data. Therefore, AOD and SSA from the cloud-screened level 1.5 AERONET retrieval data are used in this study. Instead, I applied the AERONET level 2 quality control limits (e.g., sphericity > 95%). The details are shown in Table 3.1.

In Figure 5.3, the SSA at 440 nm from AERONET is compared with SSA from the AMP retrievals using UV-MFRSR and VIS-MFRSR. Both instruments

provide best quality retrievals of SSA at high turbidity conditions (AOD at 440 nm (AOD_{440}) > 0.4) [Dubovik et al., 2002; Krotkov et al., 2005b; Mok et al., 2016]. Red dots shown in Figure 5.3 are the cloud-screened level 1.5 AERONET retrieval data. For these conditions, the average SSA at 440 nm (SSA_{440}) from both UV-MFRSR and VIS-MFRSR (~ 0.92) are in excellent agreement with the corresponding AERONET SSA (~0.93) as shown in Table 5.2. The root mean square deviation, RMSD ~ 0.02 – 0.027 is similar to the previous studies [Dubovik et al., 2002b; Estelles et al., 2012].

Relaxing AOD_{440} criteria allows analyzing larger statistical sample of the MFRSR-AERONET matchups (Table 5.2). The mean SSA_{440} values using relaxed filter (AOD_{440} > 0.2, shown as blue and red dots) is reduced by ~0.02 compared to the restricted sample using AERONET level 2 criteria (AOD_{440} > 0.4). The SSA variability (standard deviation) is insignificantly increased (less than 0.01). The increased variability reflects cases with smaller AOD, showing stronger absorption (SSA ~ 0.9). The RMSD for strict and relaxed samples are almost the same (Table 5.2). The good agreements of SSA at the common overlapping wavelength 440 nm from UV-MFRSR, VIS-MFRSR, and AERONET provide additional confidence in the MFRSR and AERONET retrievals for relaxed conditions with AOD_{440} > 0.2. Thus, I utilize the combined AERONET-MFRSR-PANDORA (AMP) SSA retrievals allowing AOD_{440} > 0.2 to compare with the SKYNET SSA retrievals.

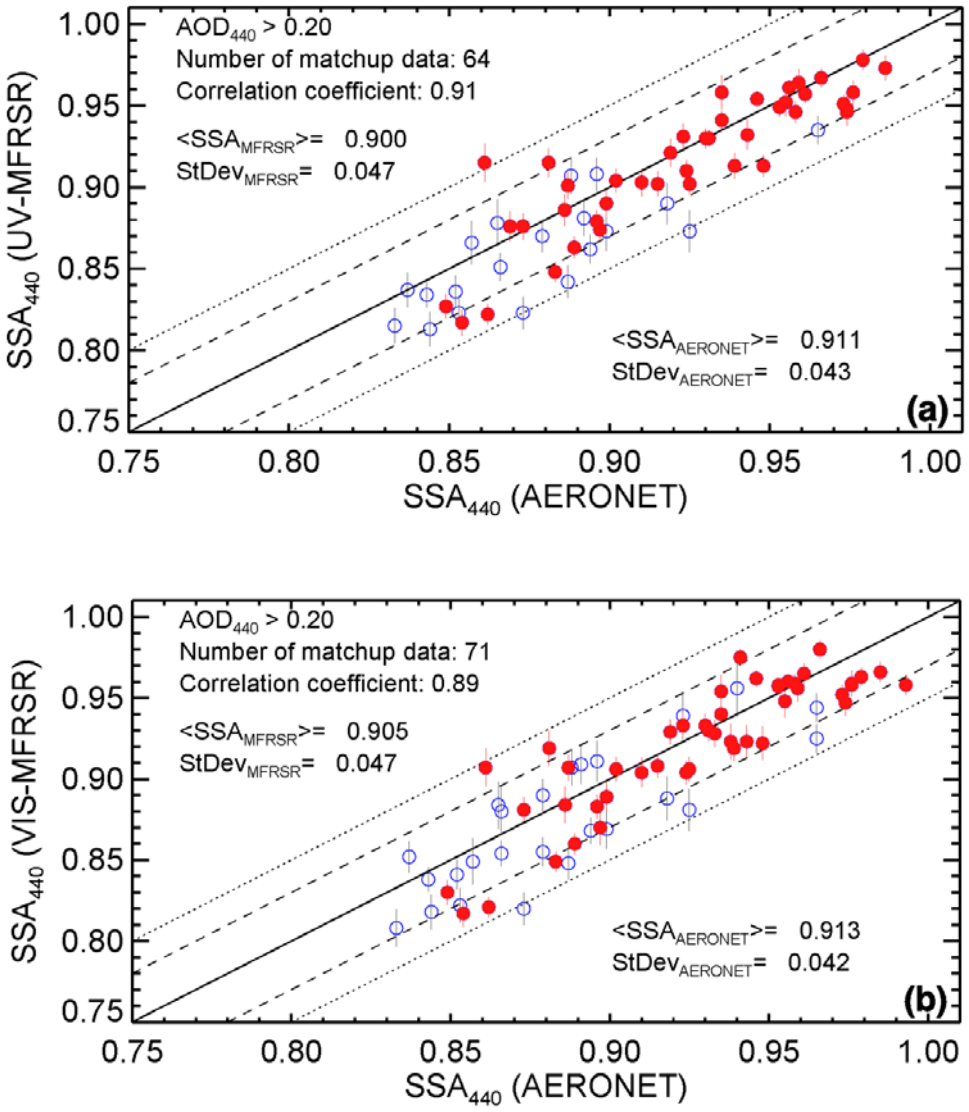

Figure 5.3. Comparison between SSA from the AERONET almucantar retrievals and SSA retrieved from (a) UV-MFRSR and (b) VIS-MFRSR at 440 nm. MFRSR SSA errors are calculated assuming 3% error in diffuse to direct ratio. For AERONET default 0.03 SSA errors are assumed. Red dots correspond to AOD_{440} > 0.4 criteria consistent with the cloud-screened level 1.5 AERONET data. Mean SSA for both UV-MFRSR and VIS-MFRSR is ~0.90 and that for AERONET is ~0.91.

Table 5.2. Comparison of SSA at 440 nm between AERONET and AMP inversions.

	$0.2 \leq AOD_{440} < 0.4$		$AOD_{440} > 0.4$	
	AERONET	MFRSR	AERONET	MFRSR
AERONET and UV-MFRSR matchup				
Mean	0.878	0.861	0.925	0.918
Standard deviation	0.033	0.034	0.039	0.042
Correlation	0.801		0.895	
Number	20		44	
RMSD	0.027		0.020	
AERONET and VIS-MFRSR matchup				
Mean	0.886	0.874	0.928	0.922
Standard deviation	0.037	0.041	0.038	0.041
Correlation	0.826		0.880	
Number	25		46	
RMSD	0.026		0.020	

5.5. Comparison of single scattering albedo between AMP and SKYNET

Previous comparison studies of aerosol properties between AERONET and SKYNET [Campanelli et al., 2004; Che et al., 2008] show better agreements for AOD than for SSA visible and NIR wavelengths. For example, Khatri et al. [2016] found that the SKYNET SSA is larger than the AERONET SSA. To compare AMP and SKYNET retrievals, I compute the means and standard deviations using available SKYNET retrievals within ± 8.5 minutes of the AMP retrievals. Initially, I compared 2 sets of SKYNET AOD and SSA data: (1) using on-site improved Langley calibration SSA(IL), and (2) using intercalibration against master instrument SSA(master) (Figure 5.4). However, I focus on SKYNET SSA (master) data, because SSA spectral dependence is similar to the MFRSR-retrieved SSA spectral dependence in UV, i.e., SSA_{340} (master) < SSA_{380} (master). I found that, on average, SKYNET SSA at 380 and 400 nm are lower compared to MFRSR data. The bias cannot be explained by AOD differences, because SKYNET AOD_{340} (master) shows good agreement with the AERONET AOD_{340} (Figure 5.5) The likely source of the bias is unreasonably high value of the spectrally invariant surface albedo (0.1, see Figure 5.6) assumed in SKYNET SSA retrievals, which leads to underestimated value of SSA even if AOD retrievals were accurate [Hashimoto et al., 2012].

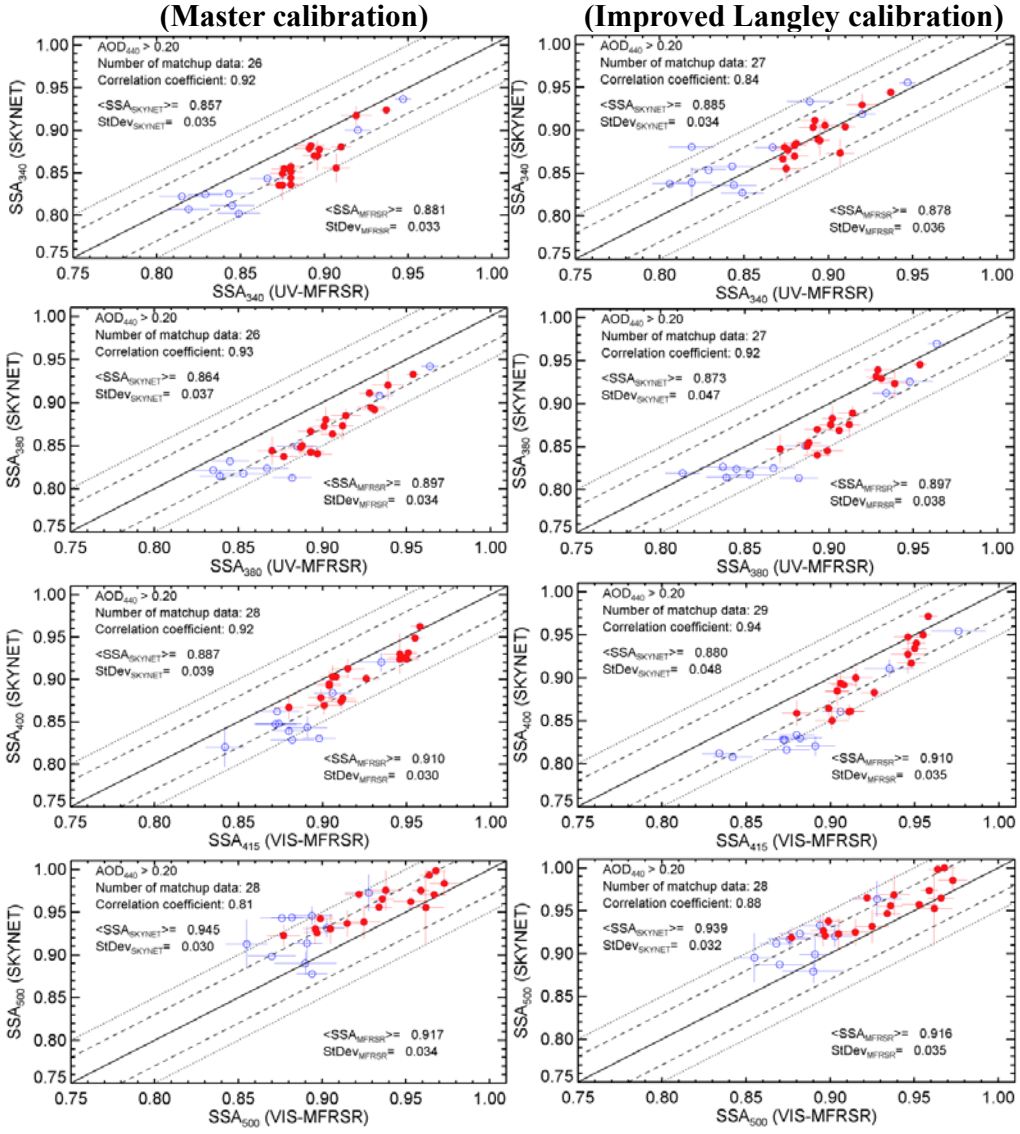

Figure 5.4. Comparisons of AMP-retrieved SSA with SKYNET-retrieved SSA using the master calibration (left) and the IL calibration (right) with surface albedo=0.1. Red dots were filtered using $AOD_{440} > 0.4$ to correspond the best quality level 2 AERONET data.

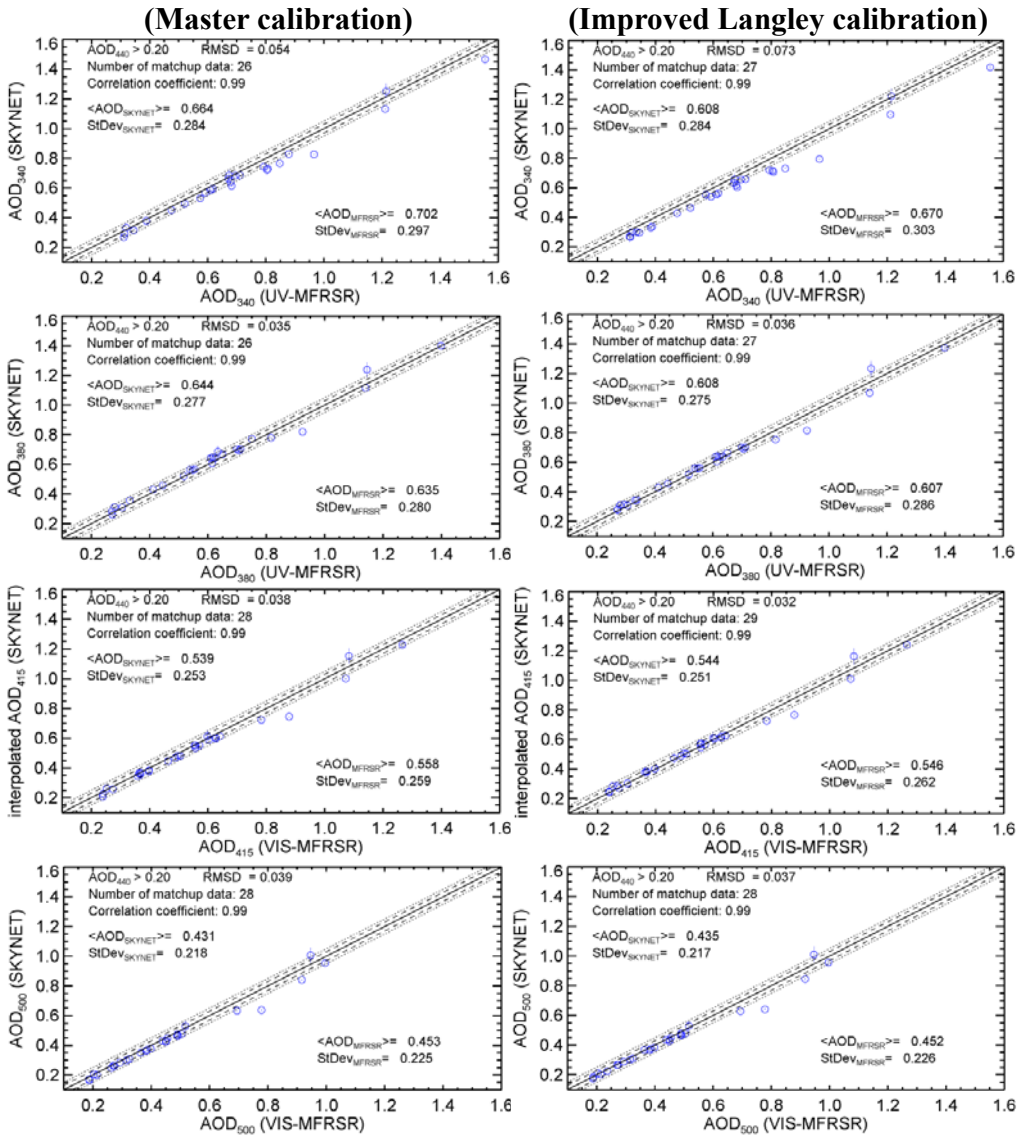

Figure 5.5. Comparisons of AMP-retrieved AOD with SKYNET-retrieved AOD using the master calibration (left) and the IL calibration (right) with surface albedo=0.1. RMSD and number of data are described in Table 5.4. AMP/AOD is AERONET/AOD used for inversions and/or interpolated to UV wavelengths and times. Dotted and dashed lines are 0.03 and 0.05 offset, respectively.

5.6. Factors of discrepancy

5.6.1. Discrepancy of AOD

Prior to comparison of SSA, the agreement of AOD is very important and has to be demonstrated. This is because the overestimation in AOD can lead to the underestimation in SSA [Dubovik et al., 2000; Khatri et al., 2016]. The discrepancy of AOD is typically attributed to problems in instrumental calibrations [Khatri et al., 2016]. The MFRSR inversion uses the same V_0 for direct and diffuse irradiance measurements as described in Chapter 2. Thus, V_0 does not affect the diffuse to direct ratio (DD) irradiance measurements that we fit in retrievals of SSA. Unlike in previous studies [Khatri et al., 2016], I found that SKYNET AOD calibrated against master instrument shows good agreement with the AERONET AOD (Figure 5.5) and is not a likely source of the SSA differences.

5.6.2. Surface albedo

Surface albedo has an important impact on the retrievals of SSA in UV [Corr et al., 2009]. The AMP inversions use the AERONET-provided spectral surface albedos from 440 nm to 1020 nm derived from MODIS land products [Moody et al., 2005]. The shortest wavelength at which surface albedo is obtained is 440 nm. Therefore, we assumed that this value applies to MFRSR retrievals in

UV wavelengths.

Figure 5.6 compares surface albedo used for the AMP inversion with that used for SKYNET inversion. There is little variability in AERONET surface albedo (± 0.01) at 440 nm. The operational SKYNET retrievals use spectrally flat surface albedo (0.1) at all wavelengths [Hashimoto et al., 2012]. The SKYNET-assumed surface albedo is close to the AERONET surface albedo at 670 nm as in Figure 5.6. However, it greatly overestimates AERONET surface albedo at 440 nm (~0.04 as estimated by MODIS). Overestimated value of surface albedo in the SKYNET inversion will lead to underestimated value of SSA at 440 nm [Hashimoto et al., 2012] and at shorter wavelengths: 340, 380, and 400 nm (Figure 5.4), where the SKYNET-retrieved SSA is larger than the AMP-retrieved SSA.

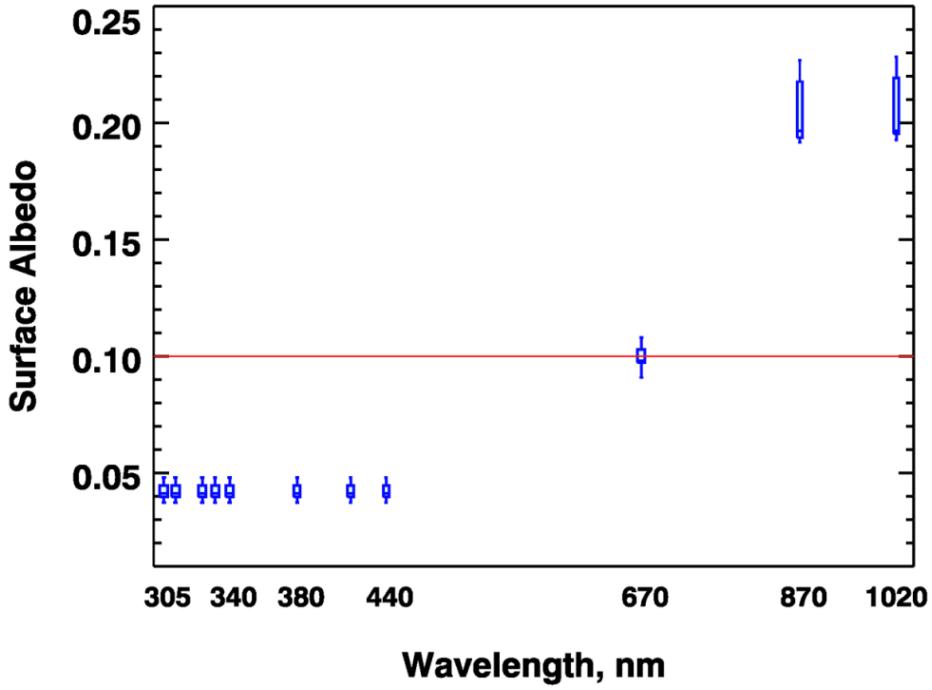

Figure 5.6. Surface albedo used for AMP (blue boxes) and SKYNET (red line) SSA inversions. Boxes show 25% and 75% percentiles of the albedo distribution and whisker show albedo outliers for AERONET retrievals at 440 nm and shorter wavelengths. Constant surface albedo of 0.1 was assumed for all wavelengths in SKYNET retrievals, is shown as red solid line.

Re-processing SKYNET inversions using new median surface albedo (0.04), consistent with the AERONET retrievals, drastically improves agreement with AERONET SSA (Figure 5.7). Mean SSA difference between AMP and SKYNET at 340 nm for $AOD_{440} > 0.2$ is ~ 0.002. The SKYNET-derived SSA at 400 nm (SKYNET/SSA_{440}) also shows good agreement with the AMP-derived SSA at 415 nm (AMP SSA_{415}) (Figure 5.7).

Figure 5.8 shows overall better agreement of the retrieved spectral SSA using AERONET consistent surface albedo (~0.04) at 340, 380, and 400 nm. Still, SKYNET-derived SSA at 380 nm shows slight underestimation compared to the AMP-derived SSA. This underestimation might be explained by unaccounted gaseous (NO_2) absorption discussed in next section. In other words, aerosol absorption at 380 nm is overestimated without consideration of NO_2 absorption [Krotkov et al., 2005c]. However, SKYNET retrievals using lower surface albedo (0.04) results in greater SSA overestimation at 500 nm. As shown in Figure 5.6, it is noted that the surface albedo at 500 nm should be higher (> 0.04) since vegetation has a local peak at 500 nm, and since there are trees in some directions (See Figure 5.2) from Yonsei University Science Building rooftop. In addition, non-vegetated surfaces show increasing reflectance from 440 to 670 nm. Therefore, the surface albedo might be expected to be closer to 0.1 as for 670 nm in AERONET than for the 0.04 at 440 nm (Figure 5.6).

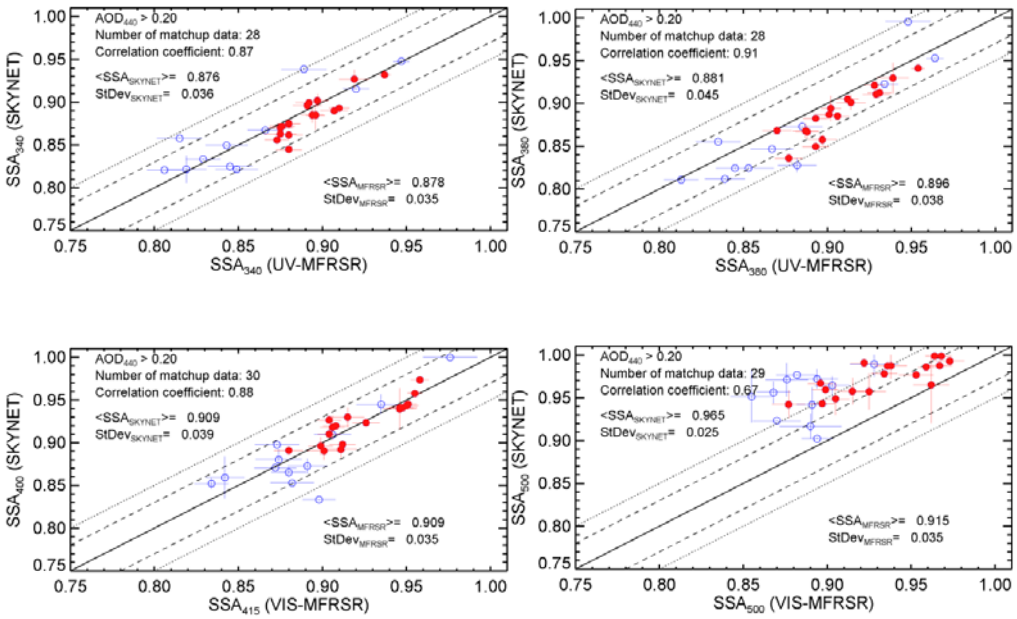

Figure 5.7. Same as Figure 5.4 except using master calibration and surface albedo=0.04.

We now estimate the SKYNET and AMP precision from the comparison measurements following Fioletov et al. [2006] approach. Assuming that the SSA variability and the retrieval SSA errors are independent, the variance of the measured SSA by each instrument can be described by equation (5.1). Next, the measured variance of the SSA difference between SKYNET and AMP can be described by equation (5.2) assuming it is independent from the true measured SSA. The equations (5.1) – (5.2) can be inverted to estimate standard uncertainties (standard deviations) for SKYNET and AMP SSA retrievals as well as the SSA variability from the measurements themselves using equations (5.3) to (5.5):

$$\sigma^2(M_i) = \sigma^2(X) + \sigma^2(e_i), i = 1,2 \quad (5.1)$$

$$\sigma^2(M_1 - M_2) = \sigma^2(e_1) + \sigma^2(e_2) \quad (5.2)$$

$$\sigma^2(X) = (\sigma^2(M_1) + \sigma^2(M_2) - \sigma^2(M_1 - M_2))/2 \quad (5.3)$$

$$\sigma^2(e_1) = (\sigma^2(M_1) - \sigma^2(M_2) + \sigma^2(M_1 - M_2))/2 \quad (5.4)$$

$$\sigma^2(e_2) = (\sigma^2(M_2) - \sigma^2(M_1) + \sigma^2(M_1 - M_2))/2 \quad (5.5)$$

where M_i is the measured SSA and its error (e_i). M_1 and M_2 are the SKYNET SSA and the AMP SSA measurements, respectively. e_1 and e_2 are the SKYNET SSA error and the AMP SSA error, respectively.

Table 5.3. Estimation of the standard instrumental uncertainty and the standard deviation of variability. SKYNET retrievals with surface albedo=0.1 are indicated in parentheses.

Wavelength (nm)	Standard uncertainty in SKYNET [$\sigma(e_1)$]	Standard uncertainty in AMP [$\sigma(e_2)$]	Standard deviation of the true value [$\sigma(X)$]
		SSA	
340	0.0137	0.0109	0.0332
	(0.0131)	(0.0045)	(0.0329)
380	0.0224	0.0117	0.0395
	(0.0146)	(0.0060)	(0.0345)
415	0.0181	0.0024	0.0346
	(0.0204)	(0.0124)	(0.0327)
500	0.0056	0.0250	0.0240
	(0.0094)	(0.0180)	(0.0289)

Table 5.4 shows SSA comparison statistics, including RMSD, the mean bias, MBD (e.g., ~0.002 at 340 nm) and standard deviation of the differences, STD ~ 0.018 at wavelengths of 340 – 415 nm, which is comparable to the estimated uncertainties in both SSA retrievals.

Table 5.4. Correlation and statistical differences between AMP and SKYNET retrieved SSA and AOD with surface albedo=0.04. RMSD is root mean square deviation, MBD is mean bias deviation, STD is standard deviation of differences, and U95 is percentile 95. SKYNET retrievals with surface albedo=0.1 are indicated in parentheses.

Wavelength (nm)	Correlation	RMSD	MBD (AMP–SKYNET)	STD	U95	Number
			SSA			
340	0.873 (0.916)	0.018 (0.027)	0.002 (0.023)	0.018 (0.014)	0.027 (0.047)	28 (26)
380	0.910 (0.935)	0.024 (0.035)	0.015 (0.033)	0.019 (0.013)	0.043 (0.056)	28 (26)
415*	0.882 (0.916)	0.018 (0.028)	0.000 (0.023)	0.018 (0.016)	0.029 (0.054)	30 (28)
500	0.674 (0.807)	0.056 (0.035)	-0.050 (-0.028)	0.026 (0.020)	-0.008 (0.007)	29 (28)
			AOD			
340	0.993 (0.993)	0.051 (0.054)	0.036 (0.038)	0.037 (0.038)	0.088 (0.088)	28 (26)
380	0.993 (0.993)	0.034 (0.035)	-0.010 (-0.009)	0.033 (0.034)	0.036 (0.037)	28 (26)
415	0.993 (0.992)	0.036 (0.038)	0.018 (0.019)	0.032 (0.033)	0.071 (0.071)	30 (28)
500	0.990 (0.990)	0.038 (0.039)	0.020 (0.022)	0.032 (0.033)	0.075 (0.075)	29 (28)

*Comparison of AMP SSA in 415 nm with SKYNET SSA in 400 nm.

5.6.3. Atmospheric gas absorption

This study accounts for effects of gaseous (ozone and NO_2) absorption in the UV and visible wavelengths. Unlike the MFRSR inversion, neither SKYNET

nor Version 2 AERONET inversion accounts for NO_2 absorption. In the upcoming AERONET Version 3 data base, the NO_2 absorption will be accounted for, but with using monthly NO_2 climatological values from Aura/OMI satellite. Ozone absorption is small at the visible wavelengths shorter than ~500 nm but should be considered at UV wavelengths shorter than 330 nm. Krotkov et al. [2005c] reported that unaccounted NO_2 absorption contributes to the low bias in SSA and could lead to incorrect interpretation of aerosol composition. Such errors in daily SSA retrievals will be introduced if one uses a fixed climatological value of column NO_2 [Corr et al., 2009].

5.7. Effect of surface albedo on the SSA retrievals

MFRSR spectral SSAs at 325, 332, and 340 nm are very similar due to small separation in wavelength. Previous studies [Che et al., 2008; Hashimoto et al., 2012; Khatri et al., 2016] show that the SKYNET SSA is overestimated compared to the AERONET SSA. Khatri et al. [2016] reported that the main factors affecting discrepancies of SSA between AERONET and SKYNET retrievals were different AOD values and systematic differences in absolute calibration of sky radiances. Specifically, overestimation of sky radiances in SKYNET measurements results in SSA overestimation as compared to AERONET.

In agreement with the previous studies [Che et al., 2008; Hashimoto et al., 2012; Khatri et al., 2016], my comparison confirms overestimation of SKYNET

SSA in the visible wavelengths compared to AERONET inversions. My new finding is SKYNET SSA underestimation in the UV, which has not been previously discussed. The underestimation could be explained, in part, by unrealistically high surface albedo (0.1) used in SKYNET inversions. The UV surface albedo should not be larger than the MODIS derived values at 470 nm (~0.04), used in AERONET SSA retrievals at 440 nm. Following this recommendation, updating the surface albedo in SKYNET inversion to the average AERONET value ~0.04, significantly increases SSA in UV (Figure 5.8). This single most important correction essentially removes the bias in UV, but increases the bias at 500 nm. This could be explained by smaller AOD at 500 nm (Figure 5.9). Also, possibly additional surface reflectance bias at 500 nm causes elevated bias at 500 nm since the surface reflectance should be greater than 0.04 due to vegetation reflectance.

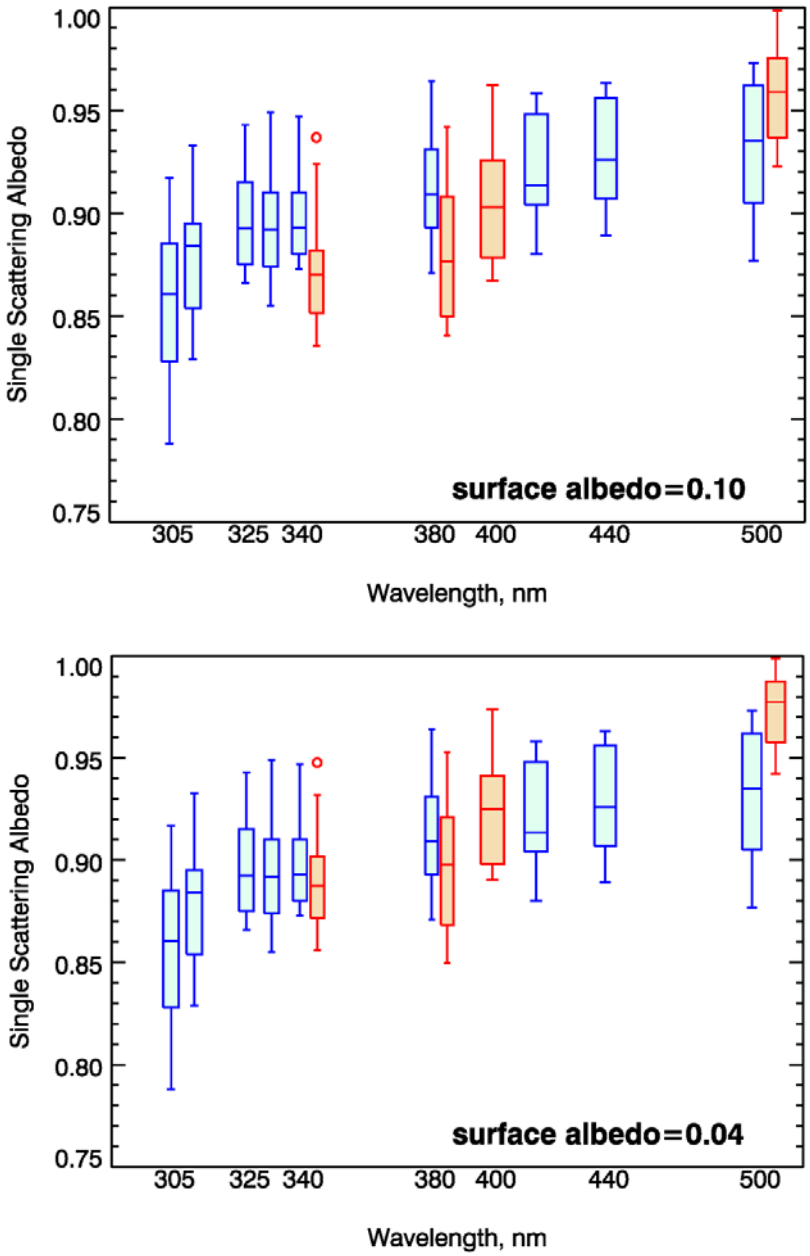

Figure 5.8. Combined spectral SSA from AMP-retrievals (blue boxes) and SKYNET retrievals (orange boxes) using surface albedo=0.1 (top) and 0.04 (bottom). The bottom and top edges of the boxes are located at the sample 25th and 75th percentiles; the whiskers extend to the minimal and maximal values within 1.5 IQR. The center horizontal lines are drawn at the median values.

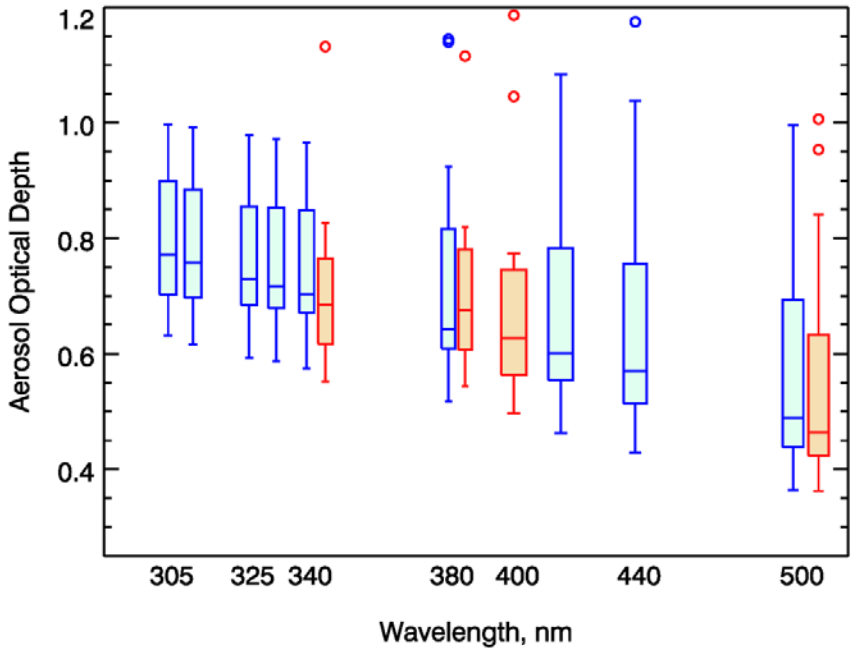

Figure 5.9. Spectral AOD from AMP-retrievals (blue) and SKYNET retrievals (orange). The bottom and top edges of the boxes are located at the 25th and 75th percentiles; the whiskers extend to the minimal and maximal values within 1.5 IQR. The circles show outliers outside of 1.5 IQR. The center horizontal lines are drawn at the median values.

5.8. Summary and discussion

In this chapter, SSA comparisons with SKYNET retrievals were performed using concurrent measurements from a combination of AERONET, MFRSR, and Pandora measurements. This combination of instrumentation is required to ensure accurate AOD measurements (i.e., within 0.01) and to correct for gaseous interferences due to ozone and NO_2. I focused on the application of the instrumentation and techniques to measure the column spectral SSA in the

near UV and visible wavelengths. This study demonstrates spectral surface irradiance consistency with the sky radiance measurements and quantifies enhanced column UV aerosol absorption. As far as I know, this study is the first validation of the SKYNET-retrieved SSA at UV wavelengths (340 and 380 nm). It is found that SKYNET provide reliable SSA at UV wavelengths (340 and 380 nm) on condition that NO_2 absorption and surface albedo are accounted for. These measurements are essential to answer how the spectral dependence of light absorbing aerosols in UV affects the air quality, surface UV radiation, and tropospheric oxidation capacity, which remains highly uncertain. In addition, retrieved spectral dependence in UV contributes to improve the classification algorithm of the columnar aerosol types [Choi et al., 2016] and satellite SSA retrievals from the current (Aura OMI [Jethva and Torres, 2011] and SNPP OMPS) and future satellite atmospheric composition missions (TROPOMI, TEMPO, and GEMS).

Chapter 6: Summary, Conclusions, and Future work

6.1. Summary and Conclusions

This study uses simultaneous measurements from co-located AERONET and MFRSR instruments to ensure (1) accurate measurements of aerosol extinction optical depth (AOD) and (2) consistent inversions of aerosol column absorption properties (i.e., single scattering albedo (SSA) and imaginary part of the effective complex refractive index) between UV and visible wavelengths.

To reduce the instrument errors, MFRSR instruments were characterized for their spectral and cosine response at NOAA Central UV Calibration Facility. Using these well-calibrated responses, I performed further correction processes, such as night-time voltage correction, angular response correction, tilt correction, corrections for atmospheric pressure and gaseous absorption (ozone and NO_2), determining extraterrestrial calibration factor (V_0), and cloud screening in AERONET calibration site at NASA/GSFC. Monitoring V_0 is necessary for the long-term assessment of the MFRSR calibration stability.

This dissertation describes long-term ground-based measurements of spectral column aerosol absorption at NASA/GSFC by combining almucantar (AERONET) and shadowband techniques (MFRSR) in UV and visible wavelengths with the spectral overlap at 440 nm. The comparison between MFRSR and AERONET aerosol absorption retrievals shows good agreement at common wavelength 440 nm. Relaxing AERONET Level 2 filters are suggested

to accept retrievals with AOD_{440} > 0.2 and SZA > 30º. With relaxed filters, the number of MFRSR–AERONET matchup increases by a factor of about 4 to 461 good matchup retrievals, the minimum–maximum SSA range doubles from 0.07 (0.93 to 1) to 0.15 (0.85 to 1), and the average SSA decreases by ~0.01 to 0.956 (MFRSR) or 0.952 for AERONET. The latter value is within 0.02 uncertainty range for AERONET climatological value of 0.96 [Giles et al., 2012].

The light absorbing (chromophoric) organic or "brown" carbon (BrC) is studied during the biomass-burning season in the Amazon basin using surface and space-based remote sensing. A new method is developed to infer the effective imaginary refractive index (*k*) of aerosol using the ground-based measurements from AERONET in the visible wavelengths and UV-MFRSR in the UV and ozone and NO_2 from the Ozone Monitoring Instrument (OMI) on NASA EOS Aura satellite. This represents the first effort to separate effects of gaseous (ozone and NO_2) and aerosol absorption and partition black and brown (light-absorbing organic) carbon absorption in the short UV-B wavelengths.

Using this new method, my study found that BrC has negligible relatively weak absorption in visible wavelengths, but significant absorption with the strong spectral dependence in UV. The estimated range of the column volume fraction of BrC is 0.05 to 0.27 and of its column mass density is ~11 to 61 mg/m^2. The best estimate is likely close to the upper bound because the lower bound represents more absorbing BrC from high temperature burn conditions in southern Africa savanna. The largest mass absorption efficiencies of BrC are observed at 305 nm, but vary significantly (e.g., 2.9 to 16.1 m^2/g) due to variability in BrC column

effective imaginary refractive index (k_{BrC}). This study was capable to constrain its spectral dependence with improved accuracy despite this uncertainty in absolute values of k_{BrC}. The best fit to the spectral dependence of k_{BrC} in UV wavelengths is the power-law with retrieved exponent of 5.4 to 5.7.

This work quantified the BrC effect on reducing biologically harmful ultraviolet B (UV-B: 305 – 320 nm) radiation reaching the surface. Reduced UV-B means less erythema (sunburn) cases, plant damage, but also a slower photochemistry. A photochemical box model is used to show that relative to black carbon (BC) alone, the combined optical properties of BrC and BC slow the net rate of production of ozone by up to 18% and lead to reduced concentrations of radicals OH, HO_2, and RO_2 by up to 17%, 15%, and 14%, respectively. The optical properties of BrC aerosol change in subtle ways the generally adverse effects of smoke from biomass burning.

The comparison of the SKYNET-retrieved SSA in UV and visible wavelengths with the SSA derived from a combination of AERONET, MFRSR, and Pandora (AMP) retrievals is performed in Seoul, South Korea in spring and summer 2016, which includes the period of the KORUS-AQ campaign. Previous studies have used the SKYNET SSA in the visible to NIR but never been compared at UV. The advantage of using combined AMP inversion for the comparison against the independent SKYNET inversion is that it separates aerosol and gaseous (NO_2 and O_3) absorption and retrieves k, AAOD, and SSA from the shortest UV-B (305 nm) through visible to NIR wavelengths (1020 nm). This study is the first comparison of the SKYNET-retrieved SSA at UV

wavelengths (340 and 380 nm). The comparison shows that SKYNET provides reliable SSA at UV wavelengths when surface albedo and NO_2 absorption are considered. These measurements contribute to better understanding to answer how the spectral dependence of light absorbing aerosols in UV influences the air quality, surface UV radiation, and tropospheric oxidation capacity, which remains highly uncertain.

6.2. Suggestions for Future work

Non-spherical dust aerosols will be considered in the future. In this study, the column effective aerosol absorption parameters are retrieved in UV and VIS wavelengths assuming all aerosol particles are spherical. The dominant aerosols in GSFC and Santa Cruz are spherical according to the effective sphericity from the AERONET inversions. However, Seoul in South Korea (Chapter 5) has been frequently affected by non-spherical soil dust, one of UV-absorbing aerosols.

The UV-MFRSR retrievals in Chapter 3 will be capable for comparison with the DISCOVER-AQ data in Baltimore and Washington in order to investigate how well aerosol optical properties from ground-based MFRSR measurement correlate with those from aircraft measurements. The column water soluble organic carbon (WSOC) was measured by the aircraft (NASA P-3B) during DISCOVER-AQ in Baltimore and Washington. Aircraft measurements in conjunction with BrC retrievals are used to estimate the ratio of BrC/WSOC.

In Chapter 3 and 5 of the dissertation, how retrievals of aerosol absorption

are affected by the column amount of ozone and NO_2 is demonstrated. On the contrary, aerosol absorption has an effect on the retrievals of trace gases (ozone, NO_2, and SO_2). Future research might improve the algorithm of gas absorption measurements such as Pandora spectrometer by separating gas and aerosol absorption by partitioning aerosol and gaseous absorption.

In Chapter 4, how smoke can change the ozone photochemistry is presented. Interestingly, the impact of BrC is different at near the fires and downwind of the fires. Downwind of the fires, radicals (RO_x) are produced more slowly by BrC and lower concentration of RO_x mean that ozone and its precursors (NO_x and VOCs) have longer lifetimes. This might cause greater ozone concentrations downwind. The net impact will be controlled by the rate of dispersion and non-linear photochemistry including the speciation of VOCs. Future studies should take account of sufficient ambient measurements to initialize and constrain a 3-D chemical transport model.

The new BrC retrieval strategy suggested in Chapter 4 is very beneficial to study aerosol absorption in UV because this methodology can be implemented in commonly used commercial UV shadowband instrument such as the UV-MFRSR. Unlike laboratory measurements that are hard to obtain and difficult to relate to in-situ aerosol in the atmosphere, the UV-MFRSR method is relatively low cost and robust. This methodology can be used at the currently operated UV-MFRSR network (e.g., UVMRP) to scrutinize the absorption of BrC at UV wavelengths.

Bibliography

Ahn, C., Torres, O. & Jethva, H. Assessment of OMI near-UV aerosol optical depth over land. *J. Geophys. Res.* **119,** 2457–2473 (2014).

Albuquerque, L. M. M. *et al.* Sensitivity studies on the photolysis rates calculation in Amazonian atmospheric chemistry – Part I: The impact of the direct radiative effect of biomass burning aerosol particles. *Atmos. Chem. Phys. Discuss.* **5,** 9325–9353 (2005).

Alexandrov, M. D. *et al.* Optical depth measurements by shadow-band radiometers and their uncertainties. *Appl. Opt.* **46**, 8027–8038 (2007).

Allen, J. in "Fires and Smoke Across South America" published in NASA Earth Observatory website on 07/11/2007 (Available online at: http://earthobservatory.nasa.gov/IOTD/view.php?id=8033&eocn=image&eoci=related_image Retrieved 07/12/2016).

Arola, A. *et al.* Assessment of TOMS UV bias due to absorbing aerosols. *J. Geophys. Res.* **110,** D23211 (2005).

Arola, A. *et al.* A new approach to correct for absorbing aerosols in OMI UV. *Geophys. Res. Lett.* **36,** L22805 (2009).

Arola, A. *et al.* Inferring absorbing organic carbon content from AERONET data. *Atmos. Chem. Phys.* **11,** 215–225 (2011).

Atkinson, R. et al. Evaluated kinetic and photochemical data for atmospheric chemistry: Volume IV – gas phase reactions of organic halogen species. *Atmos. Chem. Phys.* **8,** 4141– 4496 (2008).

Bais, A. F. *et al*. Deriving an effective aerosol single scattering albedo from spectral surface UV irradiance measurements. *Atmos. Environ.* **39(6),** 1093–1102 (2005).

Barnard, J. C., Volkamer, R. & Kassianov, E. I. Estimation of the mass absorption cross section of the organic carbon component of aerosols in the Mexico City Metropolitan Area. *Atmos. Chem. Phys.* **8,** 6665–6679 (2008).

Bigelow, D. S., Slusser, J. R., Beaubien, A. F. & Gibson, J. H. The USDA ultraviolet radiation monitoring program, *Bull. Amer. Meteor. Soc.* **79(4)**, 601–615 (1998).

Bond, T. C. Spectral dependence of visible light absorption by carbonaceous particles emitted from coal combustion. *Geophys. Res. Lett,* **28(21),** 4075–4078 (2001).

Bond, T. C. & Bergstrom, R. W. Light Absorption by Carbonaceous Particles: An Investigative Review. *Aerosol Sci. Technol.* **40,** 27–67 (2006).

Bond, T. C. *et al*. Bounding the role of black carbon in the climate system: A scientific assessment. *J. Geophys. Res.* **118(11),** 5380–5552 (2013).

Buchard, V., Brogniez, C., Auriol, F. & Bonnel, B. Aerosol single scattering albedo retrieved from ground-based measurements in the UV and visible region. *Atmos. Meas. Tech.* **4,** 1–7 (2011).

Campanelli, M., Nakajima, T., & Olivieri, B. Determination of the solar calibration constant for a sun-sky radiometer: proposal of an in-situ procedure. *Appl. Opt.* **43,** 651–659 (2004).

Castro, T., Madronich, S., Rivale, S., Muhlia, A. & Mar, B. The influence of

aerosols on photochemical smog in Mexico City. *Atmos. Environ.* **35,** 1765–1772 (2001).

Chakrabarty, R. K. et al. Brown carbon in tar balls from smoldering biomass combustion. *Atmos. Chem. Phys.* **10,** 6363–6370 (2010).

Chakrabarty, R. K. *et al.* Brown carbon aerosols from burning of boreal peatlands: microphysical properties, emission factors, and implications for direct radiative forcing. *Atmos. Chem. Phys.* **16,** 3033–3040 (2016).

Che, H. *et al.* Intercomparison between aerosol optical properties by a PREDE skyradiometer and CIMEL sunphotometer over Beijing, China. *Atmos. Chem. Phys.* **8,** 3199–3214, (2008).

Chen, Y. & Bond, T. C. Light absorption by organic carbon from wood combustion. *Atmos. Chem. Phys.* **10,** 1773–1787 (2010).

Chen, M., Davis, J., Tang, H., Ownby, C., & Gao, W. The calibration methods for Multi-Filter Rotating Shadowband Radiometer: a review. *Frontiers of Earth Science* **7(3),** 257–270 (2013).

Choi, Y., Ghim, Y. S., & Holben, B. N. Identification of columnar aerosol types under high aerosol optical depth conditions for a single AERONET site in Korea. *J. Geophys. Res.* **121,** 1264–1277 (2016).

Ciren, P. B., & Li, Z. Long-term global earth surface ultraviolet radiation exposure derived from ISCCP and TOMS satellite measurements. *Agricultural and Forest Meteorology,* **120,** 51–68 (2003).

Clough, S. A. *et al.* Atmospheric radiative transfer modeling: a summary of the AER codes. *J. Quant. Spectrosc. Radiat. Transfer,* **91,** 233–244 (2005).

Clough, S. A., Iacono, M. J., & Moncet, J. L. Line-by-line calculations of atmospheric fluxes and cooling rates: Application to water vapor. *J. Geophys. Res.* **97,** 15761–15785 (1992)

Corr, C. A. *et al.* Retrieval of aerosol single scattering albedo at ultraviolet wavelengths at the T1 site during MILAGRO. *Atmos. Chem. Phys.* **9,** 5813–5827 (2009).

Dickerson, R. R., Measurements of reactive nitrogen compounds in the free troposphere. *Atmos. Environ.* **18,** 2585−2593 (1984).

Dickerson, R. R. *et al.* The impact of aerosols on solar ultraviolet radiation and photochemical smog. *Science* **278,** 827–830 (1997).

Douglass, A. R. et al. Choosing meteorological input for the global modeling initiative assessment of high-speed aircraft. *J. Geophys. Res.* **104,** 27545–27564 (1999).

Dubovik, O. *et al.* Accuracy assessments of aerosol optical properties retrieved from Aerosol Robotic Network (AERONET) Sun and sky radiance measurements, *J. Geophys. Res.,* **105,** 9791–9806 (2000).

Dubovik, O. & King, M. D. A flexible inversion algorithm for retrieval of aerosol optical properties from Sun and sky radiance measurements, *J. Geophys. Res.* **105,** 20673–20696 (2000).

Dubovik, O. *et al.* Variability of absorption and optical properties of key aerosol types observed in worldwide locations. *J. Atmos. Sci.* **59,** 590–608 (2002a).

Dubovik, O. *et al.* Non-spherical aerosol retrieval method employing light scattering by spheroids. *Geophys. Res. Lett,* **29(10),** 1415 (2002b).

Eck, T. F., Holben, B. N., Slutsker, I. & Setzer, A. Measurements of irradiance attenuation and estimation of aerosol single scattering albedo for biomass burning aerosols in Amazonia. *J. Geophys. Res.* 103, 31865–31878 (1998).

Eck, T. F. *et al.* Wavelength dependence of the optical depth of biomass burning, urban, and desert dust aerosols. *J. Geophys. Res.* **104,** 31333–31349 (1999).

Eck, T. F. *et al.* Optical properties of boreal region biomass burning aerosols in central Alaska and seasonal variation of aerosol optical depth at an Arctic coastal site, *J. Geophys. Res.* **114,** D11201 (2009).

Estelles, V., Campanelli, M., Utrillas, M. P., Exposito, F. & Martinez-Lozano, J. A. Comparison of AERONET and SKYRAD4.2 inversion products retrieved from a Cimel CE318 sunphotometer, *Atmos. Meas. Tech.* **5,** 569–579 (2012).

Favez, O., Alfaro, S. C., Sciare, J., Cachier, H. & Abdelwahab, M. M. Ambient measurements of light-absorption by agricultural waste burning organic aerosols. *J. Aerosol Sci.* **40,** 613–620 (2009).

Feng, Y., Ramanathan, V. & Kotamarthi, V. R. Brown carbon: a significant atmospheric absorber of solar radiation? *Atmos. Chem. Phys.* **13,** 8607–8621 (2013).

Fioletov, V. E., Tarasick, D. W. & Petropavlovskikh, I. Estimating ozone variability and instrument uncertainties from SBUV(/2), ozonesonde, Umkehr, and SAGE II measurements: Short-term variations. *J. Geophys. Res.* **111,** D02305 (2006).

Fioletov, V. E. *et al.* Sulfur dioxide (SO_2) vertical column density measurements by Pandora spectrometer over the Canadian oil sands. *Atmos. Meas. Tech.* **9,**

2961–2976 (2016).

Goliff, W. S., Stockwell, W. R. & Lawson, C. V. The regional atmospheric chemistry mechanism, version 2. *Atmos. Environ.* **68,** 174–185 (2013).

Giles, D. M. *et al.* An analysis of AERONET aerosol absorption properties and classifications representative of aerosol source regions. *J. Geophys. Res.* **117,** D17293 (2012).

Hansen, J., Sato, M. & Ruedy, R. Radiative forcing and climate response. *J. Geophys. Res. Atmos.* **102,** 6831–6864 (1997).

Hammer, M. S. *et al.* Interpreting the ultraviolet aerosol index observed with the OMI satellite instrument to understand absorption by organic aerosols: implications for atmospheric oxidation and direct radiative effects. *Atmos. Chem. Phys.* **16,** 2507–2533 (2016).

Harrison, L., & Michalsky, J. Objective algorithms for the retrieval of optical depths from ground-based measurements. *Appl. Opt.* **33,** 5126–5132 (1994).

Harrison, L., Michalsky, J. & Berndt, J. Automated multifilter rotating shadow-band radiometer: an instrument for optical depth and radiation measurements. *Appl. Opt.* **33,** 5118–5125 (1994).

Harrison, L. *et al.* The rotating shadowband spectroradiometer (RSS) at SGP. *Geophys. Res. Lett,* **26,** 1715–1718 (1999).

Hashimoto, M. *et al.* Development of a new data-processing method for SKYNET sky radiometer observations. *Atmos. Meas. Tech.* **5,** 2723–2737 (2012).

He, S. & Carmichael, G. R. Sensitivity of photolysis rates and ozone production in the troposphere to aerosol properties. *J. Geophys. Res.* **104,** 26307–26324

(1999).

Herman, B. M., Browning, R. S. & De Luisi, J. J. Determination of effective imaginary term of the complex refractive index of atmospheric dust by remote sensing: the diffuse-direct Radiation method. *J. Atmos. Sci.* **32,** 918–925 (1975).

Herman, J. *et al.* NO_2 column amounts from ground-based Pandora and MFDOAS spectrometers using the direct-sun DOAS technique: Intercomparisons and application to OMI validation. *J. Geophys. Res.* **114,** D13307 (2009).

Hodzic, A. *et al.* Wildfire particulate matter in Europe during summer 2003: meso-scale modeling of smoke emissions, transport and radiative effects. *Atmos. Chem. Phys.* **7,** 4043–4064 (2007).

Hoffer, A. *et al.* Optical properties of humic-like substances (HULIS) in biomass-burning aerosols. *Atmos. Chem. Phys.* **6,** 3563–3570 (2006).

Holben, B. N. *et al.* AERONET—A Federated Instrument Network and Data Archive for Aerosol Characterization. *Remote Sens. Environ.* **66,** 1–16 (1998).

Holben, B. N. *et al.* An emerging ground-based aerosol climatology: Aerosol optical depth from AERONET, *J. Geophys. Res.* **106,** 12067–12097 (2001).

Ialongo, I., Buchard, V., Brogniez, C., Casale, G. R., & Siani, A. M. Aerosol Single Scattering Albedo retrieval in the UV range: an application to OMI satellite validation. *Atmos. Chem. Phys.* **10,** 331–340 (2010).

IPCC, 2007: Climate Change 2007: The Physical Science Basis. Contribution of Working Group I to the Fourth Assessment Report of the Intergovernmental

Panel on Climate Change [Solomon, S., D. Qin, M. Manning, Z. Chen, M. Marquis, K.B. Averyt, M.Tignor and H.L. Miller (eds.)]. Cambridge University Press, Cambridge, United Kingdom and New York, NY, USA.

Jacobson, M. Z. Studying the effects of aerosols on vertical photolysis rate coefficient and temperature profiles over an urban airshed, *J. Geophys. Res.* **103,** 10593 (1998).

Jacobson, M. Z. "Atmospheric Pollution" Cambridge University Press, Cambridge (2002).

Jethva, H. & Torres, O. Satellite-based evidence of wavelength-dependent aerosol absorption in biomass burning smoke inferred from Ozone Monitoring Instrument. *Atmos. Chem. Phys.* **11,** 10541–10551 (2011).

Jethva, H., Torres, O. & Ahn, C. Global assessment of OMI aerosol single-scattering albedo using ground-based AERONET inversion. *J. Geophys. Res. Atmos.* **119,** 9020–9040 (2014).

Johnson, B. T., Shine, K. P. & Forster, P. M. The semi-direct aerosol effect: Impact of absorbing aerosols on marine stratocumulus. *Quarterly Journal of the Royal Meteorological Society* **130,** 1407–1422 (2006).

Johnston, F. H. *et al.* Estimated Global Mortality Attributable to Smoke from Landscape Fires. *Environ. Health Perspect.* **120,** 695–701 (2012).

Kassianov, E. I., Barnard, J. C. & Ackerman, T. P. Retrieval of aerosol microphysical properties using surface MultiFilter Rotating Shadowband Radiometer (MFRSR) data: Modeling and observations. *J. Geophys. Res.* **110,** D09201 (2005).

Kazadzis, S. *et al.* Aerosol absorption retrieval at ultraviolet wavelengths in a complex environment. *Atmos. Meas. Tech. Discuss.* doi:10.5194/amt-2016-273, in review (2016).

Kerr, J. B. *et al.* "Surface ultraviolet radiation: Past and future." *Scientific assessment of ozone depletion* (2002): 5-1.

Khatri, P. *et al.* Factors for inconsistent aerosol single scattering albedo between SKYNET and AERONET. *J. Geophys. Res.* **121,** 1859–1877 (2016).

King, M. D. & Herman, B. M. Determination of the ground albedo and the index of absorption of atmospheric particulates by remote sensing. Part 1: theory. *J. Atmos. Sci.* **36,** 163–173 (1979).

Kirchstetter, T. W., Novakov, T. & Hobbs, P. V. Evidence that the spectral dependence of light absorption by aerosols is affected by organic carbon. *J. Geophys. Res.* **109,** D21208 (2004).

Koren, I., Kaufman, Y. J., Remer, L. A., & Martins, J. V. Measurement of the Effect of Amazon Smoke on Inhibition of Cloud Formation. *Science* **303,** 1342–1345 (2004).

Krotkov, N. A., Bhartia, P. K., Herman, J. R., Fioletov, V. & Kerr, J. Satellite estimation of spectral surface UV irradiance in the presence of tropospheric aerosols: 1. Cloud-free case. *J. Geophys. Res.* **103,** 8779–8793 (1998).

Krotkov, N. A. *et al.* Aerosol ultraviolet absorption experiment (2002 to 2004), part 1: ultraviolet multifilter rotating shadowband radiometer calibration and intercomparison with CIMEL sunphotometers. *Opt. Eng.* **44,** 041004 (2005a).

Krotkov, N. A. *et al.* Aerosol ultraviolet absorption experiment (2002 to 2004),

part 2: absorption optical thickness, refractive index, and single scattering albedo. *Opt. Eng.* **44,** 041005 (2005b).

Krotkov, N. A., Herman, J. R., Cede, A., & Labow, G. Partitioning between aerosol and NO_2 absorption in the UV spectral region. *Proc. SPIE* **5886,** Ultraviolet Ground- and Space-based Measurements, Models, and Effects V, 588601 (2005c).

Krotkov, N. A. *et al.* Aerosol column absorption measurements using co-located UV-MFRSR and AERONET CIMEL instruments. *Proc. SPIE* **7462,** Ultraviolet and Visible Ground- and Space-based Measurements, Trace Gases, Aerosols and Effects VI, 746205 (2009).

Lack, D. A. *et al.* Brown carbon and internal mixing in biomass burning particles. *Proc. Natl. Acad. Sci. U.S.A.* **109,** 14802–14807 (2012).

Lack, D. A. & Langridge, J. M. On the attribution of black and brown carbon light absorption using the Ångström exponent. *Atmos. Chem. Phys.* **13,** 10535–10543 (2013).

Laskin, A., Laskin, J. & Nizkorodov, S. A. Chemistry of Atmospheric Brown Carbon. *Chem. Rev.* **115,** 4335−4382 (2015).

Lautenschlager, S., Wulf, H. C. & Pittelkow, M. R. Photoprotection. *Lancet* **370,** 528–537 (2007).

Leszczynski, K., Jokela, K., Ylianttila, L., Visuri, R., & Blumthaler, M. Erythemally weighted radiometers in solar UV monitoring: Results from the WMO/STUK intercomparison. *Photochem. Photobiol.* **67,** 212–221 (1998).

Levelt, P. F. et al. The Ozone Monitoring Instrument. *IEEE Trans. Geosci. Remote*

Sens. **44,** 1093–1101 (2006).

Li, Z., Wang, P., & Cihlar, J. A simple and efficient method for retrieving surface UV radiation dose rate from satellite. *J. Geophys. Res.* **105(D4),** 5027–5036 (2000).

Liu, J. *et al.* Size-resolved measurements of brown carbon in water and methanol extracts and estimates of their contribution to ambient fine-particle light absorption. *Atmos. Chem. Phys.* **13,** 12389–12404 (2013).

Lu, Z. *et al.* Light Absorption Properties and Radiative Effects of Primary Organic Aerosol Emissions. *Environ. Sci. Technol.* **49,** 4868–4877 (2015).

Madronich, S. UV radiation in the natural and perturbed atmosphere. *Environmental Effects of Ultraviolet (UV) Radiation*, pp.17-69, Lewis Publisher, Boca Raton, FL (1993).

Mancebo, S. E. & Wang, S. Q. Skin cancer: role of ultraviolet radiation in carcinogenesis. *Rev. Environ. Health* **29,** 265–273 (2014).

Martins, J. V., Artaxo, P., Kaufman, Y. J., Castanho, A. D. & Remer, L. A. Spectral absorption properties of aerosol particles from 350-2500nm. *Geophys. Res. Lett.* **36,** L13810 (2009).

Michalsky, J. J. et al. Multiyear measurements of aerosol optical depth in the Atmospheric Radiation Measurement and Quantitative Links programs. *J. Geophys. Res.* **106(D11),** 12099–12107 (2001).

Mishchenko, M. I., Travis, L. D. & Lacis, A. A. Scattering, Absorption, and Emission of Light by Small Particles, Cambridge University Press, Cambridge (2002).

Mok, J. et al. Impacts of brown carbon from biomass burning on surface UV and ozone photochemistry in the Amazon Basin. *Sci. Rep.* **6,** 36940 (2016).

Moody, E. G., King, M. D., Schaaf, C. B., & Platnick, S. MODIS-Derived Spatially Complete Surface Albedo Products: Spatial and Temporal Pixel Distribution and Zonal Averages. *J. Appl. Meteorol.* **47,** 2879–2894 (2008).

Moosmuller, H., Chakrabaty, R. K., Ehlers, K. M. & Arnott, W. P. Absorption Angstrom Coefficient, Brown Carbon, and Aerosols: Basic Concepts, Bulk Matter, and Spherical Particles. *Atmos. Chem. Phys.* **11,** 1217–1225 (2011).

Myhre, G. *et al.* Radiative forcing of the direct aerosol effect from AeroCom Phase II simulations. *Atmos. Chem. Phys.* **13,** 1853–1877 (2013).

Nakajima, T., Tanaka, M., & Yamauchi, T. Retrieval of the Optical-Properties of Aerosols From Aureole and Extinction Data. *Appl. Opt.* **22,** 2951–2959 (1983).

Nakajima, T. *et al.* Use of sky brightness measurements from ground for remote sensing of particulate polydispersions. *Appl. Opt.* **35,** 2672–2686 (1996).

Nakajima, T. *et al.* Overview of the Atmospheric Brown Cloud East Asian Regional Experiment 2005 and a study of the aerosol direct radiative forcing in east Asia. *J. Geophys. Res.* **112,** D24S91 (2007).

Petters, J. L., Saxena, V. K., Slusser, J. R., Wenny, B. N. & Madronich, S. Aerosol single scattering albedo retrieved from measurements of surface UV irradiance and a radiative transfer model, *J. Geophys. Res.* **108**, 4288, (2003).

Pickering, K. E. *et al.* Photochemical ozone production in tropical squall line convection during NASA Global Tropospheric Experiment/Amazon

Boundary Layer Experiment 2A. *J. Geophy. Res.* **96,** 3099–3114 (1991).

Reid, J. S. *et al.* Real-time monitoring of South American smoke particle emissions and transport using a coupled remote sensing/box-model approach. *Geophys. Res. Lett.* **31,** L06107 (2004).

Reid, J. S., Koppmann, R., Eck, T. F. & Eleuterio, D. P. A review of biomass burning emissions part II: intensive physical properties of biomass burning particles. *Atmos. Chem. Phys.* **5,** 799–825 (2005).

Rousseaux, M. C. *et al.* Ozone depletion and UVB radiation: Impact on plant DNA damage in southern South America. *Proc. Natl. Acad. Sci. U.S.A.* **96,** 15310–15315 (1999).

Sander, S.P. et al. Chemical Kinetics and Photochemical Data for Use in Atmospheric Studies. Evaluation No. 17. Jet Propulsion Laboratory, Pasadena, CA (2011).

Saleh, R. *et al.* Absorptivity of brown carbon in fresh and photo-chemically aged biomass-burning emissions. *Atmos. Chem. Phys.* **13,** 7683–7693 (2013).

Saleh, R. *et al.* Brownness of organics in aerosols from biomass burning linked to their black carbon content. *Nature Geosci.* **7,** 647–650 (2014).

Schnaiter, M. *et al.* Measurement of wavelength-resolved light absorption by aerosols utilizing a UV-VIS extinction cell. *Aerosol Sci. Technol.* **39,** 249–260 (2005).

Schuster, G. L., Dubovik, O., Holben, B. N. & Clothiaux, E. E. Inferring black carbon content and specific absorption from Aerosol Robotic Network (AERONET) aerosol retrievals. *J. Geophys. Res.* **110,** D10S17 (2005).

Schuster, G. L., Lin, B. & Dubovik, O. Remote sensing of aerosol water uptake. *Geophys. Res. Lett.* **36,** L03814 (2009).

Schuster, G. L., Dubovik, O. & Arola, A. Remote sensing of soot carbon – Part 1: Distinguishing different absorbing aerosol species. *Atmos. Chem. Phys.* **16,** 1565–1585 (2016).

Slusser, J. *et al.* Langley method of calibrating UV filter radiometers. *J. Geophys. Res.* **105(D4),** 4841–4849 (2000).

Srinivas, B., & Sarin, M. M. Brown carbon in atmospheric outflow from the Indo-Gangetic Plain: Mass absorption efficiency and temporal variability. *Atmos. Environ.* **89,** 835–843 (2014).

Srinivas, B., Rastogi, N., Sarin, M. M., Singh, A. & Singh, D. Mass absorption efficiency of light absorbing organic aerosols from source region of paddy-residue burning emissions in the Indo-Gangetic Plain. *Atmos. Environ.* **125,** 360–370 (2016).

Stamnes, K., Tsay, S., Wiscombe, W. & Jayaweera, K. Numerically stable algorithm for discrete-ordinate-method radiative transfer in multiple scattering and emitting layered media. *Appl. Opt.* **27,** 2502–2509 (1988).

Stocker, T. F. *et al.* "IPCC, 2013: climate change 2013: the physical science basis. Contribution of working group I to the fifth assessment report of the intergovernmental panel on climate change." (2013).

Stockwell, W. R., Kirchner, F., Kuhn, M., & Seefeld, S. A new mechanism for regional atmospheric chemistry modeling. *J. Geophys. Res.,* **102,** 25847–25879 (1997).

Strahan, S. E. et al. Using transport diagnostics to understand chemistry climate model ozone simulations. *J. Geophys. Res.* **116,** D17302 (2011).

Taylor, T. E., L'Ecuyer, T. S., Slusser, J. R., Stephens, G. L., & Goering, C. D. An operational retrieval algorithm for determining aerosol optical properties in the ultraviolet. *J. Geophys. Res.* **113,** D03201 (2008).

Teramura, A. H. & Sullivan, J. H. Effects of UV-B radiation on photosynthesis and growth of terrestrial plants. *Photosynth. Res.* **39,** 463–473 (1994).

Thomas, G. E. & Stamnes, K. Radiative Transfer in the Atmosphere and Ocean, Cambridge University Press (1999).

Torres, O., Bhartia, P. K., Herman, J. R., Ahmad, Z. & Gleason, J. Derivation of aerosol properties from satellite measurements of backscattered ultraviolet radiation: Theoretical basis. *J. Geophys. Res.* **103,** 17099–17110 (1998).

Torres, O. *et al.* A Long-Term Record of Aerosol Optical Depth from TOMS Observations and Comparison to AERONET Measurements. *J. Atmos. Sci.* **59,** 398–413 (2002).

Torres, O., Bhartia, P. K., Sinyuk, A., Welton, E. J. & Holben, B. Total Ozone Mapping Spectrometer measurements of aerosol absorption from space: Comparison to SAFARI 2000 ground-based observations. *J. Geophys. Res.* **110,** D10S18 (2005).

Torres, O. *et al.* Aerosols and surface UV products from Ozone Monitoring Instrument observations: An overview. *J. Geophys. Res.* **112,** D24S47 (2007).

Torres, O. *et al*. OMI and MODIS observations of the anomalous 2008–2009 Southern Hemisphere biomass burning seasons. *Atmos. Chem. Phys.* **10**,

3505–3513 (2010).

Torres, O., Ahn, C. & Chen, Z. Improvements to the OMI near-UV aerosol algorithm using A-train CALIOP and AIRS observations. *Atmos. Meas. Tech.* **6,** 3257–3270 (2013).

Turpin, B. J. & Lim, H. J. Species contributions to PM2.5 mass concentrations: Revisiting common assumptions for estimating organic mass. *Aerosol Sci. Technol.* **35,** 602–610 (2001).

Tzortziou, M., Herman, J. R., Cede, A., & Abuhassan, N. High precision, absolute total column ozone measurements from the Pandora spectrometer system: Comparisons with data from a Brewer double monochromator and Aura OMI. *J. Geophys. Res.* **117,** D16303 (2012).

Veihelmann, B., Konert, M., & van der Zande, W. J. Size distribution of mineral aerosol: using light-scattering models in laser particle sizing. *Appl. Opt.* **45,** 6022–6029 (2006).

Wang, Z. *et al.* Seasonal characteristics of aerosol optical properties at the SKYNET Hefei site (31.90ºN, 117.17ºE) from 2007 to 2013. *J. Geophys. Res. Atmos.* **119,** 6128–6139 (2014).

Wang, X. *et al*. Exploiting simultaneous observational constraints on mass and absorption to estimate the global direct radiative forcing of black carbon and brown carbon. *Atmos. Chem. Phys.* **14,** 10989–11010 (2014).

Yang, M., Howell, S. G., Zhuang, J. & Huebert, B. J. Attribution of aerosol light absorption to black carbon, brown carbon, and dust in China – interpretations of atmospheric measurements during EAST-AIRE. *Atmos. Chem. Phys.* **9,**

2035–2050 (2009).

Yan, C. *et al.* Chemical characteristics and light-absorbing property of water-soluble organic carbon in Beijing: Biomass burning contributions. *Atmos. Environ.* **121,** 4–12 (2015).

Zhong, M. & Jang, M. Dynamic light absorption of biomass-burning organic carbon photochemically aged under natural sunlight. *Atmos. Chem. Phys.* **14,** 1517–1525 (2014).